Superconducting Nanowire Single-Photon Detectors for Advanced Photon-Counting Applications

Chandra Mouli Natarajan

A thesis submitted for the degree of

Doctor of Philosophy

Heriot-Watt University

School of Engineering and Physical Sciences

May 2011

Abstract

The ability to detect infrared photons is increasingly important in many fields of scientific endeavour, including astronomy, the life sciences and quantum information science. Improvements in detector performance are urgently required. The Superconducting Nanowire Single-Photon Detector (SNSPD/SSPD) is an emerging single-photon detector technology offering broadband sensitivity, negligible dark counts and picosecond timing resolution. SNSPDs have the potential to outperform conventional semiconductor-based photon-counting technologies, provided the difficulties of low temperature operation can be overcome. This thesis describes how these important challenges have been addressed, enabling the SNSPDs to be used in new applications. A multichannel SNSPD system based on a closed-cycle refrigerator has been constructed and tested. Efficient optical coupling has been achieved via carefully aligned optical fibre. Fibre-coupled SNSPDs based on (i) NbN on MgO substrates and (ii) NbTiN on oxidised Si substrates have been studied. The latter give enhanced performance at telecom wavelengths, exploiting the reflection from the Si/SiO_2 interface. Currently, the detector system houses four NbTiN SNSPDs with average detection efficiency >20% at 1310 nm wavelength. We have employed SNSPDs in the characterisation of quantum waveguide circuits, opening the pathway to operating this promising platform for optical quantum computing for the first time at telecom wavelengths.

Acknowledgements

I would like to thank everyone who inspired and supported me with their contributions towards the realisation of this thesis, without them it would not have been a pleasant journey.

Foremost, I am extremely fortunate to have had *Dr. Robert Hadfield* as my Ph.D. supervisor. His perpetual enthusiasm, inspiration, approachability and guidance have played an important role in developing my skills towards being a better scientist and individual. Robert, I sincerely thank you for your untiring efforts in elucidating scientific intricacies and diverse soft skills throughout my studentship.

I am indebted to my colleagues *Dr Michael Tanner, John O'Connor* and *Catherine Fitzpatrick*. We have worked very closely on many experiments and had many insightful discussions. Thanks a lot for your constant encouragement and support throughout this thesis work. I would also like to thank *Michael Stuiber*, *Vamsi Pottapenjara* and particularly *Martin Härtig* for their meaningful contributions that are presented in this thesis.

I would like to show my gratitude to *Dr. Ryan Warburton* and *Prof. Gerald Buller* for explaining me on how to use the TCSPC card and for providing access to the timing card on many occasions.

I am grateful to *Dr. Burm Baek* and *Dr. Sae Woo Nam* (NIST, USA) for their valuable advice and key information on various issues I have encountered during the course of this thesis work. I would also like to thank *Dr. Shigehito Miki, Dr. Zhen Wang* (NICT, Japan) and *Sander Dorenbos, Esteban Bermudez* and *Dr. Val Zwiller* (TU Delft, The Netherlands) for providing us with SNSPD chips that have been used in this thesis work.

Special thanks to *Alberto Peruzzo, Damien Bonneau, Dr. Chunle Xiong, Dr. Graham Marshall, Jonathan Matthews, Dr. Mirko Lobino,* and *Prof. Jeremy O'Brien* (University of Bristol) for the numerous stimulating discussions and waveguide experiments we have conducted together.

I would like to express my humble gratitude to members of physics and electronics workshops at Heriot-Watt University, especially *Peter B. Heron, Mark Stewart* and *Andrew Haston* for their continuous support in designing and machining the parts for this thesis work.

I have to mention *Debaditya (Adi) Choudhury*, he has always been around to lend his wise thoughts and without doubt, I would have consumed far less coffee if not for his comradeship. *Adi*, special thanks to you.

Sajeev Pillai, *Arvind Sundaram* and *Praveen Subramanian* have made my life easy and comfortable in Edinburgh in umpteen ways. I owe them a lot. Thanks to you guys!

Ina Schöttling is indeed a very special friend to me. *Ina*, thank you for your care and affection.

I am extremely grateful to my sister *Vidhya* and my parents *Varalakshmi* and *Natarajan* for having fostered and encouraged me in all my endeavours.

Contents

List of Tables

List of Figures

Glossary

Roman Symbols

D	dark count rate
E	energy
E_g	band gap energy
f	frequency
h	Planck's constant
H_c	critical magnetic field
I_{bias}	bias current
I_c	critical current
I_r	return current
$I(r, z)$	intensity profile
k	extinction coefficient
$\mathcal{L}_k$	inductance per unit length
L_k	kinetic inductance
n	real component of refractive index
N_{max}	number of maximum coincidence count
N_{min}	number of minimum coincidence count
$\dot{q}_{cond}$	rate of heat transfer by conduction
$\dot{q}_{rad}$	rate of heat transfer by radiation
R	count rate
$\mathscr{R}$	reflection coefficient
R_n	hotspot resistance
R_s	series resistance
T	temperature
T_c	critical temperature

t_{gate}	time period of the gate window
$\mathscr{T}$	transmission coefficient
U_{MZ}	unitary operation of the Mach-Zehnder interferometer
V	visibility
V_{bias}	bias voltage
V_{pulse}	output pulse voltage
V_{Theory}	theoretical visibility
w_0	beam waist width at Rayleigh length
$w(z)$	beam waist width at point z
z_0	Rayleigh length

Greek Symbols

$\chi^{(2)}$	susceptibility
$\delta I(t)$	total change in current
Δt	timing jitter
$\varnothing$	diameter
ϵ	emissivity
η	efficiency
$\eta_{coupling}$	coupling efficiency
$\eta_{material}$	material efficiency
η_{qe}	quantum efficiency
$\eta_{registering}$	registering efficiency
η_{sde}	system detection efficiency
$\eta_{wavelength}$	wavelength efficiency
$\kappa(T)$	thermal conductivity
λ	wavelength
λ_{eff}	effective wavelength
$\lambda_{\mathrm{L}}^{\mathrm{NbN}}$	magnetic penetration depth of NbN
μ	mean photon flux
ν	frequency
ω_1, ω_2	angular frequencies of daughter photons
ω_D	lattice vibration frequency
ω_p	angular frequency of pump photon
π	phase shift

Ψ	work function
σ	Stefan-Boltzmann constant
τ	dead time of the detector
τ_{fall}	fall time
τ_{rise}	rise time

Acronyms

AC	Alternating Current
BCS	Bardeen, Cooper, and Schrieffer
BiBO	BIsmuth BOrate
BS	BeamSplitter
CFD	Constant Fraction Discriminator
CMOS	Complementary Metal-Oxide-Semiconductor
CNOT	Controlled-NOT
DBR	Distributed Bragg Reflector
DC	Direct Current
DCR	Dark Count Rate
DE	Detection Efficiency
EBL	Electron Beam Lithography
ETF	ElectroThermal Feedback
FEM	Finite Element Method
FET	Field-Effect Transistor
FLIM	Fluorescence Lifetime Imaging Microscopy
FWHM	Full Width at Half Maximum
GFP	Green Fluorescent Protein
GM	Gifford-McMahon
HOM	Hong-Ou-Mandel
HSQ	Hydrogen SilsesQuioxane
ISI	InterSymbol Interference
LEO	Low-Earth-Orbit
LIDAR	LIght Detection And Ranging
LNA	Low-Noise Amplifier
MCP-PMT	MicroChannel Plate Photo-Multiplier Tube
MESNSPD	Multi-Element Superconducting Nanowire Single-Photon Detector

MZ	Mach-Zehnder
NIR	Near-InfraRed
OFHC	Oxygen Free High Conductivity
PCB	Printed Circuit Board
PMF	Polarisation-Maintaining Fibre
PMMA	PolyMethyl MethAcrylate
PMT	Photo-Multiplier Tube
PNR	Photon Number Resolving
PPLN	Periodically Poled Lithium Niobate
QBER	Quantum Bit Error Rate
QE	Quantum Efficiency
QIST	Quantum Information Science and Technology
QKD	Quantum Key Distribution
RF	Radio Frequency
RIE	Reactive Ion Etching
SAM	Seperate Absorption and Multiplication
SDE	System Detection Efficiency
SEM	Scanning Electron Microscope
SMF	Single-Mode Fibre
SNR	Signal-to-Noise Ratio
SNSPD	Superconducting Nanowire Single-Photon Detector
SPAD	Single-Photon Avalanche Diode
SPDC	Spontaneous Parametric Down-Conversion
SPD	Single-Photon Detector
SQUID	Superconducting QUantum Interference Device
SSPD	Superconducting Nanowire Single-Photon Detector
STES	Superconducting Transition-Edge Sensor
STJ	Superconducting Tunnel Junction
TCSPC	Time Correlated Single-Photon Counting
ZC	Zero Crossing

List of Publications by the Candidate

Journal Articles:

1. **C. M. Natarajan**, A. Peruzzo, S. Miki, M. Sasaki, Z. Wang, B. Baek, S. Nam, R. H. Hadfield, and J. L. O'Brien, "Operating quantum waveguide circuits with superconducting single-photon detectors", *Appl. Phys. Lett.* 96, 211101 (2010).

2. M. G. Tanner, **C. M. Natarajan**, V. K. Pottapenjara, J. A. O'Connor, R. J. Warburton, R. H. Hadfield, B. Baek, S. Nam, S. N. Dorenbos, E. Bermúdez Ureña, T. Zijlstra, T. M. Klapwijk, and V. Zwiller, "Enhanced telecom wavelength single-photon detection with NbTiN superconducting nanowires on oxidized silicon", *Appl. Phys. Lett.* 96, 221109 (2010).

3. S. N. Dorenbos, H. Sasakura, M. P. van Kouwen, N. Akopian, S. Adachi, N. Namekata, M. Jo, J. Motohisa, Y. Kobayashi, K. Tomioka, T. Fukui, S. Inoue, H. Kumano, **C. M. Natarajan**, R. H. Hadfield, T. Zijlstra, T. M. Klapwijk, V. Zwiller, and I. Suemune, "Position controlled nanowires for infrared single photon emission", *Appl. Phys. Lett.* 97, 171106 (2010).

4. C. Xiong, G. D. Marshall, A. Peruzzo, M. Lobino, A. S. Clark, D.-Y. Choi, S. J. Madden, **C. M. Natarajan**, M. G. Tanner, R. H. Hadfield, S. N. Dorenbos, T. Zijlstra, V. Zwiller, M. G. Thompson, J. G. Rarity, M. J. Steel, B. Luther-Davies, B. J. Eggleton, and J. L. O'Brien, "Generation of correlated photon pairs in a chalcogenide As_2S_3 waveguide", *Appl. Phys. Lett.* 98, 051101 (2011).

5. J. A. O'Connor, M. G. Tanner, **C. M. Natarajan**, G. S. Buller, R. J. Warburton, S. Miki, Z Wang, S. W. Nam, and R. H. Hadfield, "Spatial dependence of output pulse delay in a niobium nitride nanowire superconducting single-photon detector", *Appl. Phys. Lett.*, (In Press - 2011).

Conference Papers:

1. M. B. Ward, P. M. Intallura, **C. M. Natarajan**, R. H. Hadfield, P. Atkinson, Z. L. Yuan, S. Miki, M. Fujiwara, M. Sasaki, Z. Wang, B. Baek, S. Nam, D. A. Ritchie and A. J. Shields, "Biexciton cascade in telecommunication wavelength quantum dots", *J. of Phys. Conf. Series*, 210, 012036 (2010).
2. **C. M. Natarajan**, M. M. Härtig, R. E. Warburton, G. S. Buller, R. H. Hadfield, B. Baek, S. Nam, S. Miki, M. Fujiwara, M. Sasaki, and Z. Wang, "Superconducting Nanowire Single-Photon Detectors for Quantum Communication Applications", *Quantum Communication and Quantum Networking*, QuantumComm2009, LNICST 36, pp. 225–232, Springer (2010).
3. C. R. Fitzpatrick, **C. M. Natarajan**, R. E. Warburton, G. S. Buller, B. Baek, S. Nam, S. Miki, Z. Wang, M. Sasaki, A. G. Sinclair, R. H. Hadfield, "A superconducting nanowire single-photon detector system for single-photon source characterization", *Proc. of SPIE* Vol. 7681, 76810H (2010).

Chapter 1

Introduction: Single-Photon Detectors

The ultimate frontier in photodetection is the ability to detect light at the single-photon level. Single-Photon Detectors (SPDs) [1] now play an increasing role in a wide range of fields in science and technology. Emerging application areas include deep-space communication [2], information theory [3], cryptography [4] and biotechnology [5]. SPDs are also employed in many conventional optics applications where the photon flux is very weak [6]. Conventional photodetectors cannot be operated in the single-photon regime. The energy of a single visible or infrared photon is so small that conventional detectors fail to differentiate the single-photon signal above the noise level. The energy of an individual photon (E) is the product of Planck's constant (h) and the frequency of the photon (ν). The photon energy drops with increasing wavelength, making infrared photon detection more challenging than at visible wavelengths: at 1550 nm wavelength a photon has only one tenth of an attojoule (10^{-19} J = 0.8 eV) .

An ideal binary single-photon detector (figure 1.1) returns an electrical signal upon absorption of a photon. The signal level needs to be well defined above the noise (representing a logic '1'); in the absence of an optical signal, a logic '0' is always returned. In practice, real SPDs have many non-ideal characteristics. Single-photon detectors typically have a Detection Efficiency (DE) lower than 100%. In any real photon-counting experiment, photons can be lost before reaching the detector due

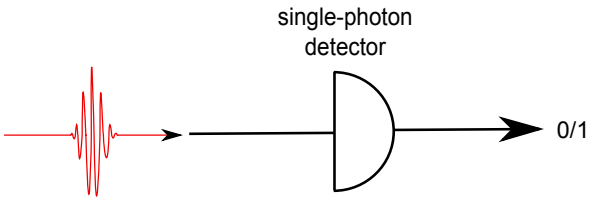

Figure 1.1: Schematic of an ideal binary single-photon detector. When a photon is absorbed by the detector it gives an output electrical signal representing logic '1' and no output signal is given as output in the absence of photon signal (logic '0').

to absorption, scattering or reflection within the experimental environment. Stray light and electrical noise can also sometimes mimic the optical signal. These false detection events are called dark counts. Over the past few decades, researchers have worked to overcome these effects in order to exploit the promising properties of single-photon detectors in real-world applications. Perhaps the most powerful photon-counting technique is the method of *Time Correlated Single-Photon Counting* (TCSPC) [7]. TCSPC is a measurement performed by repeating the experiment with high timing precision a statistically significant number of times. This allows accurate information on the temporal response of the entire experimental system to be obtained. A pulsed source of photons is used. In each clock cycle, an electrical signal is sent to TCSPC electronics acting as 'start' trigger. Simultaneously, a photon travels through the experimental unit. When the photon triggers the SPD, the detector gives a 'stop' signal to TCSPC card. The count of arrival events versus relative time interval is plotted as a histogram (figure 1.2). The trial is considered successful only for photon counts registered within the timing window of the measurement. Moreover, as the data can be binned with very high timing resolution (binning or time-tagging down to 4 ps is common in modern TCSPC cards), the contribution of randomly occurring dark counts can be easily eliminated. The shape of the histogram is determined by the convolved instrument response of the entire unit. If the optical source and the TCSPC card have a narrower instrument response, SPD will dominate the shape of the histogram. The Full Width at Half Maximum (FWHM) of the histogram is an important figure-of-merit, benchmarking the timing response (jitter) of a detector.

TCSPC applications were originally developed using photomutliplier single-photon detectors. In many TCSPC applications, commercially available Silicon Single-

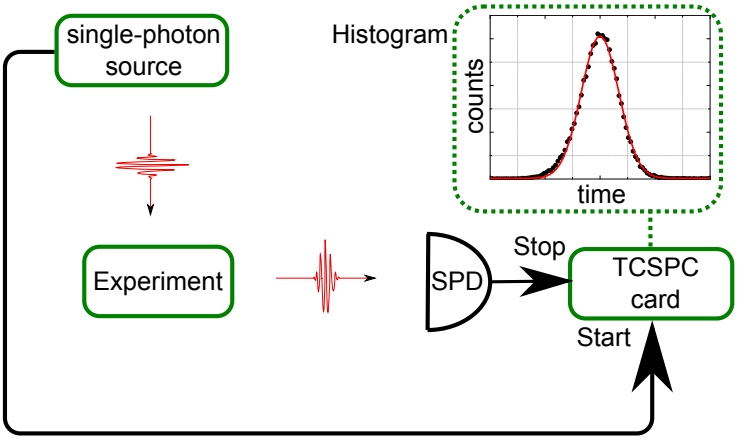

Figure 1.2: Schematic illustration of the time correlated single-photon counting (TCSPC) technique. Ideally, a single-photon source generates a electrical signal and a single-photon at the same instant of time. The electrical signal starts the TCSPC timing card, while the photon travels through the experiment and is detected by the single-photon detector (SPD) in the end. The electrical signal from SPD stops the TCSPC timing card. This process is repeated several times to build a histogram of detection events.

Photon Avalanche Photodiodes (Si-SPADs) are now preferred. These detectors offer DE of ∼45% at 800 nm [8]. The availability of high performance SPDs has a very strong bearing on the choice of wavelength for advanced photon-counting experiments. Reliance on Si-SPAD technology has limited the choice of wavelength to ∼800 nm in many challenging single-photon counting applications such as free-space or fibre optic Quantum Key Distribution (QKD) [9, 10], quantum optics for planar waveguide technology [11], single-photon source characterisation [12], fluorescence lifetime imaging [5] and time-of-flight ranging [13]. In many photon-counting applications, there are considerable benefits in moving towards longer wavelengths. Advanced telecommunications technology - a massive global industry - is typically designed for $\lambda = 1550$ nm. 1550 nm is the natural choice for terrestrial fibre-based optical communications due to the availability of low-loss optical fibre (typically 0.2 dB/km loss [14]). This has motivated the telecommunications industry to invest in development of a wide range of ever improving, cost-effective optic components at 1550 nm. In early 2010, single-wavelength (1555 nm) data capacity reached a remarkable 5.1 Tbit/s using components operating at 10 GHz clock rate [15], demon-

strating the momentum towards further advances in telecommunications technology.

Single-photon detection with high DE and low dark count rate has remained a significant challenge and a bottleneck in operating advanced photon-counting applications at $\lambda = 1550$ nm (e.g. long distance QKD [4], waveguide circuits [11]). The use of smaller bandgap semiconductor materials (Ge, InGaAs) in SPADs is an active area of research and development, but the performance of the best InGaAs-SPADs at telecom wavelength falls far short of the performance achieved by Si-SPAD technology at shorter wavelengths [16]. Superconducting materials offer the potential for single-photon detection from X-rays to terahertz wavelengths. A new type of single-photon detector based on superconducting niobium nitride (NbN) nanowire emerged in 2001 [17]. The Superconducting Nanowire Single-Photon Detector (known as the SSPD or SNSPD) operates at ∼4 K (a temperature attainable either with liquid helium or modern closed-cycle cooling technology) and offers infrared single-photon sensitivity with picosecond timing resolution and low dark counts. Developments in this field have been rapid, with many groups worldwide pursuing this promising SPD technology. Advanced SNSPD designs with integrated optical cavities have been reported to have a high intrinsic detection efficiency of 57% at 1550 nm [18]. SNSPDs also offer excellent timing resolution (FWHM ∼35 ps [19]). The narrow FWHM jitter is attributed to non-avalanche working principle of the SNSPD. The benefits of timing resolution and 1550 nm sensitivity have already been demonstrated by running these detectors in record speed, long distance quantum cryptography experiments [20]. Chapter 2 gives an in-depth discussion of SPD technologies based on semiconductors and superconductors. The requirements of different photon-counting applications on SPDs are also elaborated.

This thesis focuses on the implementation of SNSPDs into practical fibre coupled systems for use in advanced photon counting applications, particularly in the realm of quantum information science. Chapter 3 concerns the design and construction of a practical platform for SNSPDs, and a full description of techniques used for electrical and optical detector characterisation. Elsewhere SNSPDs have been studied either in a cryogenic probe station [18] or in liquid He dewars [17]. The need for cryogenic operation is a significant obstacle to the adoption of SNSPDs beyond the low-temperature physics community. Closed-cycle cryocoolers offer a practical solution to this problem by eliminating the need to handle liquid cryogens in order

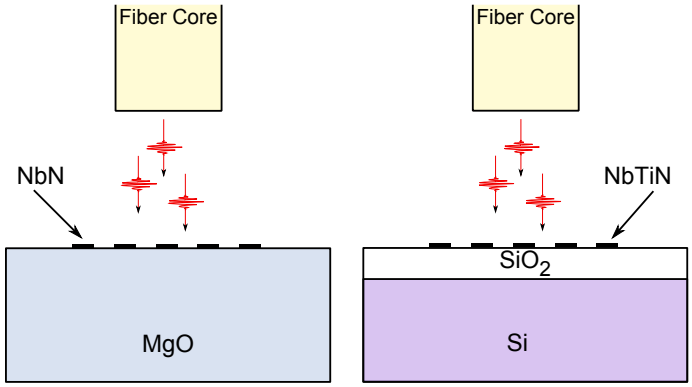

Figure 1.3: NbN and NbTiN SNSPD layer structure: The NbN SNSPD device consists of a NbN nanowire patterned on top of the MgO substrate. The NbTiN SNSPD device consists of a NbTiN nanowire patterned on top of the SiO_2 layer on a Si substrate. The photons are coupled to the SNSPD via an optical fibre. In the case of NbTiN SNSPD, the SiO_2/Si interface acts as a reflector and enhances the absorption of photons by the superconducting nanowire.

to reach 4 K [21], but systems with high performance and multiple detector channels have not yet been implemented. A cryostat based on Gifford-McMahon cryocooler (a closed-cycle cryocooler) to enclose multiple SNSPDs has been constructed and tested in this thesis work. The SNSPDs are fibre-coupled and packaged robustly to retain the optical coupling over repeated thermal cycling. The facilities developed at Heriot-Watt University for full device characterisation at infrared wavelengths are also detailed.

Chapter 4 describes the results of device characterisation measurements on SNSPDs provided by our international collaborators at NICT Japan and TU Delft, The Netherlands that were fibre-coupled and tested at Heriot-Watt University. The NICT devices are NbN nanowires fabricated on a MgO substrate (figure 1.3(a)), with a large area (20 μm $\times$ 20 μm) for efficient fibre-coupling. These devices show a fall in performance with increasing wavelengths. The TU Delft devices consist of (10 μm $\times$ 10 μm) nanowire on an oxidised Si substrate (figure 1.3(b)). The refractive index mismatch at the SiO_2/Si interface gives a strong reflection, enhancing performance at telecom wavelengths [22]. This device is in effect a cavity enhanced SNSPD (similar to [18]) which can be practically fibre-coupled.

Chapter 5 describes the implementation of the multichannel SNSPD system in a new advanced photon-counting application. Integrated quantum photonics [23] promises a paradigm shift in optical quantum information science [24]. The first silica-on-silicon quantum waveguide circuits [11] were originally characterised using Si-SPADs at $\lambda = 804$ nm to perform two-photon quantum optics experiments. In this work SNSPDs are used to characterise these quantum waveguide circuits for the first time [25]. Our successful demonstration of the use of SNSPDs opens the pathway to operating next-generation quantum waveguide circuits at telecommunication wavelengths.

Chapter 6 gives a outlook and conclusion on my thesis work. Since I began this work in late 2007, significant advances have been made in available SNSPD technology and opportunities for new applications have emerged. I will summarise the advances made in my own research, and outline promising future research avenues in this field.

Chapter 2

Review: Single-Photon Detector Technologies and Applications

A single-photon detector utilises the absorbed photon's energy to either (i) excite electrons (photoelectric effect) or (ii) raise temperature (photothermal effect). Several widely used single-photon detector (SPD) technologies [26] based on these phenomena are discussed in detail in section 2.2 following a discussion of important figures of merit for SPDs in section 2.1. Emerging superconducting single-photon detector technologies are discussed in section 2.3. Superconducting nanowire single-photon detectors (SNSPD) came into existence in 2001 and have appealing properties [17]. This developing detector technology is at the heart of this thesis and its evolution is elaborated in detail. In section 2.4, single-photon counting applications are presented along with their specific demands. Scope for the employment of SNSPDs in respective applications is also discussed.

2.1 Performance Parameters of Single-Photon Detectors

The performance of available SPDs is often a critical limitation for photon-counting applications. For example, the spatial resolution of time-of-flight ranging experiments [6] and clock rate of high speed Quantum Key Distribution (QKD) both depend on the timing resolution of the detector [20]. By contrast, single-photon

source characterisation depends on the efficiency and darkcount rate of the detector [12]. This shows that selecting the best possible detector from a range of available options for a chosen application is an important task. The SPD can be considered as a black box, which responds when illuminated by a single-photon. The responses of SPDs have inherent statistical fluctuations. The following statistical characterisation parameters fairly define advantages and disadvantages of various detector types.

2.1.1 Detector efficiency

Efficiency of the detector (η) can be defined as the probability that the detector records a single-photon absorption event [27]. This probability depends on a variety of parameters, i.e. when a detector is exposed to a photon flux only a fraction of photons gets detected due to the following independent probabilities:

- Coupling efficiency ($\eta_{coupling}$): when the active area of the detector is smaller than the spot size of the photon flux, only $\eta_{coupling}$ fraction of photons reach the detector surface due to non-ideal optical coupling to the detector.

- Material efficiency ($\eta_{material}$): depending on the energy band gap of the material, absorption can vary based on the photon wavelength. If the photon energy is less than the band-gap energy of the material then $\eta_{material}$ is zero. $\eta_{material}$ establishes the wavelength dependence of the detector [28].

- Absorption efficiency ($\eta_{absorption}$): only a portion $\eta_{absorption}$ of photons that reach the detector's surface get absorbed. The remaining photons get either reflected or scattered at the surface of the detector or transmitted through the detector. This is mainly due to the structural design of the detector. Anti-reflection coatings and optical cavities can enhance the absorption of photons by the detector [18, 29]. It should be noted that $\eta_{absorption}$ is also typically wavelength dependent.

- Registering efficiency ($\eta_{registering}$): Only $\eta_{registering}$ ratio of absorbed photons register as an absorption event [30]. For example, in a photoelectric system the electron-hole pair generated can get recombined before an avalanche is triggered.

Using the above mentioned probabilities, SPD's system detection efficiency η_{sde} is defined as

$$\eta_{sde} = \eta_{coupling} \times \eta_{material} \times \eta_{absorption} \times \eta_{registering} \tag{2.1}$$

Coupling efficiency ($\eta_{coupling}$) does not depend on the properties of the detector and $\eta_{coupling}$ can be enhanced by improving the optical arrangement for a given detector system. For a perfect coupling system $\eta_{coupling} = 1$. Therefore, intrinsic quantum efficiency (η_{qe}) of the detector is defined as

$$\eta_{qe} = \eta_{material} \times \eta_{absorption} \times \eta_{registering} \tag{2.2}$$

2.1.2 Spectral sensitivity

Dependence of η_{qe} on the wavelength of the incident photon (λ) is explicitly understood from $\eta_{material}$ and $\eta_{absorption}$. In order to meet the demands of a particular photon-counting application, it is desirable to maximise the detection efficiency at the particular operating wavelength. For example, a telecommunication wavelength QKD experiment relies on a highly efficient detector at the 1310 nm / 1550 nm windows. η_{sde} for a specific λ can be enhanced by either engineering the energy bandgap of the absorbing material by modifying the material composition (increases $\eta_{material}$) [31] or by fabricating the detector within a cavity (increases $\eta_{absorption}$) [29]. Altering the device design improves η_{qe} for certain wavelengths and simultaneously suppresses η_{qe} for other wavelengths. Intrinsically for SNSPD devices $\eta_{registering}$ decreases as λ increases and photon energy decreases [32].

2.1.3 Dark count rate

Any response mimicking the detection event from the detector in the absence of a signal photon is called a dark count D [1]. The number of dark counts within a timing window is used to quantify this phenomenon. Dark counts are due to self triggering of the detector by an internal or external noise source. For example, in a photoelectric detector, internal dark counts are due to generation of electron-hole pairs created either by thermal or tunnelling processes instead of the absorption of a photon [28]. The thermally induced dark counts can be mitigated by reducing

the operating temperature of the device. External noise sources include stray light or fluctuations in the electric circuit, which both contribute to the net dark count rate. Some single-photon detectors give dark counts correlated to the single-photon detection event. These dark counts are known as "afterpulses". For example in a InGaAs/InP SPAD, afterpulses are observed due to the trapping and subsequent escape of free charge carriers following an avalanche [28].

2.1.4 Timing resolution

The inherent statistical fluctuation in the time interval between the arrival of a photon at the detector and the subsequent response of the detector is known as the jitter of the detector. Jitter of a detector is quantified by measuring the Full Width at Half Maximum (FWHM) from the plot of statistical distribution of time delay between arrival of a photon at the detector and the observation of an output electrical signal from the detector as shown in figure 1.2. Narrow jitter of a device implies better timing precision for the arrival of the photon. This parameter determines the maximum clock rate at which single-photon counting experiments can be run before errors occur due to Inter-Symbol Interference (ISI) [33]. ISI occurs when the single-photon counts are erroneously recorded in neighbouring clock cycles (i.e. in time domain the adjacent data symbols begin to overlap with each other).

2.1.5 Dead time

Once a detection event takes place, the detector has to be restored to its initial state to be able to detect photons again. The time interval before the device can be reset passively or actively is known as the dead time of the detector (τ). In general, τ can be given as the sum of $\tau_0 + \tau_{rqe}$, where τ_0 is the time where the detector is unable to register the arrival of photon and τ_{rqe} is when a detector operates with a reduced quantum efficiency [34]. For example, in a current-biased superconducting detector, the detection of the photon involves interrupting the supercurrent; the detector will not be able to detect any photons until the supercurrent starts to flow again (τ_0). During the time when the supercurrent start to build and reaches its steady state (τ_{rqe}), the device will be photon sensitive, but will not be as efficient as its steady state value.

2.1.6 Photon Number Resolution capability

The ability of SPD to register the number of photons absorbed by the detector is an additional parameter describing the detector. A Photon Number Resolving (PNR) detector is capable of resolving the number of photons striking the detector at a particular moment of time [27]. SPDs lacking PNR capabilities are binary detectors, where they confirm only presence or absence of photon(s) in a given time window. Binary detectors can be given PNR functionality by either of the following techniques: (a) spatial multiplexing (using a broadly illuminated array of detectors) can resolve photon number by counting the number of detector pixels which fire simultaneously [35], or (b) time multiplexing of the input to a single SPD [36].

PNR feature is intrinsic to bolometric detectors with energy resolution capability for monochromatic photons. The bolometric detector generates an electrical signal whose amplitude is proportional to the energy of the photon. This feature allows these detectors to resolve energy of the single-photons absorbed. Superconducting tunnel junctions and superconducting transition edge sensors are examples of energy resolving detectors [37, 38].

2.2 Semiconductor Based Single-Photon Detectors

The interaction of light with matter strongly depends on the wavelength of the light. Across the electromagnetic spectrum a range of materials have been considered for single-photon detectors. In this section, SPDs based on semiconductors are discussed. In the following section (2.3), emerging SPDs based on superconducting materials are reviewed.

2.2.1 Photo-Multiplier Tubes

A photo-multiplier tube (PMT) operates based on the phenomenon of photoelectric emission. Development of PMTs started with the observation of secondary emissive surfaces in 1902 and the current device structure came into existence in 1949 [31]. A PMT contains a photoemissive cathode, a series of dynodes and an anode enclosed

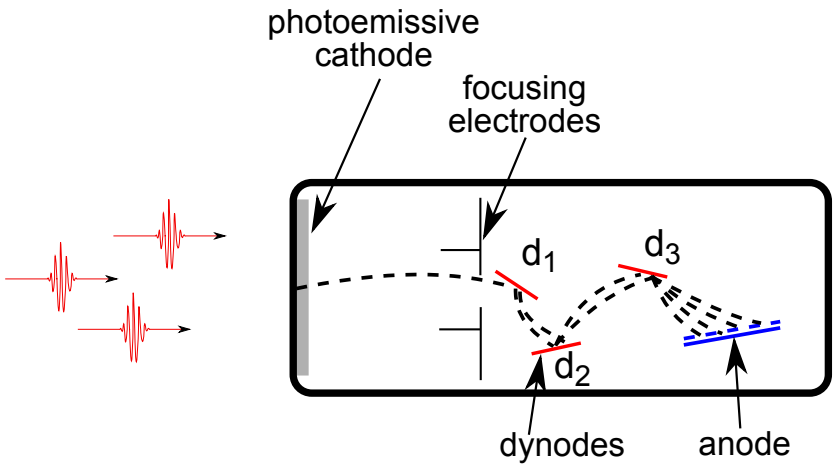

Figure 2.1: Schematic cross-section of a photomultiplier tube. The incoming photons liberate electrons from the photoemissive cathode. Focusing electrodes guide the photoelectrons towards the first dynode (d_1). The successive dynodes (d_2, d_3) emit several secondary electrons for each photoelectron absorbed achieving amplification. The anode collects sufficient number of electrons from final dynode for further amplification by transistor circuits [39].

in a vacuum chamber (figure 2.1). When a photon enters a PMT it is focused onto the photoemissive cathode. If the energy of the photon is larger than the work function(Ψ) of cathode material, a few electrons are emitted into the vacuum. These electrons are accelerated towards the first dynode. The electron count is multiplied due to secondary emission at the dynode. The multiplication factor of electrons at each dynode depends on the energies of incident electrons and inter-electrode potentials. This multiplication process is repeated over a series of dynodes and finally the multiplied electrons are absorbed by the anode. The magnitude of the current measured at the anode is proportional to the intensity of light [31, 39].

The spectral sensitivity of the PMT is regulated by the work function and the thickness of the photocathode material. Better material composition enhances the width and magnitude of the spectral response. Photocathodes made-up of GaAsP crystal with caesium are the most sensitive for visible photons. GaAsP(Cs) PMTs are 40% efficient at 540 nm. For NIR wavelengths, InP/InGaAs junction photocathodes incorporating caesium are sensitive upto 1700 nm. InP/GaAs(Cs) PMTs have efficiency of about 2% at 1550 nm [31]. Dark counts in PMTs are proportional to the applied voltage because they arise due to the thermionic emission and ohmic

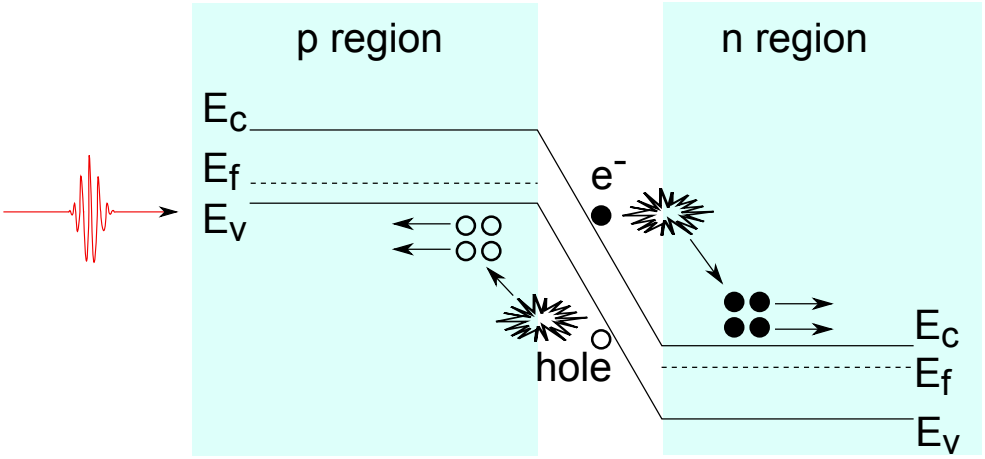

Figure 2.2: Band diagram of semiconductor p-n junction SPAD. Absorption of a photon in the depletion region generates an electron-hole pair by impact ionisation. In the presence of high electric field, these charge carriers multiply due to avalanche [28].

leakage from electrodes. After-pulses are observed in PMTs due to elastic scattering of electrons in first dynode and also due to ionization of residual gases in PMT. Traditional PMTs have a jitter of ∼400 ps due to the series of discrete dynodes used for secondary emission. In order to reduce the jitter, the set of discrete dynodes are replaced by a 2D array of glass capillaries (channels) in a MicroChannel Plate PMTs (MCP-PMTs) [31]. When an electron enters a capillary it bounces of the channel wall; this results in a secondary emission. A set of secondary emission events would have occurred by the time the electrons exit the channel. MCP-PMTs have a jitter around 25 ps FWHM. PMTs are widely employed in fluorescence spectroscopy applications [40] due to the fast temporal response, high sensitivity and large collection area (⌀∼mm). The disadvantages of PMTs are that they are bulky, fragile and expensive.

2.2.2 Single-Photon Avalanche Diodes

Silicon detectors: Silicon Avalanche PhotoDiodes (Si-APDs) are solid state substitutes to photomultiplier tubes. In an APD, light is absorbed in the depletion region at a semiconductor p-n junction which creates an electron-hole pair (figure 2.2). The photo-generated electrons and holes are accelerated by a potential difference

maintained across the device. The accelerated charge carriers collide with the lattice and generate secondary electron-hole pairs with high kinetic energy triggering repeated secondary pair generation. This avalanche multiplication is responsible for the internal gain in APDs. APDs are reverse biased slightly above the avalanche breakdown voltage, with no current flowing, in order to make APDs sensitive to single-photons [28]. This mode of operation is called Geiger mode. In this mode, a single electron-hole pair generated by the absorption of a single-photon can trigger a strong avalanche (note this is not a destructive phenomenon such as in Zener breakdown). Such APDs are called Single-Photon Avalanche Diodes (SPADs). In such conditions, a macroscopic current can be generated by the avalanche due to a single-photon. Once a photon has been detected the avalanche is quenched either passively [41, 42] or actively by bringing down the bias voltage below the breakdown voltage. This prepares the SPAD for next photon detection [28]. Dark counts in Si-SPADs are due to the current generated by electron-hole pairs created in the device in the absence of light due to thermal energy or by tunnelling current. Si-SPADs are sensitive from visible to near-infrared wavelength, with a cut-off at 1.1 μm due to the bandgap of Si ($E_g^{Si} = 1.1$ eV).

InGaAs/InP detectors: Semiconductors with $E_g < 1.1$ eV are employed to make SPADs sensitive to telecommunication wavelength photons. Separate Absorption and Multiplication (SAM) APD structure is used to optimise electron-hole pair generation and avalanche multiplication separately as in figure 2.3(a). Electron-hole pair generation region is designed as a lightly doped thick region favouring absorption of single-photons. The avalanche multiplication region is designed as a heavily doped thin region (InP) in order to maintain the very high electric field required for avalanche multiplication. This technique has made InGaAs/InP SPADs sensitive to telecommunication wavelength photons. Integration of these detectors with resonant cavities has the potential to improve efficiencies of these devices dramatically at telecommunication wavelengths [43].

InGaAs/InP SPADs have a significant drawback in the form of high dark count rates. High dark counts due to after-pulsing is a characteristic feature of InGaAs/InP SPADs. The increased probability of afterpulsing is due to the trapping of carriers at the InGaAs and InP interface (see figure 2.3(b)). Minority carriers get trapped in trap energy levels in between the conduction band and the valence band

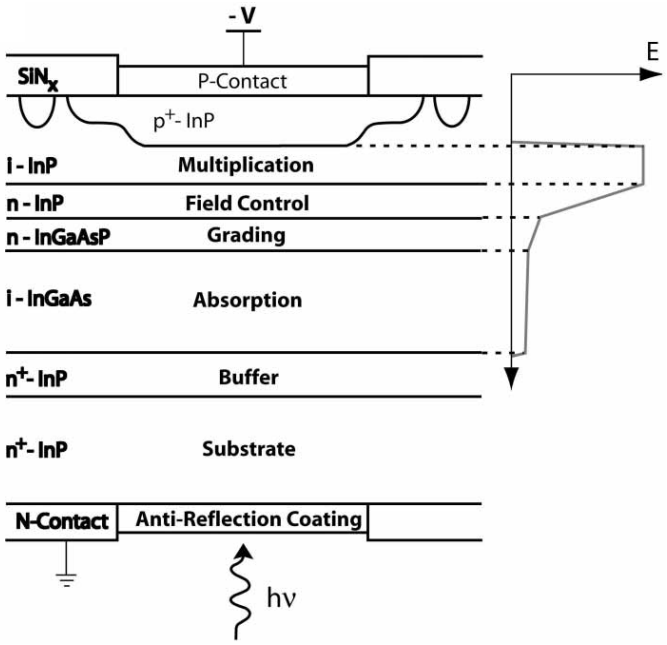

(a)

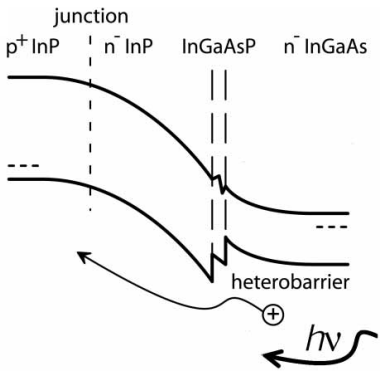

(b)

Figure 2.3: InGaAs/InP SPAD structure: (a) schematic cross-section of a Seperate Absorption and Multiplication (SAM) SPAD. (b) band diagram shows the trap energy levels at the InGaAs/InP interface. Figure reproduced from reference [28].

at the interface. As time elapses, these free carriers escape from traps and re-trigger avalanche multiplication. Afterpulsing is mitigated by quenching the device as soon as the avalanche is observed. This suppresses the secondary emission (weakens the avalanche) and subsequently reduces the number of free carriers getting trapped in interface energy levels. Therefore, SPADs are operated in gated mode by repeatedly biasing above the breakdown voltage only for a short period of time ($t_{gate} \sim 200$ ps). Sensing weak avalanches in gated mode is challenging due to the capacitive response of SPADs. Self-differencing circuits [16, 44] and sine wave gating [45] are used to observe weak avalanches at 1-2 GHz repetition rate.

Self-differencing circuits enable the study of the initial growth of avalanches. The spatially dependent studies of avalanche triggering have shown that multiple avalanches take place independently within a detector's active region [46]. When observed on an oscilloscope, the amplitude of the externally observed initial avalanche pulses depends on the number of photons absorbed, resulting in a PNR functionality [47]. This technique may be simpler to implement than spatially multiplexed PNR detectors [48]. 1 GHz run PNR detectors with ∼74% detection efficiency have been demonstrated using Si-SPADs at $\lambda = 600$ nm [49].

Frequency Up-Conversion Detectors: Integrating efficient Si-SPADs at visible frequencies with a non-linear process of frequency up-conversion can improve telecommunication wavelength detection efficiencies [50, 51]. In this non-linear scheme, a Periodically Poled Lithium Niobate (PPLN) crystal is strongly pumped with ω_p photons and with weak telecommunication photons ω_1. PPLN is quasi-phase matched to ω_p and ω_1 photons. A single output photon of sum-frequency ω_2 is generated by energy conservation. The output ω_2 is engineered to coincide with most sensitive spectral response of the Si-SPAD. The disadvantage of this technique is the low conversion efficiency. The conversion efficiency after considering the coupling losses and internal transmission loss is ∼30% and further considering the filtering and η_{qe} of Si-SPADs the net η_{qe} observed experimentally is only 5-7% [52].

2.3 Superconductor Based Single-Photon Detectors

The superconducting state: Superconductivity is a quantum mechanical phenomenon involving the resistance-free flow of electric current through a material. The other basic phenomenon observed in superconductors is the Meissner effect i.e. the magnetic fields are forcibly expelled from the superconductor. This magnetic field expulsion is due to the electrical screening currents running across the superconductor's surface. The Meissner effect differentiates perfect conductors from superconductors. Bardeen, Cooper and Schrieffer (BCS) theory can be used to explain superconductivity [53, 54]. BCS theory assumes that in superconductors, electrons are able to form pairs (Cooper pairs) overcoming the mutual Coulomb repulsive force, a phenomenon determined by polarisation of crystal lattice and mass of the lattice nuclei. The temperature of the material needs to be maintained below a critical temperature (T_c) to allow the formation of Cooper pairs. Superconducting state depends not only on temperature but also on current density and magnetic field. The superconducting state is destroyed when the current through the material is increased beyond a critical current I_c or when the material is subject to strong magnetic field beyond critical magnetic field H_c. A minimum energy gap exists between a Cooper pair's ground state and excited state. This energy gap is expressed as $2|\Delta|$. The parameter $|\Delta|$ is defined, in terms of Debye frequency (ω_D), density of states at the Fermi level for electrons of one spin orientation ($N(0)$), strength of interaction potential in between the electrons in Cooper pairs (V), Plank's constant (h) and Boltzmann constant (k_B), as [53]

$$|\Delta| = 1.76 k_B T_c = 2h\omega_D \cdot e^{-1/N(0)V} \tag{2.3}$$

equation 2.3 is valid for $N(0)V << 1$, known as the weak-coupling approximation.

Material choice: Many metals in the periodic table (Hg, Pb, Nb, Al etc.) if cooled to a sufficiently low temperature, exhibit a superconducting transition. Typically, metals have T_c below 10 K (bulk Nb shows highest T_c 9.2 K). Metallic compounds such as nitrides and A15 compounds show increased transition temperatures (upto ∼20 K) while still obeying BCS theory. MgB_2 has two super-

Material	T_c (K)
W	0.178
Al	1.2
Ta	4.47
Pb	7.2
Nb	9.2
NbN	17.0
NbTiN	18.0
MgB_2	38.0
$YBa_2Cu_3O_7$	92.0

Table 2.1: Superconducting materials with their respective critical temperature T_c [55].

conducting energy gaps which permits superconductivity at higher temperatures (38 K). By contrast, the cuprate high-temperature superconductors (high-T_c) do not conform to standard BCS theory and exhibit critical temperatures above 30 K. $(Sn_{1.0}Pb_{0.5}In_{0.5})Ba_4Tm_4Cu_6O_{18+}$ shows the highest critical temperature of ∼163 K. Table 2.1 [55] lists some superconductors with their T_c.

2.3.1 Superconducting Tunnel Junctions

Superconducting Tunnel Junctions (STJs) [37] are formed by sandwiching a thin insulating Al_2O_3 barrier trap ($T_c^{Al} = 1.17$ K) in between two thin Ta or Nb superconducting absorber films ($T_c^{Ta} = 4.47$ K, $T_c^{Nb} = 9.25$ K). Operation of the STJ is summarised in figure 2.4. When a photon strikes the superconducting absorber, which is maintained well below the superconductor's critical temperature (below 1 K), charge carriers are generated depending upon the energy of the photon. These charges tunnel across the thin barrier layer resulting in a temporary measurable current. The current signal depends upon the tunnelling, recombination and inelastic scattering of carriers in the system. For photon energies between 1 eV and 1 keV, Nb STJs have energy resolution between 0.13 eV and 4.3 eV FWHM [56]. Spectroscopic advantages due to this energy resolution capability have been demonstrated by studying multiple fluorophores of biological samples using STJs [57]. Overall, the need for < 1 K temperature and the rapid development of other superconducting single-photon detector techniques has hindered the widespread use of STJs outside

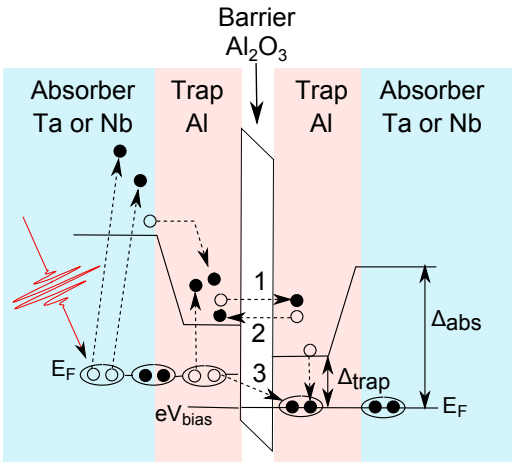

Figure 2.4: Energy band diagram of a Superconducting Tunnel Junction. The absorbed photon in the absorber region generates quasiparticle charge carriers. These charge carriers tunnel across the thin barrier resulting in a measurable current [56].

astronomy and low-temperature physics communities.

2.3.2 Superconducting Transition-Edge Sensors

The Superconducting Transition-Edge Sensor (STES) [38, 58, 59] is a quantum calorimeter as shown in figure 2.5(a). The operating principle can be summarised as follows: when a photon is absorbed the temperature of the absorber section increases. It cools down slowly by dissipating heat into the heat sink via the weak link. The thermal fluctuation is observed by the thermometer and recorded as a single-photon detection event. In the case of the STES, for visible or infrared photons the absorber is tungsten, W (∼20 nm thick) film on a silicon substrate. The Si substrate is maintained at 40 mK in an adiabatic demagnetisation refrigerator acting as the heat sink. The weak thermal link is the low electron-phonon coupling in tungsten. The tungsten film (absorber) switches from superconducting to normal state with a transition width less than 1 mK (T_c ∼178 mK). The detector is voltage-biased to maintain the tungsten film at the midpoint of the superconducting-to-normal transition by negative ElectroThermal Feedback (ETF). When a photon is absorbed by the tungsten film, the generated photoelectron heats the tungsten electron system. As the temperature increases, the current drops due to the increased resistance (thus

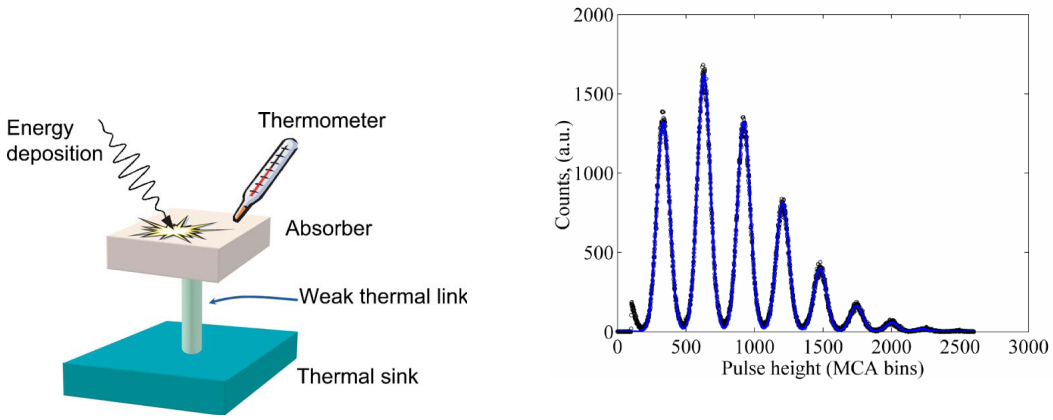

(a) (b)

Figure 2.5: Schematic of a quantum calorimeter, Poissonian statistics of a weak photon source is observed using a photon number resolving STES. Figures reproduced from: (a) reference [29] , (b) reference [58]

the device acts as a thermometer). The sensor recovers subsequently due to reduction in Joule heating. The energy of the photon can be determined by the total sum of the product of current change and the bias voltage $V_{bias} \int \delta I(t) dt$. The current change is read out by Superconducting QUantum Interference Device (SQUID) array amplifiers.

STESs have high detection efficiency at visible and near infra-red wavelengths. The current world record detection efficiency $\eta_{qe} = 95\%$ at 1556 nm has been demonstrated by embedding the tungsten within an optimised optical structure to enhance the absorption of the 1556 nm photons [58]. Energy resolution (FWHM) of 0.29 eV has been shown for this device. Due to the excellent energy resolution STES can be used for photon number resolution [59] and have the ability to resolve up to 7 photons per pulse as shown in figure 2.5(b). These devices also have very low dark count rates (= 1/1000 s). The disadvantages of STES are poor readout recovery time of ∼100 ns, they need very low temperature (40 – 300 mK) to operate and are susceptible to triggering by background black body radiation.

2.3.3 Superconducting Nanowire Single-Photon Detectors

Superconducting Nanowire Single-Photon Detectors (SNSPDs) were first developed based on photon induced transitions of the nanowire from superconducting state to normal state [17]. SNSPDs are most commonly fabricated by patterning nanowire structures on NbN ultrathin films. It is possible to grow NbN ultrathin films (∼4 nm) and still have reasonable critical temperature because the coherence length of the NbN is ∼7 nm [60]. The best 4 nm thick NbN thin films show a critical temperature ∼9 K. NbN is preferred over high-T_c superconductors because the latter are difficult materials to process into working devices. NbN is physically stable over repeated thermal cycling and is chemically inert to materials used in standard lithographic processing. These features of NbN allow fabrication of high quality thin films. Moreover, NbN thin films have an energy gap of 2.6 meV [60], orders of magnitude lower than typical photon energies, which makes it sensitive over a wide spectrum of photons from visible to mid-infrared (for example, energy of a single 1550 nm photon is 0.80 eV).

Device operation: Superconducting Nanowire Single-Photon Detectors (SNSPDs) [17] consist typically of 4 nm thick, 100 nm wide nanowires. The nanowire is maintained well below its critical temperature and DC biased just below its critical current (figure 2.6(a)). Individual photons have enough energy to disrupt hundreds of Cooper pairs in a superconductor thereby forming a resistive region called the *hotspot* (figure 2.6(b)). The hotspot resistance forces the supercurrent to bypass this region (figure 2.6(c)). Since the width of the nanowire is typically ∼100 nm, the local current density around the hotspot quickly (few ps) increases beyond the critical current density. This creates a resistive barrier across the nanowire which increases due to the Joule heating and generates a measurable output voltage pulse across the nanowire (figure 2.6(d)) [61]. The energy of the hot electrons is coupled to the phonons via electron-phonon scattering, as shown in figure 2.7, with a time constant τ_{e-ph} ($\approx$ 10 ps) [62]. The phonon-phonon scattering then couples the energy into the substrate with a time constant τ_{ph-sub}. A fraction of the energy is backscattered into the electron system due to the lattice mismatch between the superconducting nanowire and the substrate. The substrate acts as a heat sink at temperature $T_{substrate}$ [62]. Then the nanowire recovers its superconducting state (figure 2.6(a)).

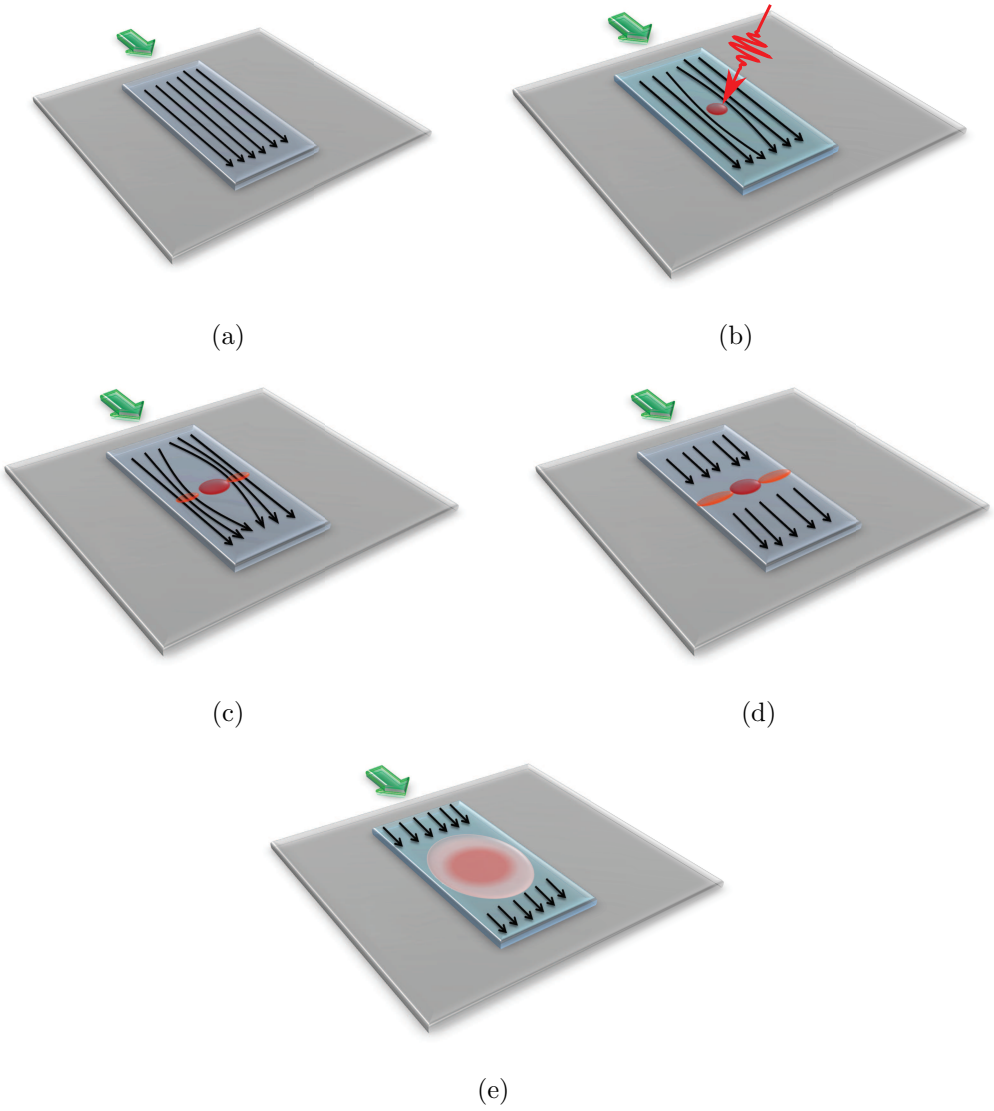

Figure 2.6: Schematic of operating principle of SNSPD: (a) the superconducting nanowire is maintained well below its critical temperature and DC biased just below its critical current. (b) When a photon is absorbed by the nanowire, the photon generates a *hotspot* in the nanowire causing the nanowire to lose its superconducting state in the hotspot region, (c) which in turn forces the supercurrent to flow along the periphery of the hotspot. Since the NbN nanowires are narrow, the local current density around the hotspot increases exceeding the superconducting critical current density. (d) This results in a resistive barrier across the width of the nanowire [17]. (e) Joule heating aids the growth of large normal region and thus a measurable output voltage pulse [61].

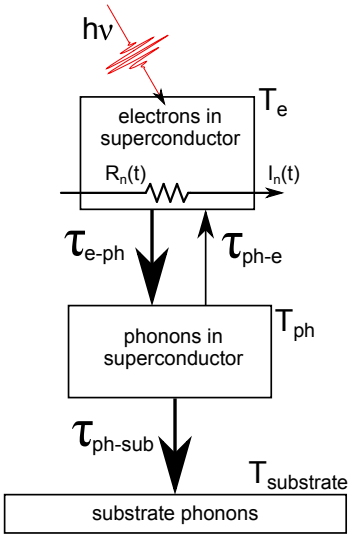

Figure 2.7: Schematic of the energy relaxation process. The electron system and phonon system of the nanowire are at temperatures T_e, and T_{ph} respectively. The energy of the photon is absorbed by the electron system which raises its temperature (T_e) creating a local hotspot with resistance $R_n(t)$. The current through the nanowire $I_n(t)$ heats the electron system due to Joule heating and further increases $R_n(t)$. The energy in the electron system is coupled to the phonon system, via electron-phonon scattering, with a time constant τ_{e-ph}. The phonons then couple the energy to the substrate, via phonon-phonon scattering, with a time constant τ_{ph-sub}. The substrate acts as a heat sink which is maintained at a lower temperature $T_{substrate}$. τ_{ph-e} represents the time constant of the energy returned via phonon-electron scattering. [62]

The generation of measurable output voltage pulse from an SNSPD, biased at I_{bias}, can be modelled as shown in figure 2.8(a). Inductor L_k and resistor R_n represent the kinetic inductance of the superconducting nanowire and the hotspot resistance respectively [63]. Absorption of a photon forms a resistive barrier, which can be simulated as opening of the switch. Introducing R_n into the circuit diverts the current through the load impedance Z_0 (typically 50 Ω << R_n). The LR circuit imposes a time constant of $\tau_{fall} = L_k/(Z_0 + R_n)$ on the decay of I_{bias} through the nanowire. This τ_{fall} limits the rise time of the voltage pulse across Z_0. The simulated voltage rise is shown in figure 2.8(b). As the current flowing through the nanowire decays to a return current (I_r), the electrothermal feedback reduces the Joule heating in the nanowire. In this model, the switch closes again to dump R_n from the

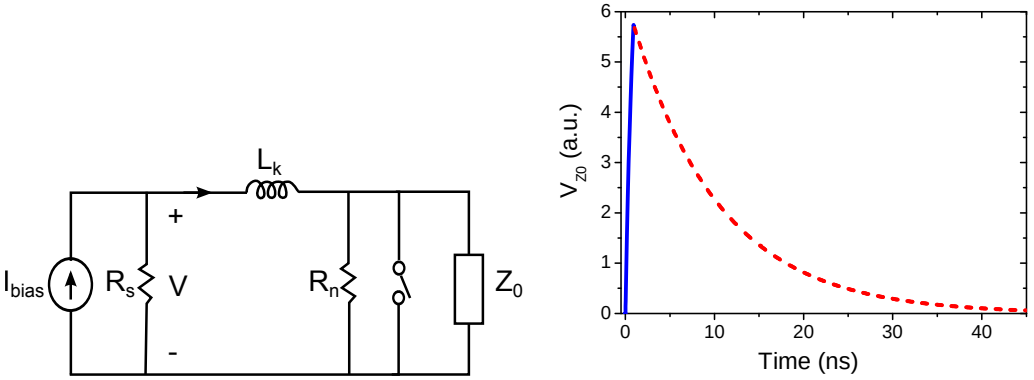

(a) (b)

Figure 2.8: (a) Electrical equivalent circuit of an SNSPD. L_k and R_n is the kinetic inductance and hotspot resistance of the SNSPD respectively, The SNSPD is current biased at I_{bias} and the absorption of a photon is simulated by opening and closing the switch. An output pulse is measured across the load resistor Z_0 [63]. (b) Values of $L_k = 500$ nH and $R_n = 500\ \Omega$ have been used for this simulation. The solid blue line is the leading edge of the SNSPD output pulse while the dotted red line is the trailing edge of the output pulse.

circuit, representing the initiation of the recovery of supercurrent in the nanowire. The current recovers from I_r to I_{bias} with a longer time constant $\tau_{rise} = L_k/Z_0$ due to the reduction of total resistance in the circuit (dashed red curve in figure 2.8(b)). The SNSPD remains insensitive to photons while the supercurrent decays and eventually recovers to a re-triggerable level. This insensitive time period is known as the *dead time* of the detector. The dead time of the detector can be reduced considerably by either reducing the value of L_k (shorter nanowire) [64] or including a resistance R_s in series to the device, thereby reducing the decay time [61].

Detector design: Focusing an optical spot at $\lambda = 1550$ nm on to a 100 nm wide nanowire is not feasible. In order to enhance optical coupling (η_c), a nanowire meander is written typically across a 10 μm $\times$ 10 μm [17] or 20 μm $\times$ 20 μm area (figure 2.9(a)) [68]. These devices show system detection efficiencies of about 2-3% at 1550 nm, 1 kHz DCR and $\sim$2 K. η_{sde} increases as the energy of the photon increases (i.e. lower wavelength photons) [32]. Quantum efficiencies (η_{qe}) of 57% for 1550 nm photons, at 1.8 K, have been demonstrated by embedding a 3 μm $\times$ 3 μm nanowire meander inside an optical cavity [18]. Shorter nanowires possess better

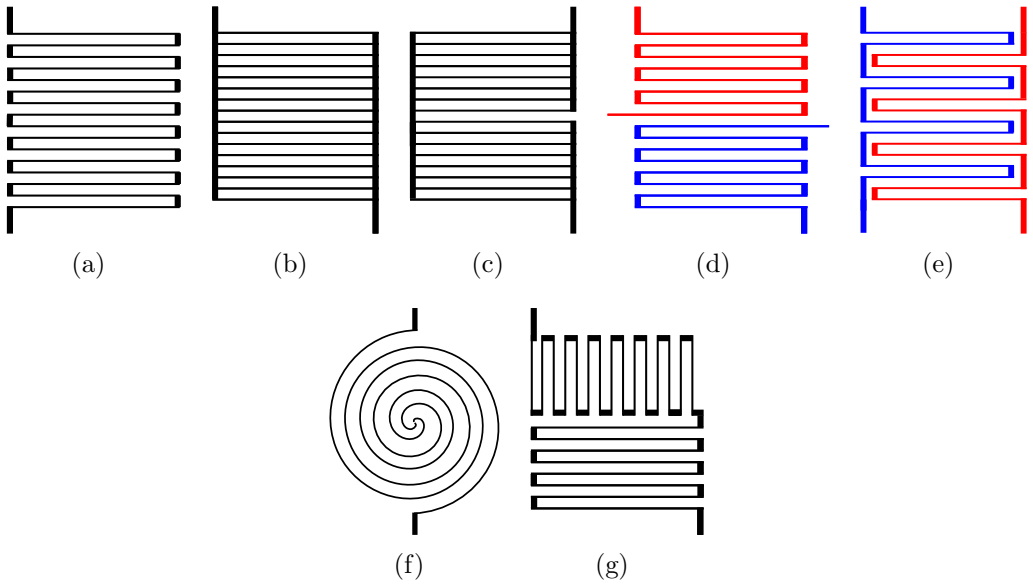

Figure 2.9: SNSPD nanowire patterns: (a) meander [32], (b) parallel nanowire [65], (c) parallel nanowires in series [66], (d) multi-element SNSPD [34], (e) spatially interleaved multi-element SNSPD [34], (f) spiral [67] and (g) perpendicular meander SNSPDs [67]. Each pixel in a multi-element SNSPD is shown in a different colour.

intrinsic quantum efficiency due to their superior uniformity. Fabricating uniform 20 μm $\times$ 20 μm nanowires without constrictions remains a challenge. Constrictions in the nanowire do not allow the detector to be biased at a high current, consequently lowering η of the device [69]. For a given defect density, reducing the area of nanowire meander improves the quality of the nanowire's uniformity. 3 μm $\times$ 3 μm devices have been shown to be highly uniform exhibiting higher efficiency. The challenge is to couple the light to this small 3 μm $\times$ 3 μm area. L_k is lower for shorter nanowires, resulting in a shorter dead time (τ_{rise}). This makes shorter nanowires highly suitable for high speed applications. The load impedance can also be increased to reduce τ_{rise}. However, τ_{rise} suppression has a limitation. If τ_{rise} is reduced beyond a point, the returning current in the nanowire does not allow the hotspot to decay completely due to Joule heating. This results in a self-heating hotspot [70]. This self-heating hotspot causes the nanowire to enter into a "latched" state, forbidding further detection of photons. Alternatively, inductance of the detector can be reduced by writing a set of parallel nanowires [65] (figure 2.9(b)) or a series of parallel nanowire blocks [71]

(figure 2.9(c)) rather than meandering across a given area. Even though reduction in dead time has been observed for these devices, the latching phenomenon and other key parameters such as efficiency and jitter of these devices have not been reported yet.

Multi-Element Superconducting Nanowire Single-Photon Detectors (MESNSPDs) offer another solution to improve the single-photon count rate. MESNSPDs consist of spatially interleaved nanowires meandering across an active area (figures 2.9(d) & 2.9(e)). Each element is independently current biased and requires an individual readout [34]. The lack of cross talk between elements tackles the problem of longer dead time without compromising on L_k or Z_0. Multiple elements firing simultaneously result in Photon Number Resolving MESNSPDs [72]. The complexity of multiple bias and readout can be mitigated by connecting the nanowire elements in parallel, provided the hotspot creation in one element does not affect the superconducting state of the remaining elements. This is achieved by introducing series resistance in each nanowire element. The resistance values are carefully chosen such that the hotspot formation diverts the current into Z_0 instead of flowing into the remaining nanowires. When 'n' elements fire simultaneously, current flowing into Z_0 increases by a factor of 'n'. This results in a '$\sim$n' times taller observable voltage pulse which acts as a PNR-SNSPD [35, 73]. Another technique to observe multiphoton events using SNSPDs is to reduce the bias current and rely on the absorption of multiple photons to form a resistive barrier across the nanowire [17, 74]. However, at low bias the SNSPD is less efficient, so this multiphoton detection regime is hard to exploit in practical applications.

2.4 Single-Photon Detector Applications

Constant advancements in photon-counting applications, such as quantum key distribution, motivate the development of improved single-photon detectors. Detectors often undergo selective evolution targeted at particular applications. The suitability of the novel SNSPD in various areas of research is yet to be investigated. The aim of this section is to understand the specific needs of each of these applications. The section starts off with a discussion of quantum optics applications such as quantum cryptography, optical quantum computing and characterisation of quantum emit-

ters. The section concludes with a discussion of a wide variety of more mature TCSPC applications.

2.4.1 Quantum Key Distribution

Quantum Key Distribution (QKD) [4, 75] is a secure technique for the creation of a cryptographic key via two pairs of conjugate quantum states. The initial idea was developed in 1984 and is known as the BB84 protocol after its inventors C. Bennett and G. Brassard [76]. Alice (traditional information sender) and Bob (traditional information receiver) realise the BB84 protocol using photons with the help of two communication channels: (i) quantum channel to distribute keys and (ii) classical channel to verify security and subsequently send the encrypted message. Either polarisation or phase of the photon is used to represent each conjugate state of the quantum system. The protocol to distribute keys securely is illustrated in figure 2.10. Alice starts the secure communication by sending random information to Bob in the form of polarised photons over a quantum channel from the four chosen states {45,° , 90°, 135° and 180°}. Bob randomly uses a rectilinear {180°, 90°} or diagonal {45°, 135°} polarising filters to detect the polarisation of the photons. Then over a classical (unsecured) channel, Alice only confirms Bob's correct choice of polarisation filters used for different photons. They discard the information related to Bob's wrong choice of polarisation filters (on average 50% of the information). This process is known as *sifting*. The remaining photons are translated into '0's and '1's based on the predefined logic. To confirm the security of the quantum channel, they reveal the actual information content for a set of bits and if an unusually high error rate (Quantum Bit Error Rate – QBER) is observed the presence of eavesdropper is assumed and the keys exchanged are discarded leaving the eavesdropper without any useful information. In the absence of an eavesdropper the remaining unrevealed bits form the key for one-time pad encryption. The entire protocol relies on the fact that the quantum state of the photon cannot be cloned by the eavesdropper (known as no-cloning theorem [77]). First demonstration took place in a lab in 1992 [78] and then outside the lab in 1995 [79, 80]. Currently, commercial QKD systems are also available [81, 82].

The lack of efficient, noise-free telecommunication wavelength SPDs has re-

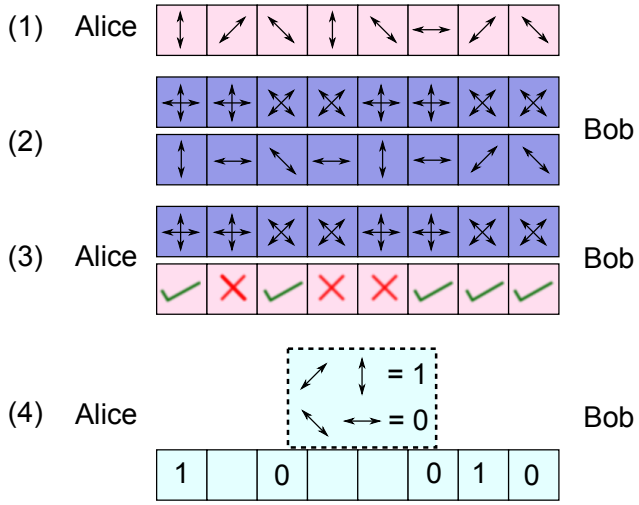

Figure 2.10: Schematic illustration of the BB84 QKD scheme: (1) Alice sends random information to Bob in the form of polarised photons from the four chosen states {45,°, 90°, 135° and 180°}. (2) Bob randomly uses rectilinear {180°, 90°} or diagonal {45°, 135°} polarising filters to detect the polarisation of the photons. (3) Alice verifies Bob's choice of polarisation filters over a classical communication channel. (4) Alice and Bob translate the information into '0's and '1's based on the predefined logic, while discarding the information related to Bob's wrong choice of polarisation filters [4].

stricted QKD to shorter wavelengths which in turn limit the communication distance [10, 83]. Since 1984, various QKD schemes like decoy state QKD [84, 85, 86, 87], the DPSK [88], SARG [89] and other fibre-based schemes [90] have been developed to extend the communication distance by improving the security. Free-space QKD system have also been implemented over 144 km at 850 nm wavelength [91]. Free-space QKD systems can be further developed to communicate securely between Low-Earth-Orbit (LEO) satellite and a ground station [92]. The detector requirements for such applications include large collection area, low dark counts and low timing jitter. Ground to space communications can be benefited from shifting the wavelength to ∼1550 nm by utilising better available photon sources and less solar background spectrum.

The development of high-speed QKD systems depends on the availability of SPDs with low timing jitter. The QKD clock rate >1 GHz has not been achieved mainly due to asymmetric and fairly wide timing jitter of the efficient semiconductor

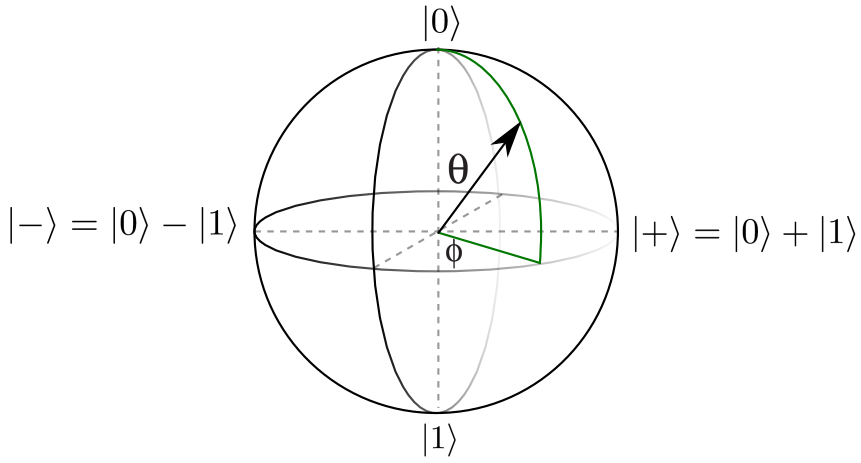

Figure 2.11: Geometric representation of qubit states known as Bloch sphere. Antipodal points of the abstract Bloch sphere is considered to represent $|0\rangle$ and $|1\rangle$. Any arbitrary quantum state can be expressed in terms of states, $|0\rangle$ and $|1\rangle$, and angles, ϕ and θ. The same construction is referred to as Poincaré sphere when used to represent the polarisation states of photons [24].

SPADs. Lower jitter of the detectors allows aggressive gating or time stamping to eliminate dark counts from the QKD system, which will inevitably decrease QBER and improve communication distance. Lower timing jitter detectors will also increase the clock-rate of the QKD system. SNSPDs have helped QKD to achieve secure communication over 200 km of optical fibre at 10 GHz clock rate [20]. Recently high speed (4.8 bits/sec) entanglement based QKD [93] has been demonstrated over a 100 km optic fibre channel using InGaAs/InP detectors [94].

2.4.2 Optical quantum computing

Quantum interference can be achieved in quantum optics by interfering single-photon states. Much of optical quantum information science is based on the exploitation of two-photon quantum interference. A single-photon is used as the basic information carrier called the quantum bit (*qubit*). An arbitrary quantum state of a single-photon is represented by the Bloch or Poincaré sphere with the computational basis states being $|1\rangle$ and $|0\rangle$ (figure 2.11) [95]. Until now the development has been based on path-encoded photons. Path-encoded photons entering modes 'a' and 'b'

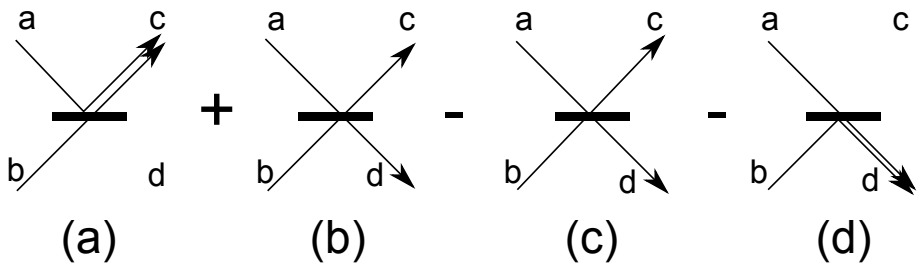

Figure 2.12: Schematic representation of two photons entering a 50:50 beam splitter and four possibilities at the probability amplitude level: (a) top photon is reflected and bottom is transmitted (b) both are reflected, (c) both are transmitted and (d) top photon is transmitted and bottom is reflected [24].

of a 50:50 beam splitter[1] undergo the following transformation expressed in terms of its exit modes 'c' and 'd':

$$|1\rangle_a |0\rangle_b \rightarrow \frac{|1\rangle_c |0\rangle_d + |0\rangle_c |1\rangle_d}{\sqrt{2}} \text{ and } |0\rangle_a |1\rangle_b \rightarrow \frac{|1\rangle_c |0\rangle_d - |0\rangle_c |1\rangle_d}{\sqrt{2}} \tag{2.4}$$

If two distinguishable-photons enter the beamsplitter (figure 2.12), we have 4 possibilities (a) top photon is reflected and bottom is transmitted (b) both are reflected, (c) both are transmitted and (d) top photon is transmitted and bottom is reflected. However if the two photons are identical, in terms of its energy and phase, they interfere with each other. Applying above the equations for $|1\rangle_a |1\rangle_b$ we get:

$$|1\rangle_a |1\rangle_b \rightarrow \frac{|2\rangle_c |0\rangle_d + |0\rangle_c |2\rangle_d}{\sqrt{2}} \tag{2.5}$$

Due to the unitary transformation[2] of the beamsplitter, choices (b) and (c) from figure 2.12 will always have opposite sign and will cancel out each other. This is famously known as the Hong-Ou-Mandel effect [96].

$$|1\rangle_a |1\rangle_b \rightarrow \frac{|1\rangle_c |1\rangle_d}{\sqrt{2}} \text{ and } |1\rangle_a |1\rangle_b \rightarrow -\frac{|1\rangle_c |1\rangle_d}{\sqrt{2}} \tag{2.6}$$

[1] A 50:50 beam splitter is defined as $U_{BS} \equiv \frac{1}{\sqrt{2}} \begin{bmatrix} 1 & 1 \\ 1 & -1 \end{bmatrix}$

[2] An operator U is unitary if $U^\dagger U = I$

In 2001, E. Knill, R. Laflamme and G. J. Milburn showed that scalable linear optical quantum computation is possible (in theory) by using two-photon interference, linear optical elements and projective measurements [97]. The drawback of the KLM protocol was that it relied on perfect photon-number resolving detectors and negligible losses between the photon source and detectors. Subsequent proposals eased the requirement on the detectors and a non-deterministic, coincidence basis Controlled-NOT (CNOT) gate was proposed [98]. Soon after, quantum CNOT gates were experimentally realised using phase shifters and beam splitters [99, 100]. Most of the experiments performed have been restricted to non-PNR single-photon detectors. Upon the availability of dark count free, highly efficient PNR detectors, loophole free test of Bell's inequality and many more QIP experiments can be performed [24].

In summary, these challenging quantum information science experiments require (i) negligible dark counts for better signal to noise ratio, (ii) narrow jitter for narrower coincidence window and (iii) high efficiency at the wavelength of operation for better performance. It has been shown that the product of source efficiency and detector efficiency has to be at least 67% for this scheme to be scalable [101].

2.4.3 Quantum emitters (single-photon sources and FLIM)

A deterministic single-photon source would be highly desirable for quantum information processing applications. The two leading single-photon source technologies are based on (i) III-V semiconductor quantum dots [12] and (ii) NV-centres in diamond crystals [102]. The semiconductor quantum dot can be considered as an artificial atom with electron motion confined in all 3 dimensions. This results in a discrete energy level spectrum. When a quantum dot is pumped by a high energy photon, an electron-hole pair is generated in the quantum dot. This electron-hole pair recombines rapidly and gives out a single-photon. Typically single-photon emission is at λ ~900 nm, but wavelengths upto 1.3 μm are attainable [12]. On the other hand, NV-centres consist of a carbon vacancy (V) near a nitrogen atom (N) in the diamond lattice. The electronic structure of the defect results in a triplet ground state. The emission spectrum of the NV centre is ~600 – 800 nm [102]. In both these cases, to establish a deterministic source a pulsed pump beam is used to excite

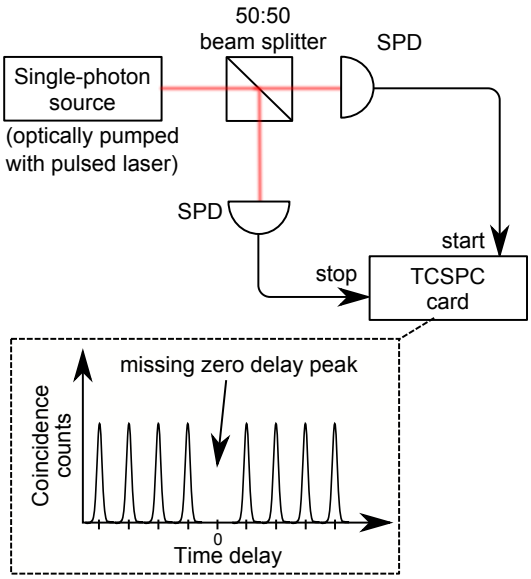

Figure 2.13: Schematic of the Hanbury Brown and Twiss interferometer. The optical path is split into two using a 50:50 beam splitter and the correlation between the photons in the two paths is studied using single-photon detectors (SPDs) and time correlated single-photon counting (TCSPC) card. The expected histogram of a periodically pumped source is shown in the dotted box. The absence of the zero-delay peak confirms the quality of the single-photon source [21].

the electron. The quality of a single-photon source is characterised by measuring the second order correlation function of the source ($g^{(2)}(\tau)$) using a Hanbury-Brown and Twiss (HBT) interferometer [21]. The output optical beam from the source is split into two paths and the coincidence histogram is recorded to study the quality of the single-photon source (figure 2.13). An ideal single-photon source characterised with a SPD possessing no darkcounts will have no coincidence at zero delay. In practice, the coincidence to accidental ratio is often given as the figure-of-merit [103]. Another important performance parameter *source lifetime* can be measured using TCSPC techniques. This requires low jitter pump source, SPDs and TCSPC card as in figure 1.2. In summary, development of high quality single-photon sources at any wavelength heavily depends on availability of a free running, low noise, narrow jitter and highly efficient single-photon detectors. Alternatively, combination of a high quality photon pair source and SPD can be used to build a heralded single-photon source [104].

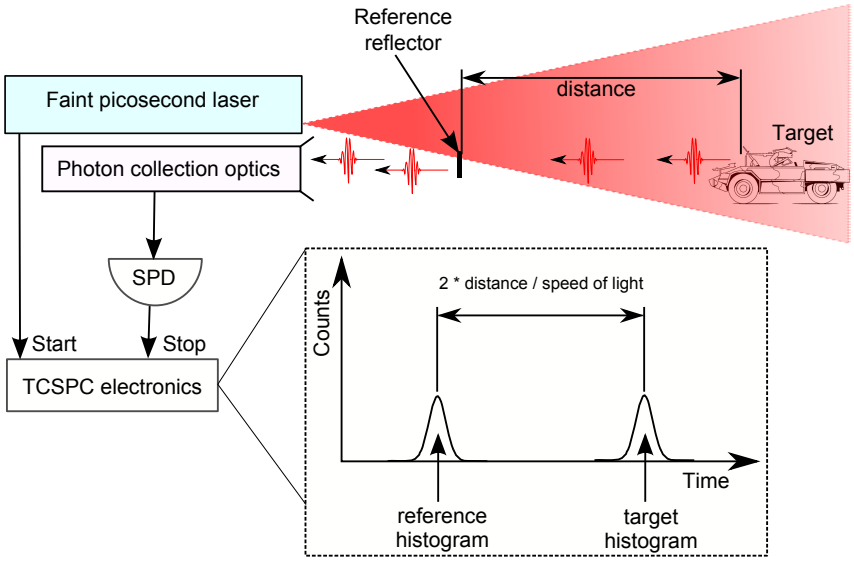

Figure 2.14: Graphic representation of time-of-flight ranging technique: The target is illuminated by a faint picosecond laser pulse and the reflected optical signal (few photons per pulse) is collected and detected by single-photon detector (SPD). The time correlated single-photon counting technique is used to recover the target-distance information. A reference reflector is introduced in the setup to mitigate any drift in timing electronics [6].

Similarly spontaneous emission lifetime in various biological systems can be studied, most commonly known as Fluorescence Lifetime Imaging Microscopy (FLIM) [7]. In biological systems, single-photon detectors are employed to study weak fluorescence from the fluorescent flavin enzyme or Green Fluorescent Protein (GFP) [105] to understand protein dynamics, record ion concentration and record oxygen saturation [106].

2.4.4 Time-of-flight ranging

TCSPC techniques can be used in LIght Detection And Ranging (LIDAR) applications to improve performance. Depth measurement is performed with the help of faint picosecond laser pulses and a narrow timing resolution single-photon detector as shown in figure 2.14. The laser pulses are fired at a target and few reflected photons from the surface of the target are sensed by the SPDs. The time delay between these two events is the time of flight of the photon and is proportional to

the target distance [107, 108]. Any drift in the electronics can be averted by placing a reference reflector in between the target and the source. The timing correlation between the two reflected signals gives the same information. Sub-centimetre depth resolution has been achieved as a result of system timing resolution being ∼70 ps with the target at 300 m [6]. The repetition rate of the pulse is limited by the range of the target. A random pulse pattern can be employed to increase the repetition rate (over 1 GHz) without introducing ambiguity in the range [13]. This technique is based on classic TCSPC methods and relies heavily on the timing resolution (jitter) of the detector. Efficient collection of returning photons is a limitation. A highly efficient wide area detector would be advantageous for this application.

2.4.5 Singlet Oxygen detection

In PhotoDynamic Therapy (PDT) the ability to monitor singlet oxygen would give a powerful diagnostic tool. The amount of singlet oxygen present in the tissue is needed to calculate the dose absorbed in a tissue. The PDT dosimetry has so far evolved based on the technology to measure luminescence emission at 636 nm, 704 nm, 765 nm, and 1270 nm [40]. Singlet oxygen is an important intermediary in many key biological processes. Observation of 1270 nm is highly desired due to the elimination of low ambiance light interference. PMTs are used in such experiments by filtering wavelengths beyond 800 nm or by using a NIR PMT. Currently, these measurements are done with heavy doses or by adding quenchers that signal the presence of singlet oxygen. In real cell environments these techniques may not be feasible. Single-photon detection with energy discrimination is required to confirm the emission of a photon by $^1O_2$ decay [109, 110]. The single-photon detector for this application needs to be highly efficient at 1270 nm and must have a quick recovery time for continuous luminescence detection. Other features such as large active area and spatial resolution are also desirable for this application [111].

2.4.6 Remote sensing of greenhouse gases

The amount of greenhouse gases such as CO_2, CH_4 and N_2O in the atmosphere needs to be monitored, as the knowledge of the location, magnitude and variability on a global basis of sources and sinks of these gases is crucial to predicting changes in

climate. The absorption lines for CO_2, CH_4 and N_2O have been identified as 1.57 and 2.05 μm, 1.65 and 2.29 μm and 3.93 μm respectively [112]. LIDAR technologies are used in remote sensing of these molecules. The properties of scattered light are used to detect the range and other information about the target molecules [113]. Currently, 1.6 μm band is used to study atmospheric CO_2 by the Orbiting Carbon Observatory [114]. Highly efficient single-photon detectors at the desired wavelengths are required to determine the strengths of the laser echoes. Free-running SPDs operating at the wavelengths of interest with low timing jitter, high efficiency and large active area are required for this application.

2.4.7 Testing of Integrated Circuits

There is a high demand for improving practical techniques to debug and to diagnose chip failure of Complementary Metal Oxide Semiconductor (CMOS) logic devices in the semiconductor industry. In CMOS devices, when switching takes place, Field Effect Transistors (FETs) in the saturation mode develop a high field ($\sim 10^5$ V/cm) in the pinch off region of the channel driving electrons to high energy (> 1 eV). Photon emission takes place in order to decrease the electron's energy. As the transistor size decreases, the gate size decreases, reducing the required bias voltage resulting in longer wavelength emissions. Emitted photons are typically in the NIR region [115]. The detection of these single-photons will enable the semiconductor industry to analyse the timing parameters of the CMOS device. NIR single-photon detectors with very low timing jitter, high quantum efficiency and very low dark count rate are required for improving testing of high speed semiconductor circuits.

2.5 Summary

In fields such as astronomy, the life sciences and environmental science the operating wavelength of the photon-counting experiments is decided by the nature. Whereas the other photon counting applications have been mainly developed around 3 wavelength windows — 800 nm, 1310 nm and 1550 nm. The wavelength compatibility between the three major single-photon detector technologies — PMTs, SPADs and superconducting SPDs — is illustrated in figure 2.15. Efficiencies against wavelength

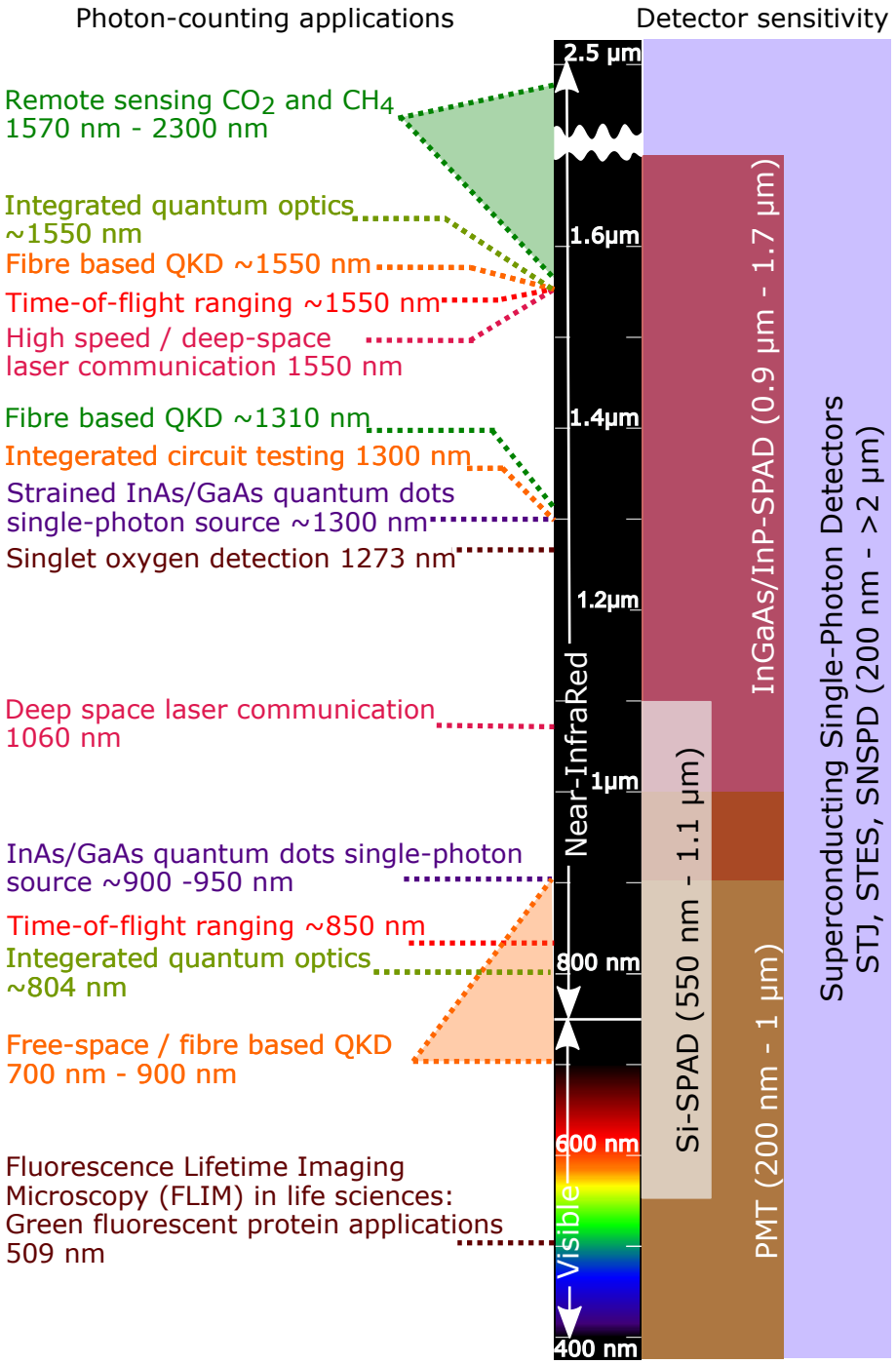

Figure 2.15: Graphic illustrating the compatibility between single-photon counting technologies and applications in terms of operating wavelength.

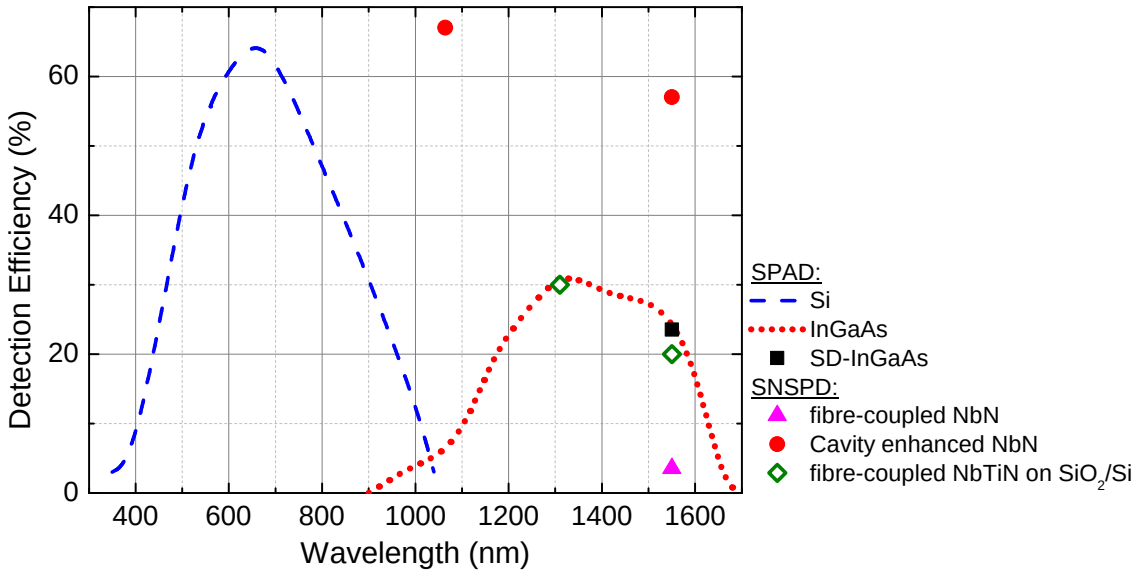

Figure 2.16: Detection efficiencies of commerical Si-SPADs [8] and InGaAs/InP SPADs at 200 kHz Dark Count Rate (DCR) [116] is plotted across a wide spectrum. InGaAs SPADs can be operated at a relatively lower 26.4 kHz DCR using a Self-Differencing (SD) circuit with $\eta = 23.4\%$ [44]. Fibre-coupled NbN SNSPDs have $\eta_{sde} = 3\%$ at $\lambda = 1550$ nm and 100 Hz DCR [68]. Cavity enhanced NbN SNSPDs have been demonstrated to have a higher quantum efficiency of $\eta = 67\%$ at 1064 nm and $\eta = 57\%$ at 1550 nm [18]. In this thesis, fibre-coupled detectors based on NbTiN on SiO_2/Si SNSPDs have been demonstrated to have efficiencies upto $\eta_{sde} = 30\%$ and 20% at 1310 nm and 1550 nm respectively at 1 kHz DCR (discussed in chapter 4).

has been plotted for Si-SPADs, InGaAs SPADs and SNSPDs in figure 2.16. Communication experiments such as QKD and high speed communication have been developed around 1310 nm and 1550 nm wavelength window due to the readily available global fibre-optic networks and supporting technologies. Deep space communication, time-of-flight ranging applications can be centred comfortably around 1060 nm and 1550 nm due the availability of rare earth (ytterbium/erbium) doped fibre lasers and amplifiers. Only InGaAs/InP SPADs or Superconducting SPDs are sensitive beyond 1.1 μm (silicon cut-off wavelength). The other applications have evolved around 800 – 900 nm wavelength namely, short-distance QKD, integrated quantum optics and time-of-flight ranging. This is mainly due to the availability of highly efficient commercial SPDs (Si-SPADs). All these applications could be shifted to 1550 nm wavelength upon the improvement of detection efficiencies

of superconducting SPDs at telecom wavelength. In life sciences applications, the emergence of green fluorescent protein has revolutionised fluorescence lifetime imaging microscopy. In some cases, detection at wavelengths beyond 1.1 μm is required (e.g. singlet-oxygen detection) but in this region the sensitivity of traditional PMT drops dramatically.

The major advantage of the SNSPD is that its broadband sensitivity and free-running operation allows us to characterise any photon-counting application operating across a broad spectrum. Quantum information science applications are a challenging area for testing novel SPD technologies such as SNSPDs. Dramatic improvements in QKD experiments in optical fibre have already been demonstrated using SNSPDs. QKD experiments do not rely on explicit quantum interference effects. Linear optical quantum computing is a tougher experiment to attempt and the recent developments in quantum waveguide circuits provide a promising platform for SNSPD testing.

Chapter 3

Methodology: Construction and Characterisation of the Detector System

Superconducting Nanowire Single-Photon Detectors (SNSPDs) possess excellent timing resolution, wide spectrum sensitivity (visible to NIR) and short dead time [1]. The goal of my thesis research was to integrate these devices into a practical detector system for use in advanced photon-counting applications. A cryostat based on a closed-cycle refrigerator, developed from an earlier prototype designed at the US National Institute of Standards and Technology (NIST) [21] was constructed for this purpose. The challenge was to construct a robust detector system to maintain the chip at <2.5 K (section 3.1), to fibre-couple photons efficiently (section 3.2) and to extract the weak electrical signal while preserving the temporal information (section 3.3). Automated characterisation techniques (section 3.4) were developed to establish the stability of detector performance over multiple thermal cycles.

3.1 Thermal Challenges: Reaching Below 4 K with a Closed-cycle Refrigerator

The most common method for cooling a sample down is to immerse it in liquid helium and reach 4.2 K. Liquid He is expensive, hazardous and demands trained

personnel for correct use [117]. This technique is satisfactory for testing superconducting devices in a low temperature physics laboratory; if the goal is to provide a working device for users in other scientific fields or in industrial applications alternative solutions must be sought. Closed-cycle cryocoolers offer a solution to this problem [118]. The circulating fluid is high pressure, high purity He gas which is enclosed inside the refrigerator eliminating repeated cryogenic handling. Over the past decade, commercially available closed-cycle cryocoolers have improved in terms of both attainable base temperature and reliability [118]. Pulse-tube cryocoolers offer 0.3 W cooling power at 4 K, but have the disadvantage that a water cooled compressor is required. Also the operating principle demands that the coldhead points downwards. These features make it less portable and flexible to work with. The smallest available Gifford-McMahon unit provides 0.1 W of cooling power at 4 K [119] and it features an air-cooled compressor powered by a 13 A plug. Our aim is to construct a cryostat with heat load less than 0.1 W, sufficient to employ this closed-cycle cryocooler to cool multiple SNSPD detectors down to less than 4 K.

3.1.1 Background on Gifford-McMahon cryocoolers

Working Principle [117]: Cryocoolers operate on the principle of a regenerative heat exchanger. By continuously alternating cold and hot fluids through a regenerative matrix a periodic cooling cycle is achieved. The regenerative material is chosen due to its ability to store heat at the target temperature. With the help of rare-earth regenerative materials a two-stage Gifford-McMahon (GM) cryocooler can reach below 4 K [118]. GM refrigerator consists of a compressor, a regenerator, and a cold head. The samples are mounted on the cold head which reaches sub-liquid He temperatures. A circulating fluid acts as the heat transferring medium. High purity helium is circulated through the cold head at high pressure. The cryogen is in an oscillating flow and oscillating pressure at about 1 Hz. As illustrated in figure 3.1(a), the cyclic operation of the fridge can be broken down into the following 4 steps:

- Inlet valve opens when displacer is at the bottom of the cold head.
- Displacer is brought to the top of the cold head. The gas in the top flows

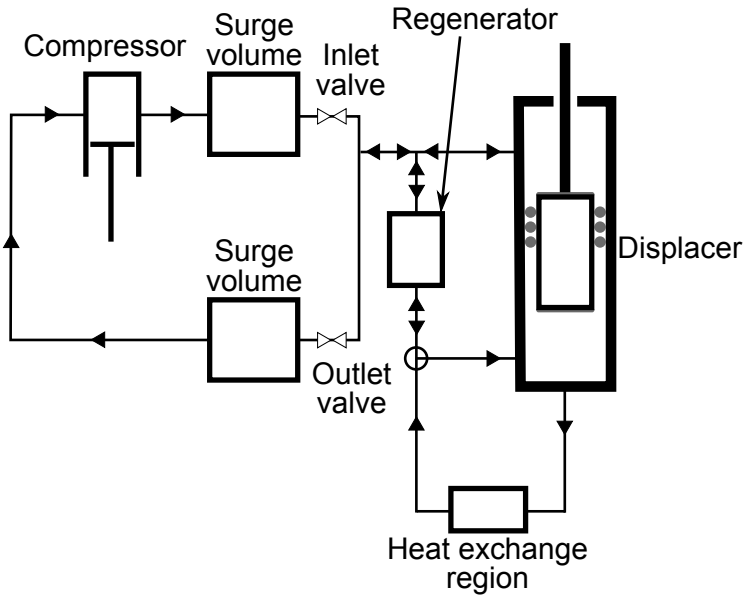

(a)

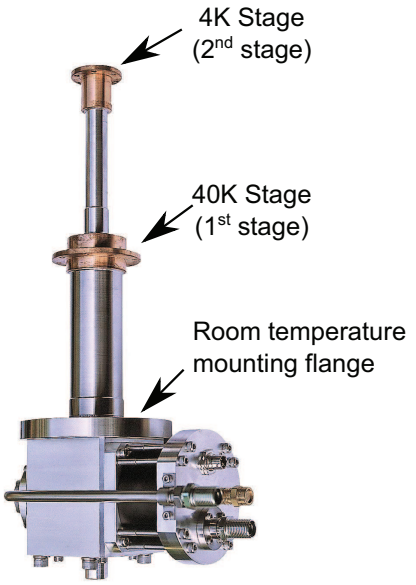

(b)

(c)

Figure 3.1: (a) Heat flow diagram of Gifford-McMahon cryocooler [117]. (b) photograph of Sumitomo cryogenics RDK-101D two stage cold head (40 K and 4 K) and (c) photograph of the compressor, this is very practical because it runs off a standard 13 A electrical socket and is air cooled. Figures (b) and (c) reproduced from reference [119].

through regenerator to the bottom of the cylinder. This flow cools the gas and the volume reduction is compensated by the open inlet valve.

- Inlet valve closes and outlet valve opens. The gas in the bottom of the cold head is allowed to expand to the original system pressure. This cools down the gas further. The expansion pushes excess gas out through the exhaust valve.
- The gas flows through the heat exchange region by forcefully bringing the displacer to the bottom of the cold head (using a motor). The heat from the target region is removed by the flowing gas.
- The gas flows thorough regenerator to the exhaust valve. This heats the gas back to ambient temperature. The compressor at the warm end restarts the pressure oscillation.

Temperatures well below 20 K can now be reached by building a multistage cryocooler using successive GM stages. Two stage GM cryocoolers are now common with first stage reaching (40 – 80 K) and the second stage reaching about 4 K, with the aid of rare-earth regenerative materials [117]. The GM cryocoolers can be operated with the compressor and cold head located at least 10 m apart connected by electrical cables to drive valves and displacer and two flexible gas lines. Since the helium gas circulates within the system, the user need not worry about handling and refilling the cryogen regularly. A Sumitomo RDK101D coldhead (figure 3.1(b)) and Sumitomo CNA-11C compressor unit (figure 3.1(c)) were used to build the cryostat in this thesis work. This unit runs off a 13 A electrical outlet (with 1 kW power consumption) and requires only air cooling.

The oscillating mechanical parts in the cold head have certain disadvantages. The lifetimes of rubbing seals, valves and compressor are limited to 1-3, 3 and 5 years of continuous use respectively [119]. The displacer causes a significant vibration, at 1.3 Hz, at the cold head. GM refrigerators have long thermal cycling times (at least compared to direct immersion in liquid He) and can handle only low sample currents due to small heat load capacity.

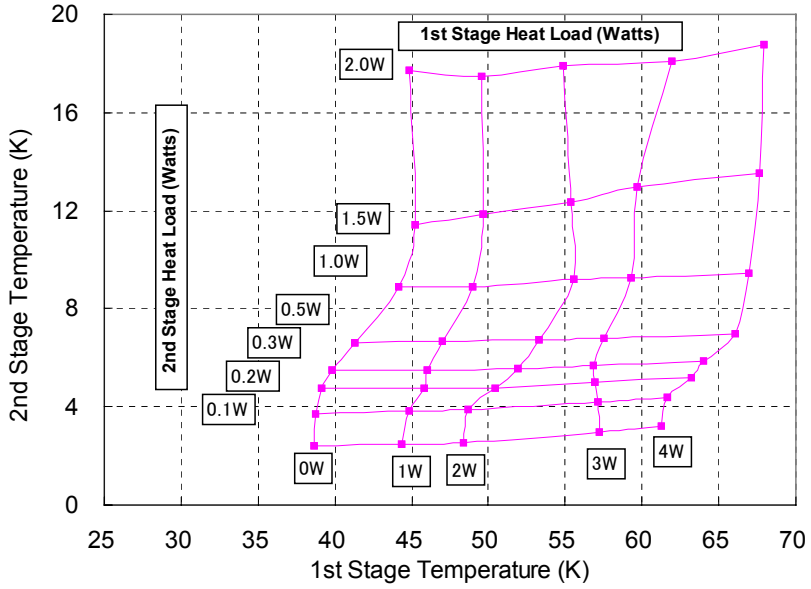

Figure 3.2: Typical heat load map of RDK101D coldhead operating on 50 Hz main electrical power. Reproduced from reference [119].

3.1.2 Design and construction of closed cycle cryostat

The characteristic heat load map of Sumitomo RDK101D cold head is shown in figure 3.2. The load map clearly indicates that temperatures less than 4 K can be targeted for heat load less than 0.1 W. The primary requirement for the closed cycle cryostat design is to reach a stable base temperature of around 2.5 – 4 K for long periods of time so that it can be employed in demanding and time consuming photon-counting experiments. The sample holder is to be mounted on the 4 K stage (sample stage or second stage) of the GM refrigerator. The 40 K stage (first stage of the cryocooler) plays a dual role, it can be used to cool a radiation shield in addition to acting as a heat-sink. Calibrated silicon diode thermometers (Lakeshore DT-670) are mounted on the 40 K stage, the 4 K stage and the sample stage to monitor the respective temperatures.

Conductive heat load: SNSPDs demand an electrical connection for bias and high speed readout, therefore a coaxial cable connection has to be made to each SNSPD from the outside world. These coaxial cables act as heat load on the 4 K stage. Low thermal conductivity is desirable to minimise the heat load at the sample

and simultaneously high electrical conductivity is necessary to allow faithful propagation of high speed electrical pulses. Additionally, the lead connecting the two thermometers mounted on the 4 K stage is also a source of heat. Heat conduction ($\dot{q}_{cond}$) through the leads is calculated using equation 3.1

$$\dot{q}_{cond} = (A/L) \int_{4K}^{300K} \kappa(T) dT \tag{3.1}$$

Where A, L and $\int_{4K}^{300K} \kappa(T) dT$ are the cross-sectional area, length and thermal conductivity between 300 K and 4 K of the lead respectively. We have used two twisted pairs of 110 μm diameter, polyester insulated constantan wire for each thermometer and a brass 50 Ω coaxial, 250 μm diameter, shielded cable for biasing each SNSPD. These wires are $\sim$1 m in length. Brass is chosen as it has lower thermal conductivity than copper and has higher electrical conductivity than stainless steel. Thermal conductivity between 300 K and 4 K for constantan and brass is 5.16 kW/m and 42 kW/m respectively. Considering the maximum capacity of 3 thermometers and 8 sample holders, we get $\dot{\mathrm{q}}_{\text{ const. wire}} = 0.4$ mW, $\dot{\mathrm{q}}_{\text{ brass wire}} = 16$ mW [120]. SNSPDs need only $\sim$20 μA bias current for operation therefore the effect of Joule heating can be neglected. The estimated total conduction load 16.4 mW is six times smaller than our target heat load. Note that due to the poor thermal conductivity of silica, heat load due to optical fibres has not been taken into account. In our case, conductive heat load may not be as significant a problem as the radiative heat load.

Radiative heat load: Radiative heat load can be a significant problem in reaching very low temperatures due to the huge temperature difference between ambient temperature and the cold head. Net heat flow from surface at temperature T_2 (warm) to T_1 (cold), using Stefan-Boltzmann equation [120], is

$$\dot{\mathrm{q}}_{\text{ rad}} = \sigma \mathrm{EA}(\mathrm{T}_2^4 - \mathrm{T}_1^4) \tag{3.2}$$

Where σ is the Stefan-Boltzmann constant [5.67×10^{-8} $W/(m^2K^4)$], A is the surface area of the inner material and $E = \epsilon_1\epsilon_2 / [\epsilon_2 + (A_1/A_2)(\epsilon_1 - \epsilon_1\epsilon_2)]$ where ϵ is the emissivity of the material's surface. Estimating for a worst case scenario, we approximate the surface area of the 4 K stage and 8 sample mounts to a cylinder of length 12 cm and 80 cm diameter ($A_{4\text{K stage}} = 453$ cm^2 [120]). Gold plated sample mounts help to

reduce the black body radiation due to their high reflectivity ($\epsilon_{4\text{Kstage}} = 0.02$ [120]). The outer enclosure cylinder is 50 cm tall and has 164 mm inner diameter. The stainless steel vacuum can has low reflectivity ($\epsilon_{300\text{K}} = 0.07$ [120]). Using eqn. 3.2 we get $\dot{q}_{\text{rad max}} = 400$ mW. This is a factor of four times higher than the amount of total heat load needed to lower the cold head temperature to 4 K (figure 3.2). If the outer can is maintained at 40 K, $\dot{q}_{\text{rad}}$ will drop down to 0.1 μW. This confirms that radiation shields at 40 K stage reduces the head load dramatically.

Radiation shields: Metals with highly reflective surfaces have very low emissivities. Emissivities can be reduced to 0.01 by polishing these surfaces. Metals such as Ag, Cu, Au, and Al are excellent candidates for radiation shields. Oxygen-Free High Conductivity (OFHC) Cu is the ideal choice in terms of thermal conductivity. However copper is prone to oxidation: oxidised copper has a high emissivity of 0.6. Therefore, gold plated OFHC copper is used for radiation shields. Recalculating the radiative heat load with radiation shields, $\dot{q}_{\text{rad shield}}$ remains lower than 0.1 μW. To reduce the load of blackbody radiation on the SNSPD devices a 4 K shield is employed. An Au-coated OFHC Cu cap is used to hold a fibre ferrule to couple photons to the detector as in figure 3.7. This ferrule holder shields the NbN nanowires from blackbody radiation emitted by the 40 K shield. It should be noted that the NbN nanowires do not need any magnetic shielding since the thickness of the NbN nanowire (4 nm) is much smaller than NbN's magnetic penetration depth ($\lambda_{\text{L}}^{\text{NbN}}$=176 nm [60]).

Pressure contacts: Unfortunately at cryogenic temperatures, the thermal conductivity at the boundaries across any two metal contacts is poor. This will affect contacts between (i) radiation shield and 40 K stage, (ii) the electrical cables and the heat sinking 40 K stage and (iii) more importantly, sample mount and 4 K stage. However, this heat flux across surfaces improves linearly with pressure irrespective of the contact area. Again, highly polished and conducting surfaces are a better choice for pressure contacts. This is the reason why Au plated OFHC Cu is chosen for the sample mounts and radiation shields. Since the contact area is not a concern for pressure contacts, bolting is an ideal choice for building a flexible system. Au-Au interface under a force of 500 N will have high thermal conductivity ($\sim$1 W/K). M4 size screws can provide force equal to $\sim$2.5 kN. By choosing a brass screw, which contracts more than the copper, pressure is increased with cooling from

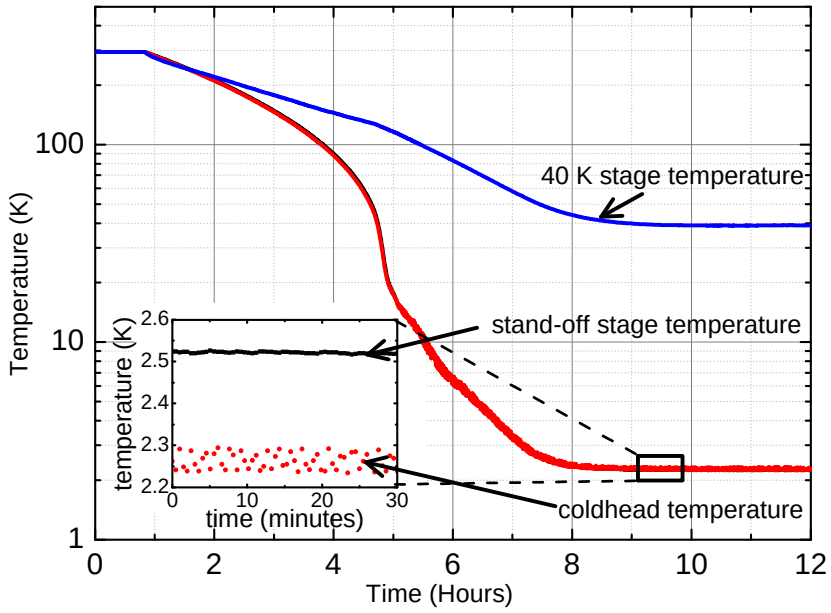

Figure 3.3: The cooldown plot of the cryostat with two mounted SNSPD devices. The coldhead reaches base temperatures of ∼2.3 K and 39 K in 9 hours. The inset shows the temperature oscillations in the coldhead and the elevated stable temperature of the stand-off stage.

room temperature to cryogenic temperatures. This has restricted our usage to ≥M4 brass screws and Au plated OFHC copper blocks for sample mounts and radiation shields.

Vacuum space: All the heat load calculations discussed above have assumed a vacuum space between the stainless steel can, radiation shields and sample holders. The cryostat should attain a sufficiently low pressure, such that the heat load is negligible due to the remaining gas in the chamber. A significant amount of time was spent on identifying and fixing leaks, using a He leak checker, during the initial building stage of the cryostat. This iterative process involve identifying and fixing smaller and smaller leaks. The space is evacuated to $< 10^{-5}$ mbar and sealed off before starting the cool down. The vacuum system uses commercially available room-temperature rubber O-ring seals for the flanges. 50 Ω hermetic SMA connectors and 12 pin hermetically sealed receptacle are used for electrical connections to the detectors and thermometers respectively. Optical connections consist of a home-made epoxied optical fibre feedthroughs. Once the cold stage reaches

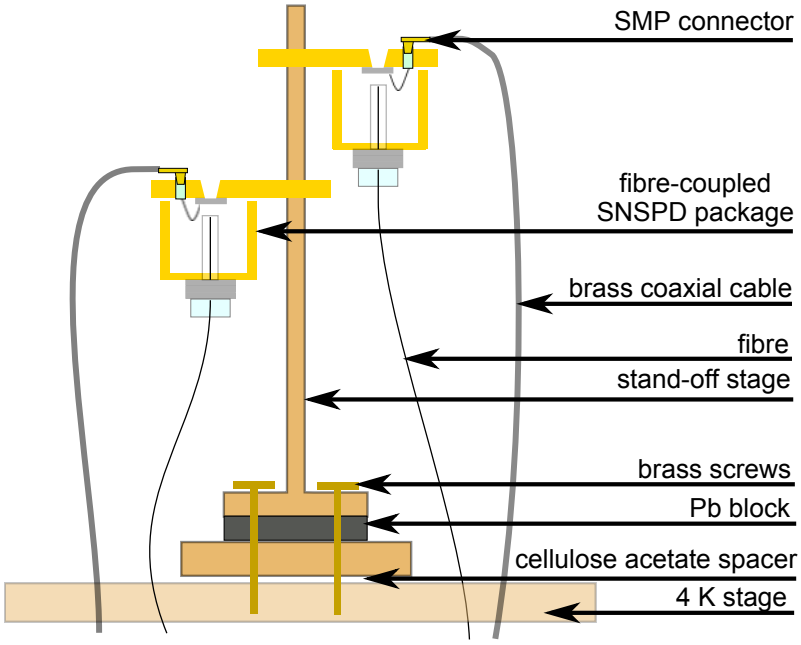

Figure 3.4: Schematic diagram of the stand-off stage with two fibre-coupled SNSPD packages mounted. A photograph of the stand-off stage is shown in figure 3.5

cryogenic temperatures, cryopumping dominates and condensible gases stick to cold surfaces. This will maintain the low pressure needed for a long period of time, even in the presence of a very small leak. This can be a serious hazard if overlooked. In the presence of a small leak, when the cold head warms back to room temperature, the condensed gases can evaporate and over pressure the cryostat chamber leading to a possibility of explosion. A pressure release vent is mandatory in this scenario. In our case, once the cooling is started, the main seal clamp is released as a safety measure.

With the design discussed above we have been able to reach close to the bottom-left point of the load map in figure 3.2. Cool down data, obtained with two sample mounts, one thermometer mounted at the 40 K stage and two thermometers mounted at the 4 K stage, is presented in figure 3.3. The cool down takes around 8 – 9 hours to reach the base temperatures ∼39 K and ∼2.3 K (figure 3.3). The second stage oscillates in between 2.26 K and 2.3 K, due to the cyclic operation of the GM cooler (red data points in the inset of figure 3.3). For temperature stability, a passive stand-off stage with a long thermal time constant (determined by the ratio of the

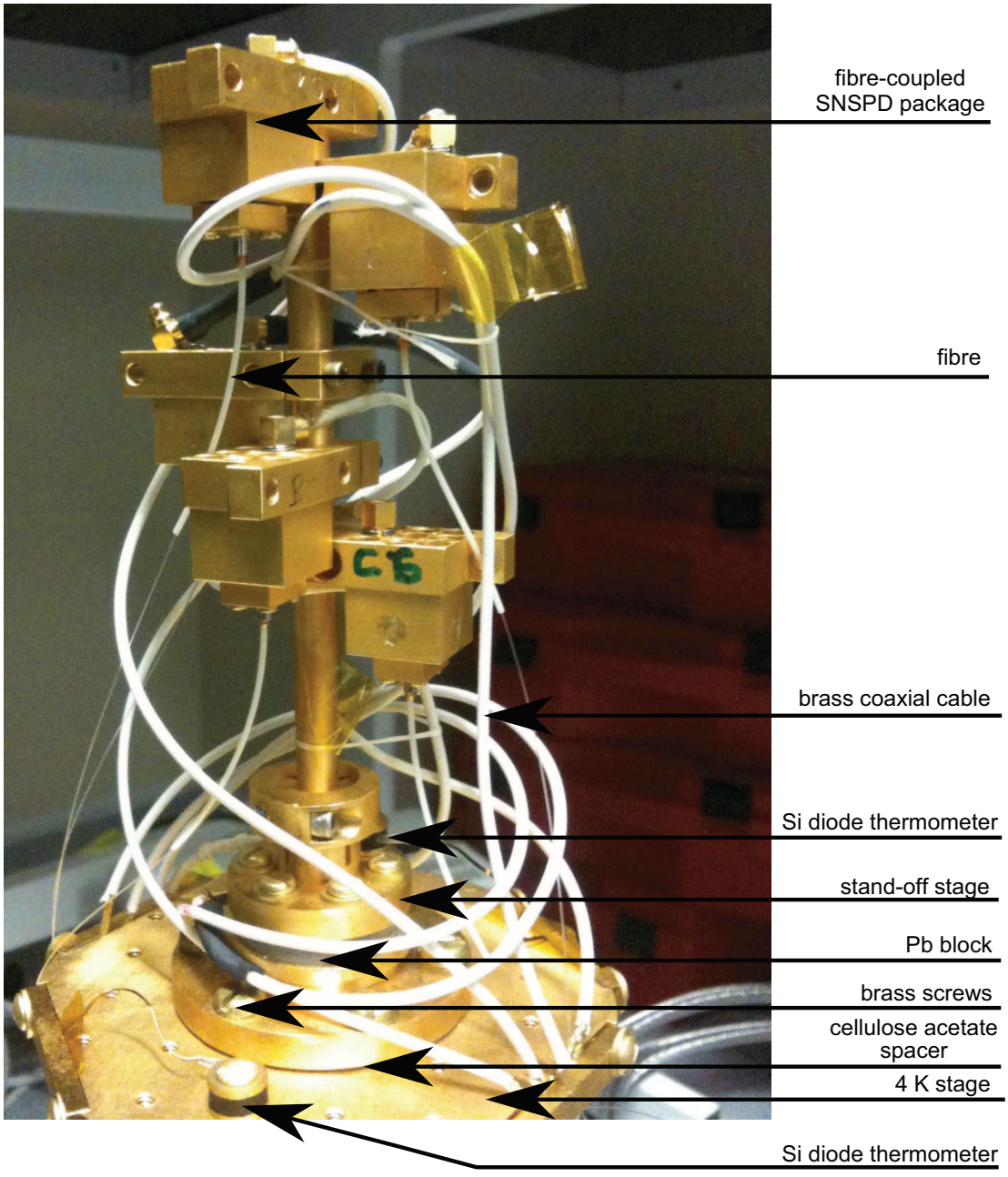

Figure 3.5: Photograph of stand-off stage with five fibre-coupled SNSPDs mounted.

heat capacity C to thermal conductance g) is implemented by sandwiching a 18.8 g lead (Pb) block in between the cold head and stand-off stage (figure 3.4). Pb has a superconducting transition at 7.19 K. Since Pb is maintained below its transition temperature, it becomes a poor thermal conductor and also contributes additional heat capacity. The Pb block along with cellulose acetate foil (OHP transparency sheet) acts as a spacer between the coldhead and the stand-off stage. The brass screws provide the necessary thermal conduction path between the stand-off stage and the coldhead. This arrangement reduced temperature variations at the stand-off stage (black curve points in the inset of figure 3.3). A picture of the stand-off stage is shown in figure 3.5.

3.2 Optical Challenges: Optimising Coupling Efficiency[1].

The most obvious way to couple photons to a detector inside a cryostat is via an optical window. This technique has the following disadvantages: (i) it is difficult to focus the optical spot on the 10 μm $\times$ 10 μm or 20 μm $\times$ 20 μm nanowire meander area, (ii) the vibrations in the refrigerator and ambient temperature fluctuations outside the cryostat result in poor alignment stability, (iii) operating multiple SNSPDs in parallel will require separate alignment optics, this will eventually limit the number of simultaneous operating detectors and (iv) the dark count rate will be higher due to the increase in blackbody radiation and stray light coupling to the device. To overcome these issues we have opted to guide the photons through an optical fibre, thereby eliminating the need for optical window in the cryostat. This option makes the operating environment more favourable for low noise SNSPD operation due to reduction in blackbody radiation and stray light reaching the detector. As in any other optical setup, good alignment is mandatory for fibre-coupled meander nanowire devices.

In the lab, the SNSPD chip is mounted on a sample holder and wire bonded for electrical connection as shown in figure 3.6. A hollow copper cap is used to hold the fibre-ferrule perpendicular to the surface of the chip as shown in figure 3.7. The

[1]This work was carried out together with Martin M. Härtig, MPhys. 2007/08

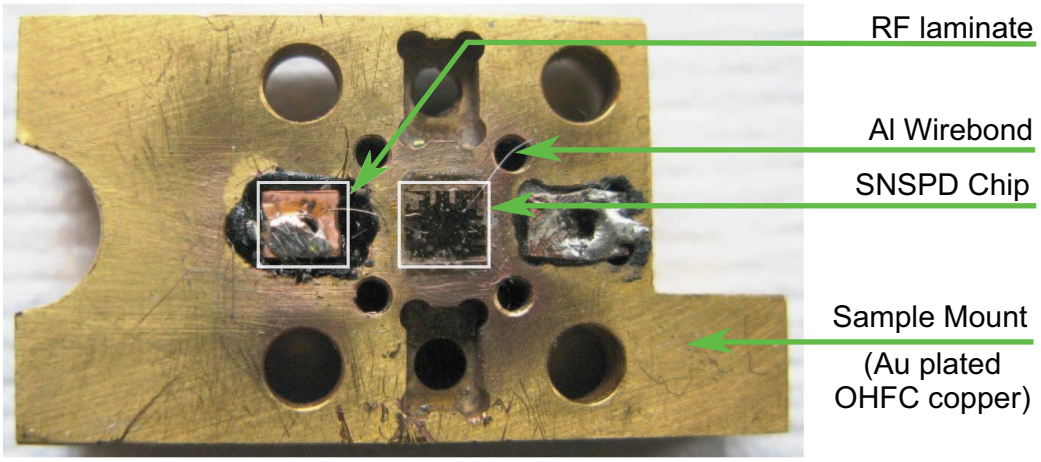

Figure 3.6: Photograph of the sample mount for SNSPD.

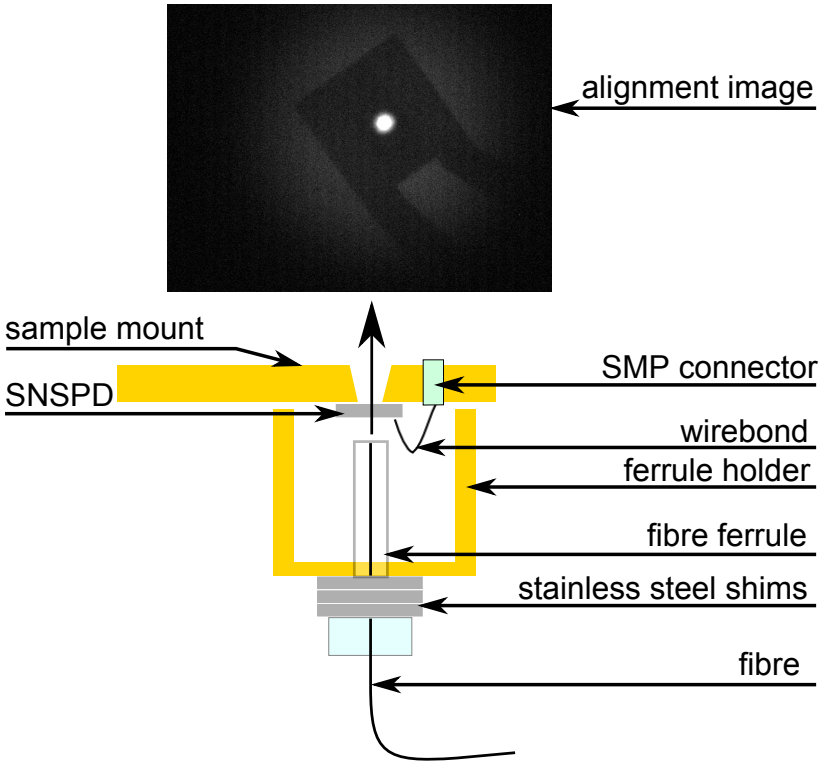

Figure 3.7: Schematic of the fibre-coupled SNSPD package (bottom) with aligned device viewed through microscope (top).

cap is fixed to the sample mount using brass screws. The challenge lies in optically aligning the device at room temperature and subsequently cooling the package down to ∼3 K without affecting the alignment. It is important that two factors (i) the separation between the fibre ferrule and SNSPD (z axis) and (ii) the alignment (x-y axis), are precisely controlled and maintained over repeated thermal cycles in order to avoid the need for realignment after every thermal cycle.

3.2.1 Analysing dependence of coupling efficiency on alignment

The primary goal of this thesis was to build a fibre-coupled, single-photon detector system operating in the telecom-wavelength window. The choice of fibres is restricted to single-mode fibres, as multi-mode fibres are prey to modal dispersion. Within the operating wavelength range photons are guided only in TEM_{00} mode within a single mode optical fibre. Commercially available 9 micron core (Corning SMF28 [14] or similar) fibre is the natural choice to couple photons to the detectors. When the photons leave the optical fibre they diverge. This beam divergence is studied below to understand where the fibre has to be positioned relative to the detector's active area to achieve high coupling efficiency(η_{coup}).

A Gaussian beam is a very close approximation to the output of a single mode fibre. The beam is considered as a perfect plane wave with Gaussian transverse irradiance (intensity) profile. Light waves spread transversely under diffraction laws. This causes the irradiance profile to evolve as the beam propagates along the optical axis (z axis). This evolution is understood by the waist width ($w(z)$) parameter. The intensity profile is given as

$$I(r,z) = I_0 \left(\frac{w_0}{w(z)}\right)^2 e^{-\frac{2r^2}{w^2(z)}} \tag{3.3}$$

where r is the distance perpendicular to the optical axis. The beam width is given as

$$w(z) = w_0\sqrt{1+\left(\frac{z}{z_0}\right)^2},\ z_0 = \frac{\pi w_0^2}{\lambda} \tag{3.4}$$

waist width (w_0) is the beam diameter at Rayleigh length (z_0) (the value of z at 50%

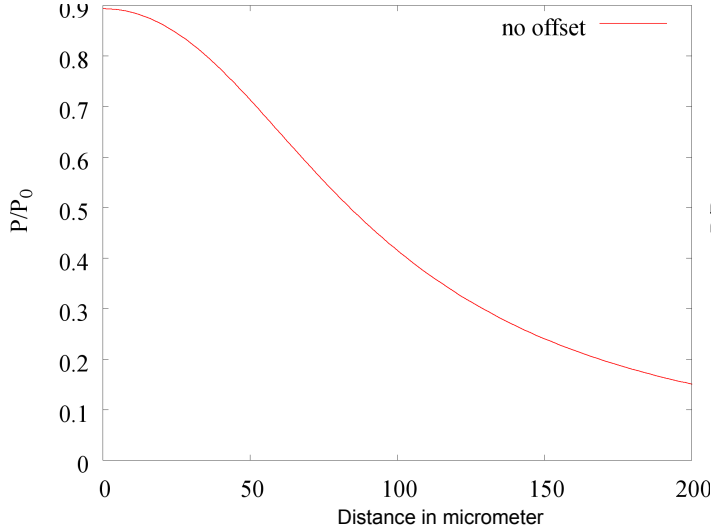

Figure 3.8: z alignment: calculated ratio of optical power coupled into 10 μm×10 μm SNSPD device from the end of a 9 μm core fibre plotted as a function of distance between the fibre end and the device for ideal x-y alignment. Graph reproduced from reference [121].

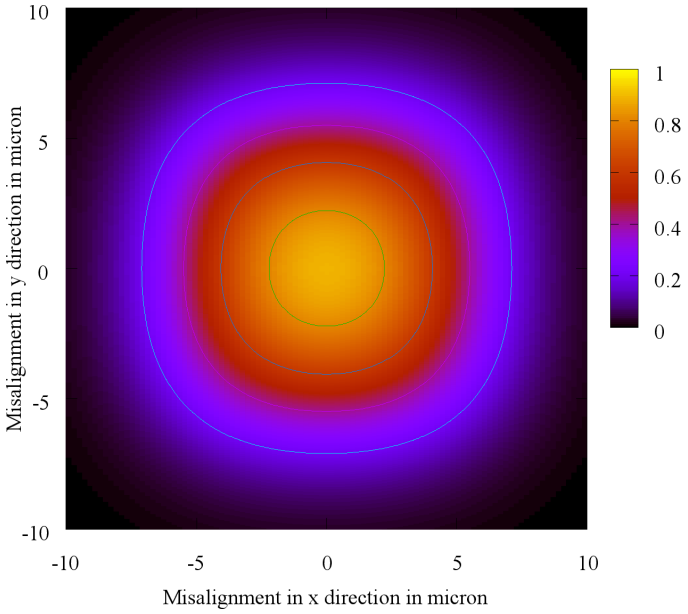

Figure 3.9: x-y alignment: calculated ratio of optical power coupled into 10 μm×10 μm SNSPD device from the end of a 9 μm core fibre plotted as a function of x-y misalignment between the fibre end and the device and the z axis distance was set as 10 μm. Graph reproduced from reference [121].

intensity). Using equations 3.3, 3.4, and assuming the active area of the SNSPD to be a square of width l, centred at $x = y = 0$, the coupling efficiency of power at SNSPD from the tip of fibre is given as:

$$\eta_{coup}(z) = \frac{1}{4}\left[erf\left(\frac{\sqrt{2}}{w(z)}x\right)\right]_{x=-l}^{l}\left[erf\left(\frac{\sqrt{2}}{w(z)}y\right)\right]_{y=-l}^{l} \tag{3.5}$$

Fibre coupling efficiency as a function of z and x-y misalignment is plotted for a 9 micron core fibre and 10×10 μm detector, at $\lambda = 1550$ nm in figure 3.8 and figure 3.9. The beam waist width and Rayleigh length has been taken as 5.2 ± 0.4 μm and $54.8^{+8.8}_{-8.1}$ μm respectively. The graphs indicate a 80% coupling efficiency, when the distance between chip and the device is less than 40 μm at a 2 μm alignment accuracy.

3.2.2 Optical Coherence Tomography for z-axis alignment

Optical Coherence Tomography (OCT) [122] is a low coherence interferometric technique. The key feature is that micrometre resolution can be achieved using a simple white light source. OCT is widely used in non-destructive imaging such as internal microstructures of biological samples [123] and defects in Si integrated circuits [124]. OCT can potentially be used to study and control the distance between fibre ferrule and the SNSPD surface. A basic OCT setup consists of a Michelson interferometer with broad spectrum light source. Low coherence light is launched through a fibre beam splitter to split light into 2 halves, one path ends at a mirror (reference arm) and the other half at the sample. The reflected returning light from both these arms will interfere. The interference pattern contains the path length difference information. The spectrometer at the receiver end is used to record a profile of the reflected signal intensity over the broad spectrum. The distance can be retrieved from the frequency of the interfered signal. This technique is known as frequency domain OCT. The limitation on the maximum spacing measurable is set by the spectral width of the light source and the minimum spacing is set by the resolution of the spectrometer.

Our experimental OCT setup is shown in figure 3.10. A polished fibre ferrule is used as the sample arm which combines the reference arm and the sample arm.

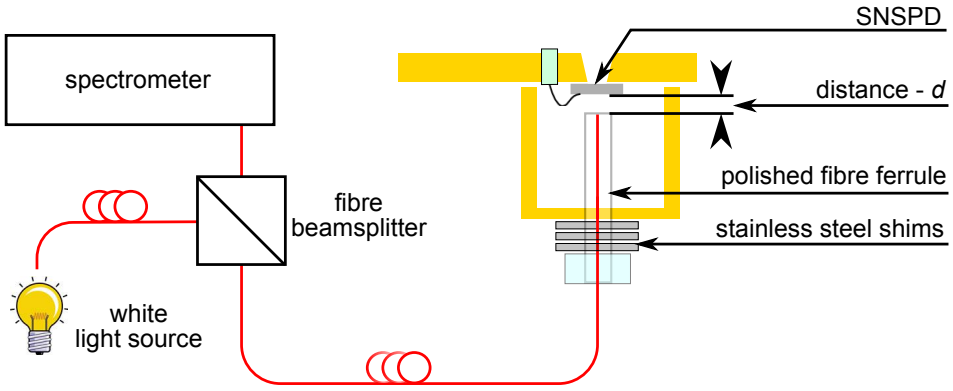

Figure 3.10: Schematic of the optical coherence tomography setup.

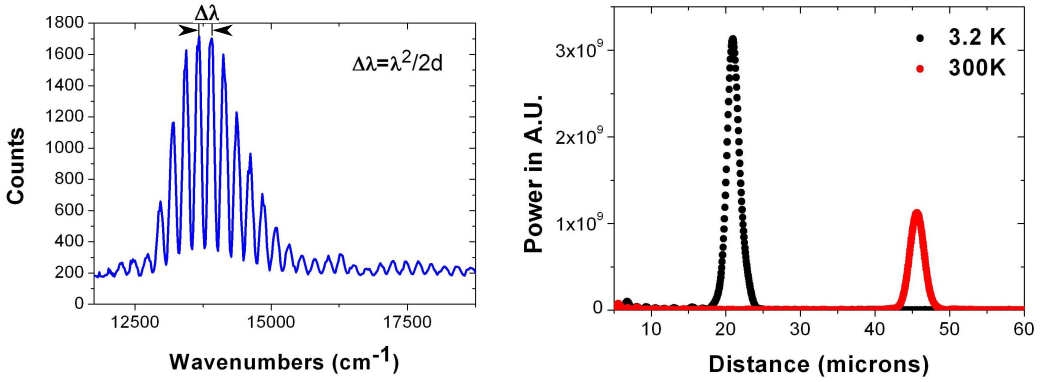

Figure 3.11: Optical coherence tomography data: (a) Interference pattern of the reflected light from SNSPD surface and the polished end of the fibre ferrule as seen by the spectrometer, (b) Fast Fourier transform of the interference pattern to extract distance 'd'. At 3.2 K, $d = 21\ \mu m$ and at 300 K, $d = 26\ \mu m$.

Light from a broad spectrum light source (halogen lamp) is launched through a fibre beamsplitter (50:50 splitting ratio at 700 nm) that splits it into two halves, one of which is dumped and the other half is coupled to the device using a polished ferrule. A fraction (∼4%) of the light is reflected back from the polished end of the ferrule, ∼4% of the remaining light is reflected back from the device surface and the rest of the light gets transmitted through the device. This acts like two poor parallel mirrors at the end of the sample arm separated by distance 'd', resembling a Fabry − Pérot cavity. The two reflected signals interfere at the coupler and an OceanOptics RedTide USB650 spectrometer is used to study the interference intensity profile over the broad spectrum (350–1000 nm). Path length of the cavity is equated to the integral multiple of the wavelength to retrieve the separation 'd' (due to interference) using the equation 3.6

$$\Delta\lambda = \frac{\lambda^2}{2d} \tag{3.6}$$

While packaging the device and the ferrule, precisely machined shims are introduced to control 'd'. Interference intensity profile obtained using the spectrometer is shown in figure 3.11(a) and its fast Fourier transformed signal is plotted in red in figure 3.11(b). At room temperature 'd' is typically set to ∼ 50 μm and as the package is cooled down to ∼3 K the package contracts reducing 'd' to ∼ 25 μm (black plot in figure 3.11(b)).

3.2.3 Near-infrared microscope for x-y axis alignment

In order to achieve accurate x-y alignment a NIR microscope is built with 50X magnification. The NIR microscope consists of (i) 50X Mitutoyo Plan Apo NIR objective, Qioptiq Optem NIR zoom 70XL optical System and phosphor coated NIR CCD camera (see figure 3.12). For ∼2 μm accuracy alignment, the sample holder and the ferrule holder are secured onto a platform and a sub-micron x-y alignment stage respectively. A 1550nm beam from a CW laser diode is sent through the fibre ferrule, the beam emanating from the ferrule is transmitted through the device and is viewed using the long working distance objective. Acceptable x-y alignment is achieved by carefully adjusting the position of the 1550 nm spot relative to the SNSPD device

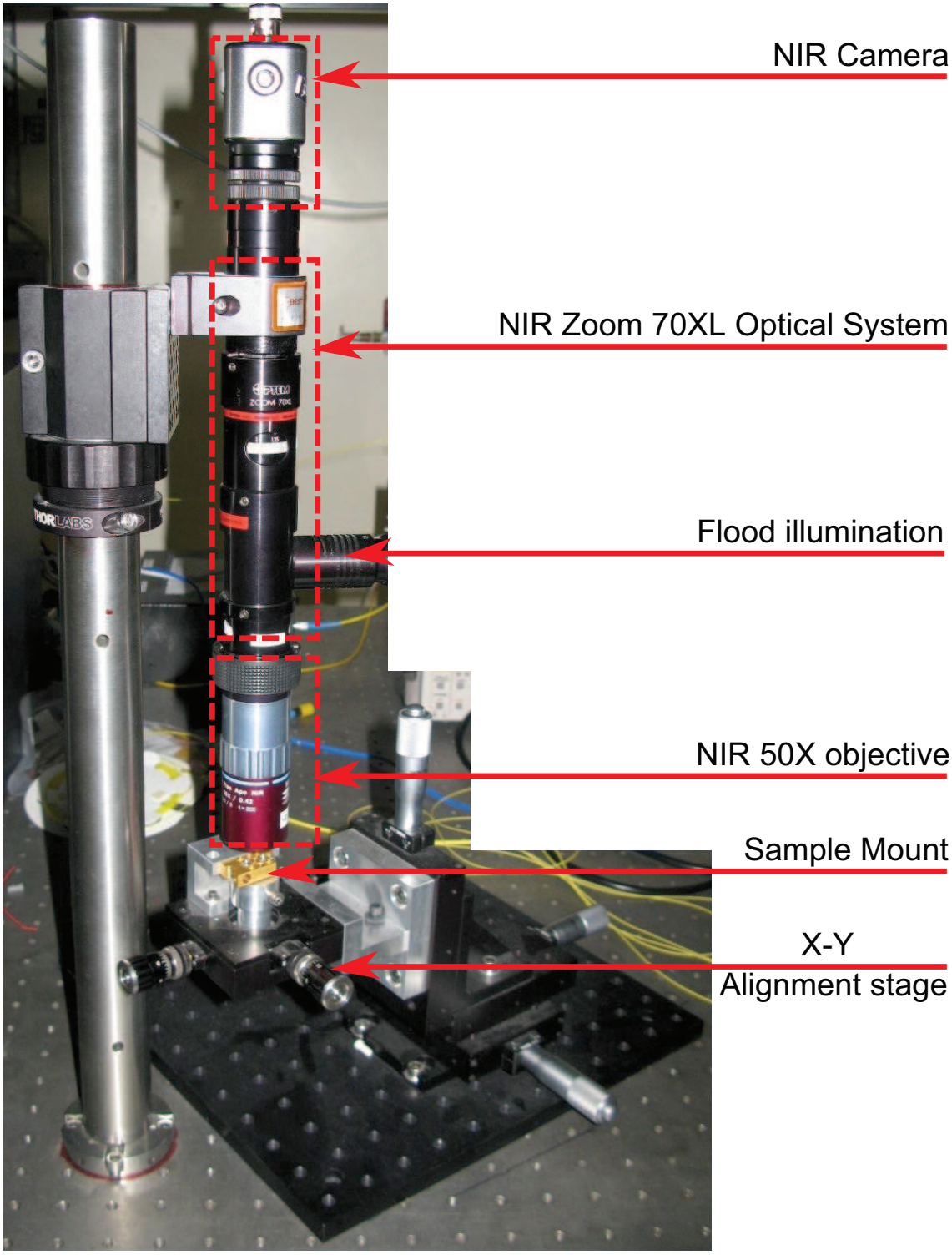

Figure 3.12: Schematic of the x-y alignment setup.

area within the 50 Ω coplanar waveguide structure (figure 3.7). Thereafter the ferrule holder and sample holder are bolted together using brass screws. The alignment is performed at room temperature and the package is attached to the stand-off stage in the cryostat (see figure 3.5). This robust packaging scheme enables the alignment to be preserved over repetitive thermal cycling between room temperature and cryogenic temperatures.

3.3 Electrical Challenges: Bias and Read-out Electronics

The key advantages of SNSPD over other telecom wavelength photon-counting technologies are its negligible dark count rate (D), <100 ps timing jitter and ungated operation. The dark count rate depends on the bias current of the SNSPD and the signal-to-noise ratio of the read-out circuit. The timing resolution depends on the bandwidth and jitter of the electronics. Therefore, suitable bias and read-out electronics are needed to optimise the performance of the SNSPD. This section discusses the method to determine appropriate bias points for an SNSPD, followed by the simulation of the output pulse from an equivalent electrical circuit. Based on this simulation and measured output, the choice of read-out electronics used is justified.

3.3.1 Studying I-V characteristics

For an SNSPD to be single-photon sensitive it has to be stably biased just below its critical current. The critical current can be determined by studying the I-V characteristics of the nanowire. The device is characterised by using the electrical circuit shown in figure 3.13. This measurement is carried out with a 50 Ω shunt across the nanowire. The shunt resistor prevents the biased device from latching i.e. remaining in the resistive state without recovery. The voltage is swept across ±5 VDC, in steps of 1 mV, using an isolated voltage source (SRS SIM928 module) and the corresponding potential difference across the SNSPD is measured using a digital voltmeter (SRS SIM970 module). Both the SRS modules were installed in a single SRS SIM900 mainframe. Measured I-V data, at ∼2.3 K, is plotted in

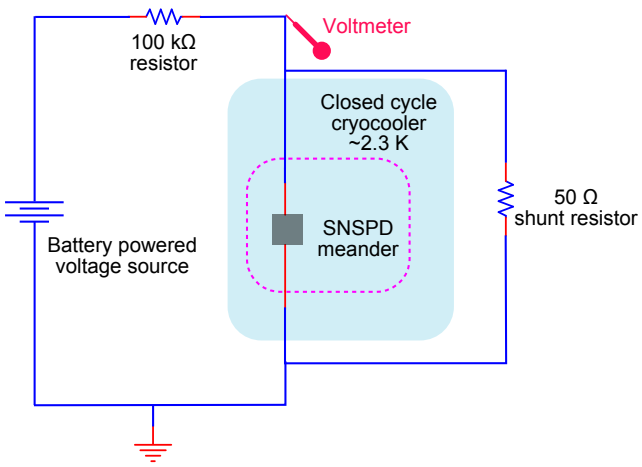

Figure 3.13: Schematic of an electrical circuit to study I-V characteristics of an SNSPD. The SNSPD is current biased with the help of battery powered voltage source in series with a 100 kΩ resistor and the potential drop across the parallel network (nanowire and 50 Ω shunt) is measured.

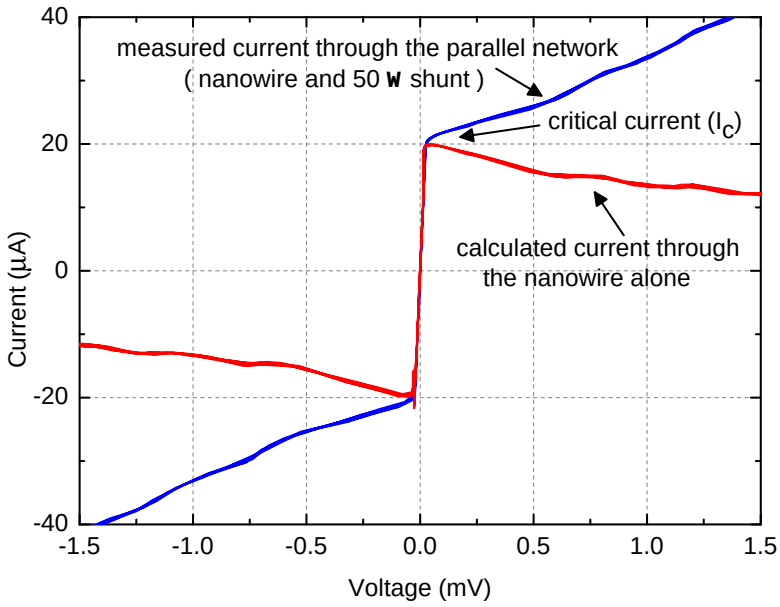

Figure 3.14: I-V characteristics of an SNSPD measured at ∼2.3 K with a 50 Ω shunt resistor and the data is corrected by subtracting the current flowing through the 50 Ω shunt resistor.

blue in figure 3.14. The red plot in figure 3.14 shows the plot of the corrected I-V characteristics of the SNSPD by calculating the current flowing only through the SNSPD by subtracting the current flowing through the 50 Ω shunt resistor. This sample loses its superconducting property for a current higher than ∼20 μA. This SNSPD has to be biased just below ∼20 μA to operate as a single-photon detector at ∼2.3 K. A resistance of 1.5 Ω is observed at the superconducting state, this is due to the finite resistance of the cables used to study the detector in a 2-wire measurement.

3.3.2 Electrical model of SNSPD

When a current-biased superconducting nanowire absorbs a photon, a region with a large number of low energy quasi particles is created; this is referred to as the 'hotspot' [17]. To maintain the same bias current the surviving Cooper pairs accelerate. For this acceleration to happen an electric field is generated intrinsically which is observed as an output voltage pulse. The temporal information of the voltage pulse depends entirely on the thermodynamics of the subsystems, such as Cooper pairs, quasiparticles and phonons in the superconductor and its substrate [125]. This non-equilibrium state can be electrically approximated to the circuit shown in figure 2.8(a) [63, 64]. The absorption of photon is considered as the opening of the switch resulting in an instantaneous increase in resistance of the nanowire. The current in the inductor decays with a time constant $L_k/(50 + R_n)$ towards a steady final current $I_{bias} \times 50(50 + R_n)$. The drop in current also decreases the Joule heating $I(t)^2 R_n$ in the hotspot region. Therefore the superconducting current recovers before the final current is reached.

More detailed practical circuit has been simulated using Cadence PSpice software package (Figure 3.15). The SNSPD consists of the kinetic inductor ($L1$) and the hotspot resistance ($R1$). The transmission line represents the 50 Ω coaxial cable used to read the output pulse. The nanowire is current biased ($I1$) through the inductive arm ($L2$) of the Bias Tee and the output RF pulse is coupled through the capacitive arm ($C2$). The output pulse observable across the load resistor ($R3$) is shown in figure 3.16. A single-photon absorption event is simulated by introducing the $R1$ into the circuit with the help of a current controlled switch ($W1$). The switch

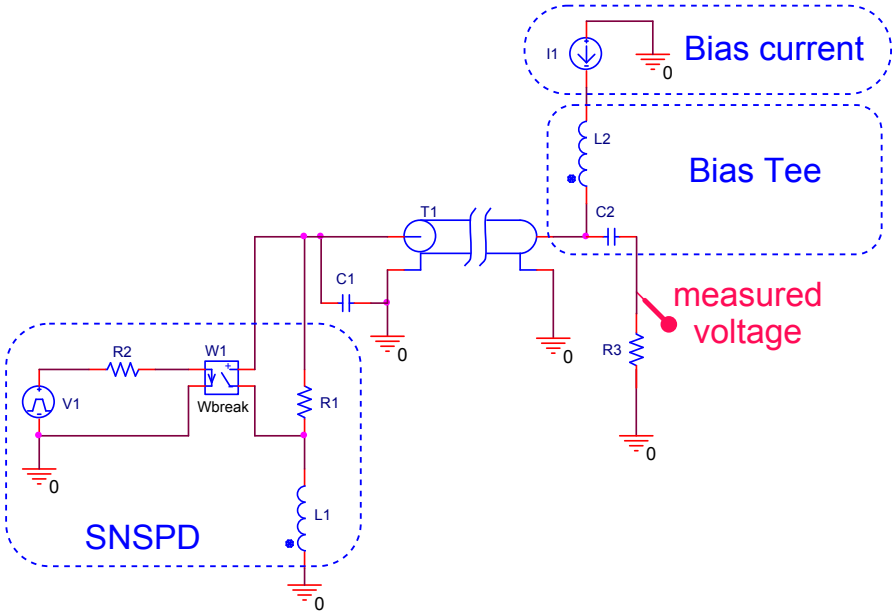

Figure 3.15: Schematic of the PSpice model of the SNSPD circuit: The SNSPD is simulated using kinetic inductor $L1$ and 'hotspot' resistor $R1$, The formation and collapse of the 'hotspot' is simulated using current controlled switch $W1$. The transmission line $T1$ is used for the 50 Ω coaxial cable. $L2$ and $C2$ represent the Bias-Tee. The SNSPD is current-biased using current source $I1$. The potential difference across the load resistor $R3$ is measured using a voltage measurement probe.

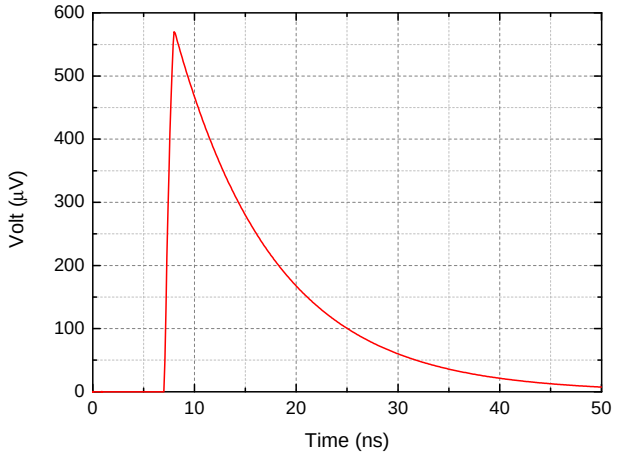

Figure 3.16: The output pulse of the SNSPD is simulated using the circuit shown in figure 3.15 for the following values: $L1 = 500$ nH, $R1 = 500$ Ω, $I1 = 20$ μA and $R3 = 50$ Ω. The values of $L1$ and $R1$ were chosen based on reference [64]. Switch $W1$ is opened at $t = 0$ and closed when $t = L_k/(50 + R_n)$. The output reaches the voltmeter only when $t = 7$ ns due to the delay in the transmission line.

is opened by a leading edge from the voltage source ($V1$) and the switch is closed by the trailing edge from the voltage source ($V1$). The time delay between the opening and closing of the switch is estimated as the time constant defined by the values $L1$ and $R1$. A careful section of electronics is needed to use this weak RF pulse in TCSPC experiments.

3.3.3 Operation of the SNSPD read-out circuit

The magnitude of an unamplified voltage pulse from an SNSPD is bias current times the shunt resistor value ($V_{pulse} = 50\ \Omega \times I_{bias}\ \mu A$). Typical critical current of a 20 μm $\times$ 20 μm NbN SNSPD is around 20 μA which restricts the pulse height to less than 1 mV (Figure 3.16). ($V_{pulse} = 50\ \Omega \times 20\ \mu A = 1$ mV). This pulse needs to be amplified to trigger commercial counters, discriminators or photon-counting cards. Typically TCSPC cards require 80 mV for triggering. In our case this weak pulse exiting the cryostat is amplified using room-temperature Low Noise Amplifiers (LNAs). For several reasons, the room-temperature LNAs have been used instead of cryogenic amplifiers. Cryogenic amplifiers are expensive and need one each for every detector channel and also would add an additional heat load in the cryostat. Moreover cryogenic amplifiers are not typically 50 Ω impedance matched causing undesirable reflections. Placing the LNAs as close as possible to the SNSPD is crucial for better signal to noise ratio (SNR). The signal from SNSPD is coupled to the LNA through the AC port of a bias tee, while the DC port is used to bias the device. The sharp leading edge of the voltage pulse contains the temporal information of the photon absorption. If the bandwidth is too low the amplifiers can flatten the sharp leading edge. On the other hand a wide bandwidth amplifier can increase the noise due to back action. A low frequency cut-off will lead to oscillations in the slow falling edge of the pulse giving ringing and potentially leading to retriggering of the counter. This afterpulsing effect could result in an elevated count rate on the SNSPD. The SNSPD along with readout electronics has been simulated as in figure 3.17.

Characteristic leading edge of the SNSPD pulse has a time scale of $\sim$1 ns ($L_k/(50 + R_n)$), this corresponds to a frequency of 250 MHz. RFBay LNA-580 has a upper cut-off frequency at 580 MHz giving a reasonable match. This 10–

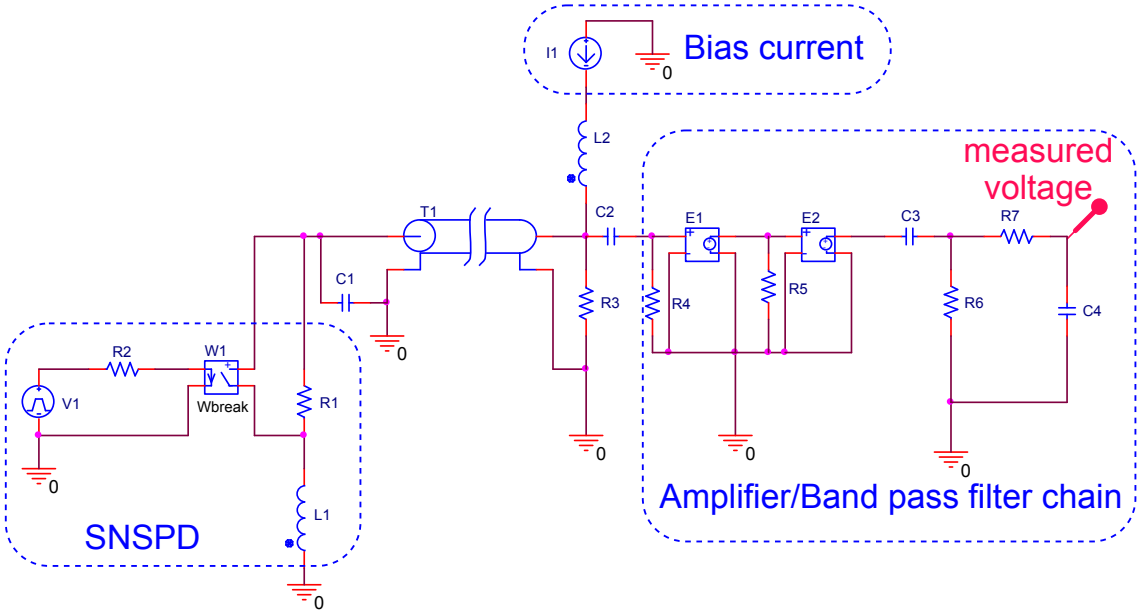

Figure 3.17: SNSPD circuit with amplifier chain ($E1$ and $E2$)and bandpass filter ($C3-R6$ and $R7-C4$ circuit)(10 – 580 MHz). The SNSPD is shunted with a 50 Ω resistor ($R3$).

580 MHz band pass amplifier does not degrade the pulse shape. This is verified from the simulation (figure 3.18(a)). The red curve (labelled – before filter) is the raw response of the nanowire. The leading edge has a time-scale of 1 ns and the trailing edge has a time scale of ∼20 ns ($L_k/(50)$). The black curve is the output pulse after the amplification stage i.e. bandpass filter in the case of our simulation. The trailing edge is different for both the curves due to the lower cut-off limit (10 MHz) set by the amplifiers. A second stage of amplification (RFBay LNA1000 with cut-off frequency at 1 GHz) is added to the circuit to boost the voltage up to a few 100 mV.

A measured output pulse along with a simulated pulse is plotted in figure 3.18(b). The measured signal is negative due to inverting LNA used. The voltage drop starts at 5 ns due to the delay in the coaxial transmission line in the circuit. 2300 nH and 2.9 KΩ has been used for L_k and R_n respectively in the simulation to match the leading edge (∼1 ns) and trailing edge (∼20 ns) of the output pulse. The bump in the trailing edge at ∼15 ns is due to the reflection bouncing back and forth between SNSPD and the bias tee, with a period of ∼10 ns. This reflection is due to the

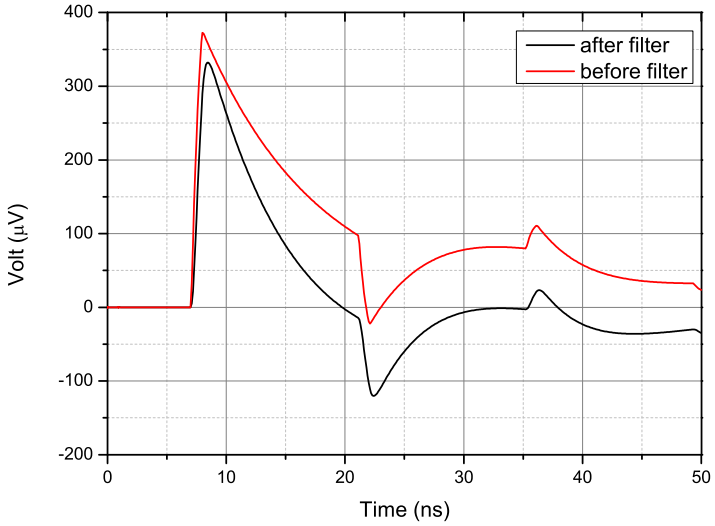

(a) Pulse Shape

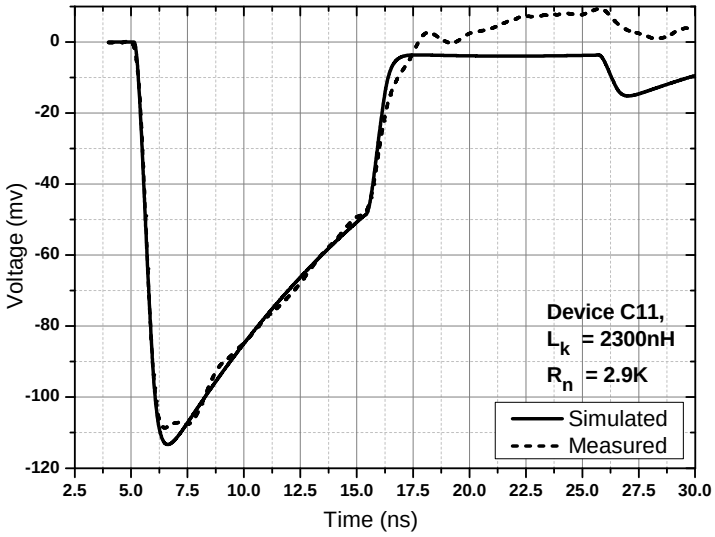

(b) Measured Vs Simulated

Figure 3.18: Simulation results of practical SNSPD circuit: (a) raw output pulse of the SNSPD simulated before and after the unit gain amplifier chain and band pass filter. The fluctuations in the trailing edge of the output pulse are due to the poor impedance matching due to addition of the 50 Ω DC shunt. (b) Simulated result fitting the measured output pulse from a 20 μm × 20 μm NbN SNSPD. The simulated pulse has been inverted due to the inverting amplifier used in the experiment.

impedance mismatch due to the 50Ω DC shunt resistor (mounted via a tee piece). The remarkable overlap between the simulated and measured voltage indicates that the read-out circuit has not suppressed any significant information.

The 50Ω DC shunt resistor plays a major practical role in operating the device in a free running mode. In the absence of the shunt resistor, the SNSPD is susceptable to latching to a resistive state disrupting the continuous operation of the device. When the hotspot is collapsing and the return current is growing back to its stable state, a balance can be achieved between Joule heating and the energy dissipated by the hotspot into the substrate. This balance leads to a stable self heating hotspot. The presence of a self-sustaining hotspot does not allow the SNSPD to recover its superconducting state, making it insensitive to photons. This phenomenon is known as "latching" [70]. Latching can be averted by quenching the hotspot quickly by diverting the bias current through the 50Ω DC Shunt resistor, before the return current starts to flow through SNSPD. Without a 50 Ω shunt resistor, the SNSPD would need to be monitored (via the DC voltage) throughout an experiment, and manually reset by cycling the bias current.

3.4 Measurement Challenges: Characterisation of the Detector System

3.4.1 Evaluation of the system detection efficiency

System detection efficiency (η_{sde}) of the detector is determined by calculating the ratio of the number of photons detected to the number of photons coupled into the system. This ratio is estimated without backing out the losses within the system. Schematic of the setup used to determine η_{sde} at a given wavelength for a fibre coupled detector is shown in figure 3.19. A laser diode[1], gain switched by Agilent 81110A Pulse Pattern Generator (PPG), generates optical pulses at the drive frequency f (typically 1 MHz). The laser pulses are attenuated using two programmable digital optical attenuators (JDS Uniphase HA9). Each attenuator is calibrated over 60 dB

[1]Fibre-coupled laser diodes Hitachi HL8325G, Mitsubishi ML725B8F, Mitsubishi ML925B6F were used at 830 nm, 1310 nm and 1550 nm wavelengths respectively.

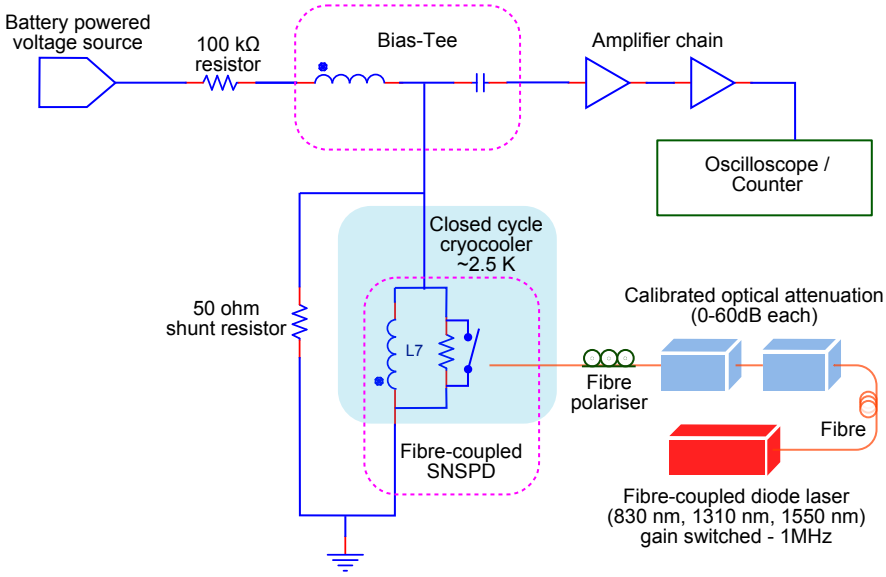

Figure 3.19: Schematic of the system detection efficiency measurement: weak coherent optical pulses are generated using a gain switched diode laser and the mean photon per pulse is varied using a series of calibrated optical attenuators. The polarisation of the optical pulse is rotated using a fibre polariser. The response from the SNSPDs is recorded using the standard read-out circuit explained earlier.

with a conventional power meter[1], resulting in a range of 0 – 120 dB attenuation when used in series. This scheme allows us to vary the photon flux fibre-coupled to the SNSPD. The device is current biased at constant bias point (I_{bias}) using an isolated voltage source (SRS SIM928) in series with a 100 kΩ resistor. The average number of photons per pulse (μ) is controlled by varying the attenuation and the corresponding response from the device is recorded, using Agilent 53132A frequency counter, as R counts per second. As indicated in figure 3.20, when the photon flux is extremely low ($\sim 10^{-4}$ photons/pulse), R corresponds to the dark count rate D of the device at I_{bias}. When the photon flux is high, the count rate R saturates at the frequency f as the photon flux reaches hundreds of photons/pulse regime. This is due to the inability of meander SNSPD to resolve the number of photons absorbed by the nanowire. For $(1/f) >$ detector recovery time($\sim$ 20 ns), η_{sde} is extracted by

[1]The calibration was performed using PM300 - dual-channel benchtop optical power meter with the following sensors: (i) Thorlabs S144A (InGaAs sensor) for wavelengths 1310 nm and 1550 nm and (ii) Thorlabs S120B (Si Sensor) for 830 nm wavelength. These optical sensor heads offer NIST-traceable measurements [126, 127].

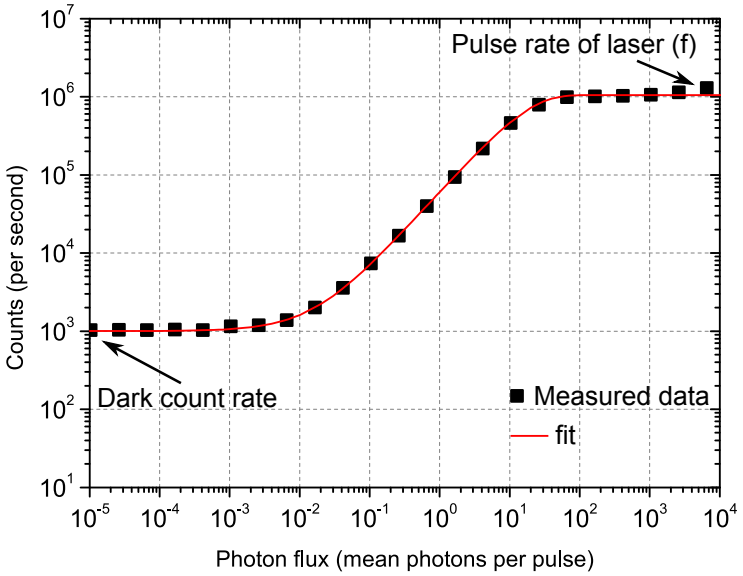

Figure 3.20: SNSPD photon detection rate is plotted against the photon flux for a 1 MHz gain-switched diode laser. The data was taken using a NICT NbN SNSPD maintained at 2.3 K. The counts measured when the photon flux is very low is primarily the dark counts from the SNSPD. The counts increase in proportion to the photon flux over the range 0.01 – 10 photons per pulse. The plateau at the top-right is due to the saturation of the SNSPD. Since this SNSPD acts as a binary device the counts saturate at 1 MHz (gain switching frequency).

fitting the data (figure 3.20) to the following curve [1, 21]:

$$R = D + f(1 - e^{-\eta\mu}) \tag{3.7}$$

The η_{sde} is measured at various bias points (I_{bias}) as shown in figure 3.21. η_{sde} is plotted against the dark count rate in figure 3.22. $\eta_{registering}$ increases as the bias current I_{bias} is increased[1]. The x-axis represents the increase in bias from left to right (increasing dark count rate). Raising I_{bias} increases η_{sde} by pushing $\eta_{registering}$ towards unity because even the smallest hotspot formed can drive the nanowire resistive due to increased current density and Joule heating in the region. The dark count rate also increases as I_{bias} approaches I_c. Since the increase in sensitivity forces the SNSPD to pick up electronic and thermal fluctuations resulting in higher dark count rate. The device is operated at an appropriate bias point depending

[1]Recall $\eta_{sde} = \eta_{coupling} \times \eta_{absorption} \times \eta_{wavelength} \times \eta_{registering}$.

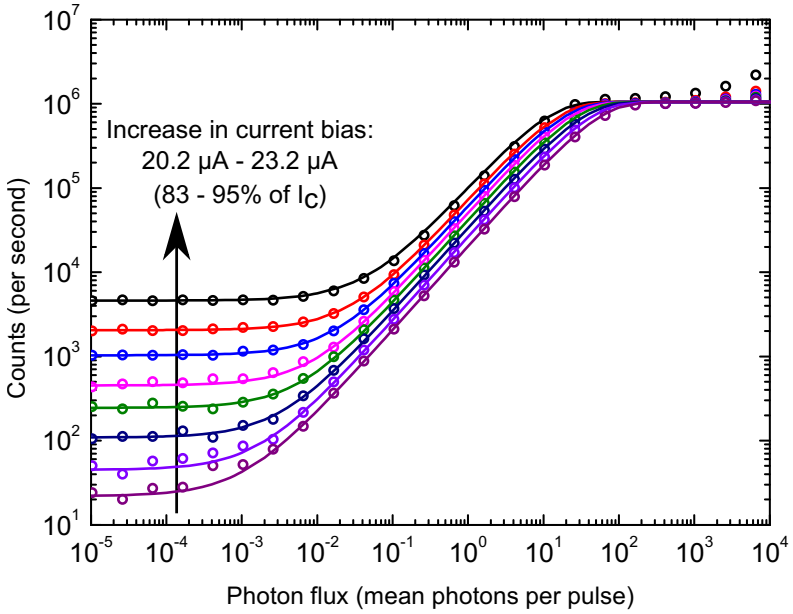

Figure 3.21: The relationship between the photon flux and measured count is plotted for various bias points. The bias current is swept from $0.83I_c$ to $0.95I_c$ in steps of 0.4 μA and at each bias point, the photon flux is varied and the corresponding SNSPD output counts is measured at 2.3 K. This measurement was performed at 1310 nm wavelength for a NICT NbN SNSPD device.

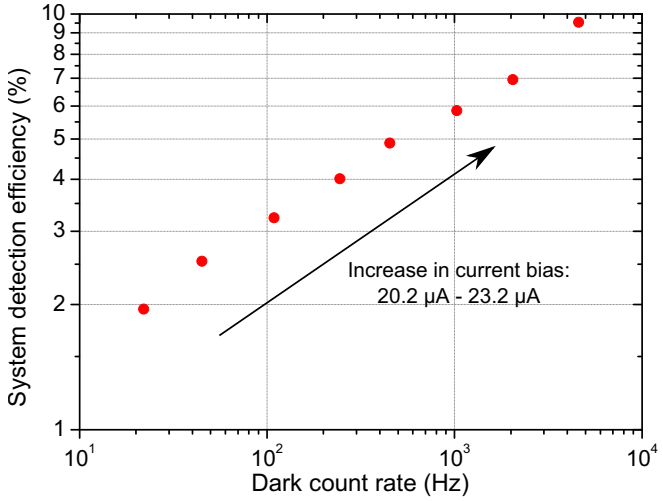

Figure 3.22: System detection efficiencies of a NICT NbN SNSPD device plotted against the dark count rate for 1310 nm photons at 2.3 K. The SNSPD sensitivity increases as the bias current is raised towards the critical current; dark count rate also increases simultaneously.

on the dark count rate and detection efficiency requirements of the experiment in question.

3.4.2 Effect of optical polarisation on detection efficiency

From an optical standpoint, the meander SNSPD device is essentially a subwavelength grating and is observed to possess noticeable polarisation sensitivity [30]. It has been reported that the count rate from the detector displays a maximum and a minimum value depending on the orientation of the electric field being either parallel or perpendicular to the orientation of the nanowire. This is because of the variation in $\eta_{absorption}$ exhibited by the meander structure [30]. In our setup, the polarisation dependence is observed by varying the polarisation of the incident photons using a fibre polariser (see figure 3.19). The fibre polarisers are adjusted to either high or low count rate and corresponding η is subsequently measured. The variation in system detection efficiencies is plotted in figure 3.23 for two polarisation states at λ=1550 nm. The experimental ratios of the high count rate η_{high} to that of low count rate η_{low} are in accordance with results from simulations (see figure 3.24)[1]. Comsol Multiphysics v3.2b (EM module) was used to calculate the absorptance for parallel and perpendicular polarisations. The SNSPD was modelled as a NbN infinite grating on a sapphire substrate with following parameters: NbN thickness - 4 nm, width - 100 nm, fill factor - 50%, $n_{NbN} = 5.23 - i5.82$ and $n_{Sapphire} = 1.75$ at 1550 nm, $n_{NbN} = 3.6 - i4.52$ and $n_{sapphire} = 1.75$ at 900 nm. More detailed information on the simulations can be found in reference [30, 128]. Attempts to mitigate the disadvantage of SNSPD being sensitive to polarisation have been demonstrated using spiral 2.9(f) [67] and perpendicular device designs 2.9(g) [67]. These designs suppress the SNSPD polarisation sensitivity; this inevitably reduces the absorption efficiency.

3.4.3 Measurement of timing resolution

Given that state-of-the-art optical sources (femtosecond lasers, SPDC sources) have negligible jitter, the timing jitter of the detector gives the practical limit on when

[1]The simulation results were kindly provided by Dr. Vikas Anant (MIT, USA).

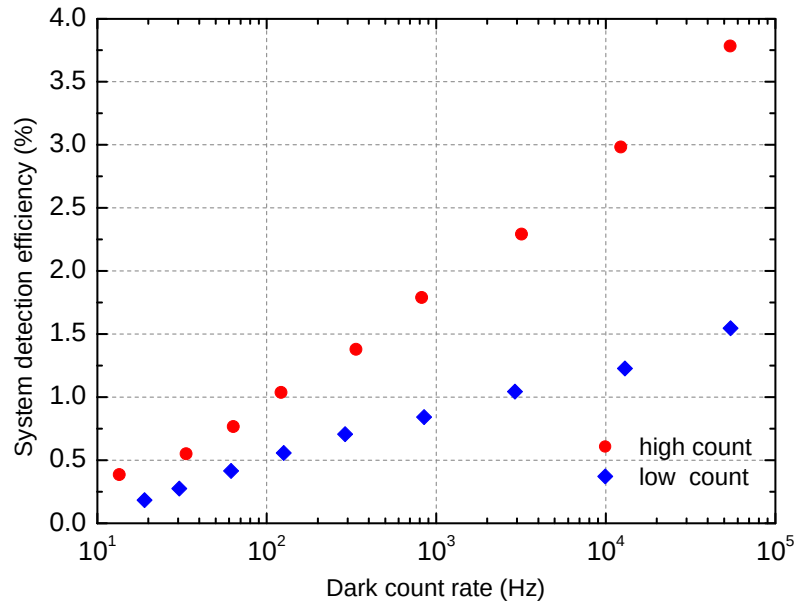

Figure 3.23: Maximum and minimum detection efficiency tuned via input polarisation at 1550 nm wavelength at various bias points. This data was measured using a NICT NbN SNSPD device maintained at 3.6 K.

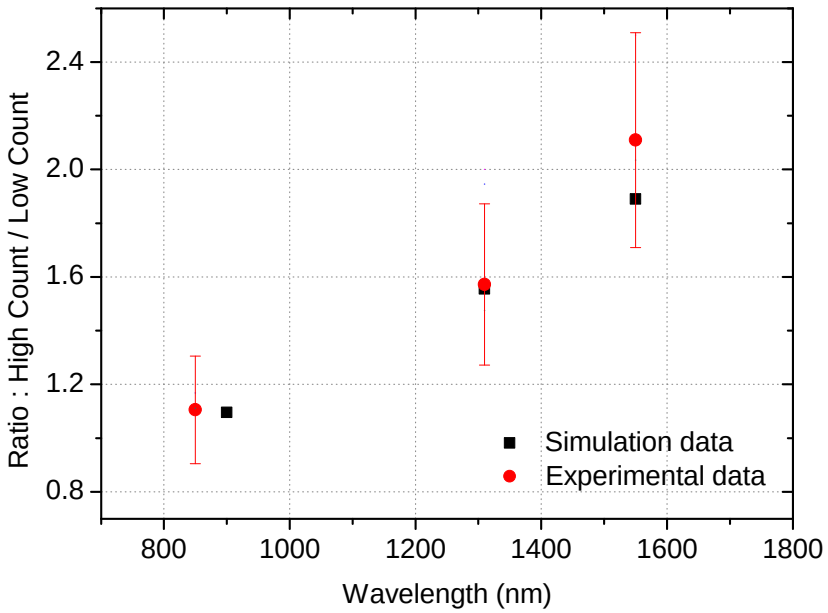

Figure 3.24: Polarisation dependent detection efficiency ratio at 830 nm, 1310 nm and 1550 nm wavelengths. This data was measured using a NICT NbN SNSPD device maintained at 3.6 K.

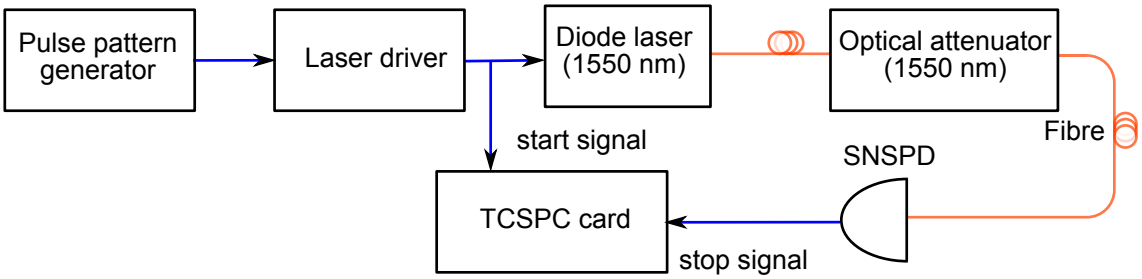

Figure 3.25: Timing jitter is measured using a Becker and Hickl TCSPC card. Weak coherent optical pulses are generated using a 1550 nm diode laser at 16 MHz using a pulse pattern generator. The timing electronics is started by the electrical pulse from the laser driver. The optical pulses are attenuated to single-photon regime using optical attenuators. The single-photons are detected by the SNSPD, which stops the TCSPC electronics. A histogram is generated by the TCSPC software module.

a photon arrival can be gated or timestamped. Jitter is usually given by the Full Width at Half Maximum (FWHM) of the histogram of the detection time of photons. The jitter analysis can be performed via the experimental setup shown in figure 3.25.

Photon pulses are generated by driving PicoQuant (LDH-P-1550) picosecond diode laser (λ=1550 nm) by a pulse pattern generator (Agilent 81133A Pulse Pattern Generator). The pulses are attenuated to the single-photon per pulse regime and coupled to the SNSPD. Synchronisation (Sync) pulses from the laser driver (PicoQuant PDL 800-B) and output pulses from the detector are used to start and stop the Time-Correlated Single-Photon Counting (TCSPC) card respectively. The TCSPC card generates a histogram of time intervals between start and stop signals. The two types of cards that were available to us were (i) Becker & Hickl SPC600 card and (ii) PicoQuant PicoHarp 300. A sample statistical plot of the instrument response is shown in figure 3.26. The histogram has a Gaussian profile and a FWHM of $\sim$60 ps. This data was recorded using Becker & Hickl SPC600 card tuned to a timing resolution of 4 ps time bins.

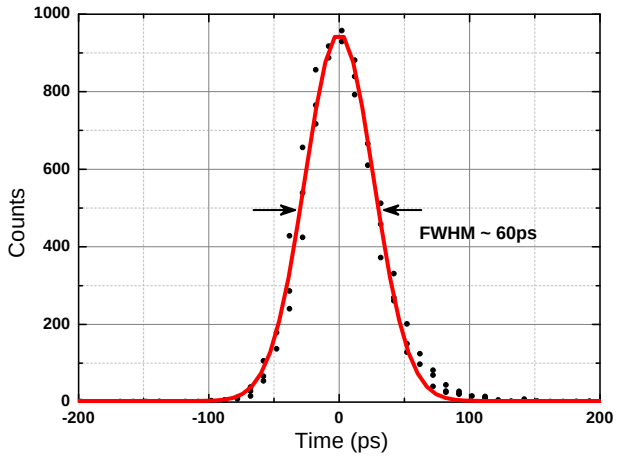

Figure 3.26: Jitter plot at 1550 nm using the setup described in figure 3.25. The timing bin resolution was set to 4 ps. The black dots are the measured counts at each time bin and the red curve is the Gaussian fit of the data. 60 ps FWHM jitter is obtained from the Gaussian fit.

Comparison of TCSPC cards : The working principle of Becker & Hickl (B & H) SPC600 card is schematically shown in figure 3.27. It has two independent Constant Fraction Discriminators (CFDs), one for reference signal and the other for the single-photon detector signal. The CFD electronics is designed to generate a voltage pulse when the input signal reaches a constant fraction of the leading pulse; irrespective of the pulse height. Schematic operation of CFD is shown in figure 3.28. The principle is to add an inverted and delayed version of the original signal to itself and extract the zero crossing (ZC) point. This ZC point establishes precisely when the signal reaches a constant fraction of height determined by the delay. The time difference between the generation of the two CFD output signals is converted into an analog signal using Time-to-Analog converter (TAC). This analog signal is amplified and digitalised for high precision histogramming. This mode of running is known as $start - stop$ mode. Since the efficiencies of single-photon detectors are poor, only a small fraction of detection events reach the TCSPC card compared to the reference signal. This makes the card overrun without reset, waiting for a detection event upon receiving every reference signal. To overcome this issue, B&H SPC600 can also be run in $reverse\ start - stop$ mode where the detector signal starts the timing electronics and the reference signal stops the timing electronics.

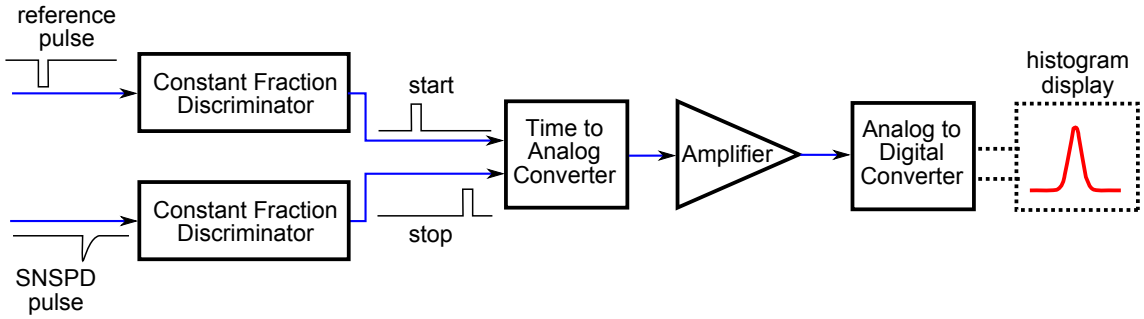

Figure 3.27: Operating principle of Becker and Hickl Time Correlated Single-Photon Counting card [7].

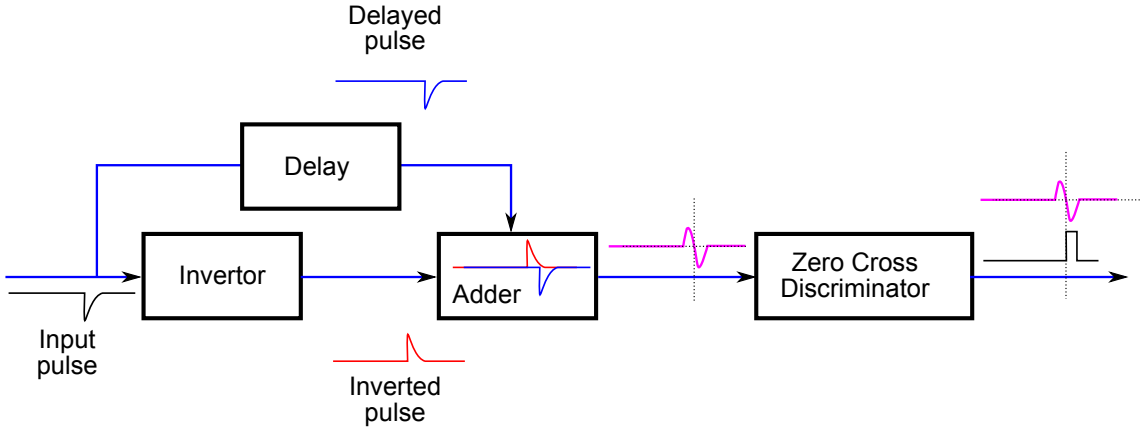

Figure 3.28: Working principle of a Constant Fraction Discriminator (CFD): the electrical signal is duplicated, delayed and added to an inverted version of the original signal. The zero crossing point of the resultant signal is used to generate a pulse by the discriminator [7].

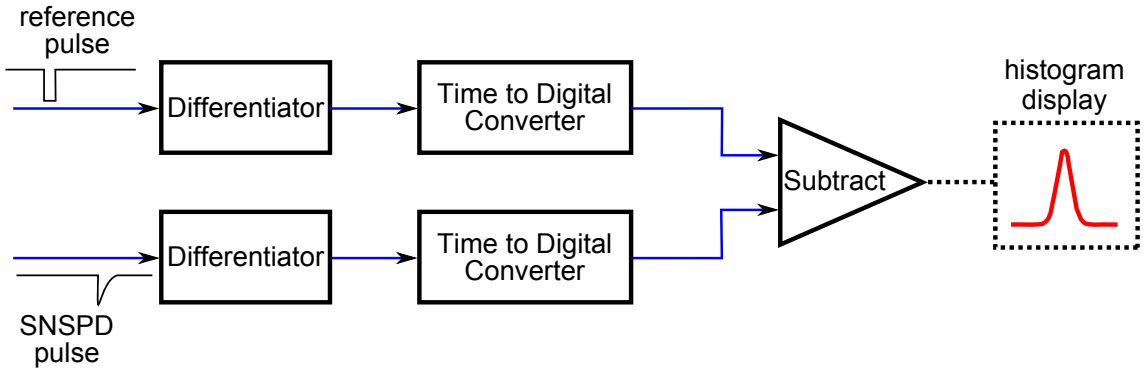

Figure 3.29: Operating principle of PicoHarp TCSPC Card: Differentiator is used instead of CFD to timestamp the signal [129].

Even though the working principle of the PicoQuant PicoHarp 300 is similar to the Becker & Hickl TCSPC card, the implementation is slightly different. PicoHarp converts both the signals into digital timestamps in the initial stage (figure 3.29). These timestamps are digitally subtracted and the difference is histogrammed with better resolution. The key difference is that the PicoHarp's CFD does not operate in the traditional way. It uses a differentiator to analyse the input signal and time stamps the zero-cross point of the differentiated signal (i.e. zero-cross corresponds to the peak of the pulse). These new features of the PicoHarp mean that it does not require reverse start-stop mode for better operation.

3.5 Summary

SNSPDs are typically operated at $\sim 2 - 4$ K employing cooling techniques such as the traditional liquid He cryostat [17], cryogenic probe-station [64] or Gifford-McMahon cryocooler [63]. Liquid He offers a rapid cooling technique but this aggressive thermal cycling can degrade the superconducting nanowires and also prevent stable fibre-coupling. The probe station offers rapid characterisation of many devices on a single chip with a movable probe, which favours device development rather than application. Also in this configuration it is hard to eliminate stray light and blackbody radiation, leading to dramatically elevated dark count rates. We have utilised the advantages offered by Gifford-McMahon cryoolers to build a portable, application-oriented multichannel SNSPD system. This chapter discussed solutions to various engineering issues involved in building this detector system. Following the successful construction of my detector system (figure 3.30), we have further built several detector systems: a cryostat for nano-optical testing at Heriot-Watt University (J. A. O'Connor), a detector system for single-photon source characterisation for the UK National Physical Laboratory, NPL, (C. R. Fitzpatrick) and a detector system for quantum key distribution and eavesdropping experiments for University of Toronto, Canada (V. Burenkov).

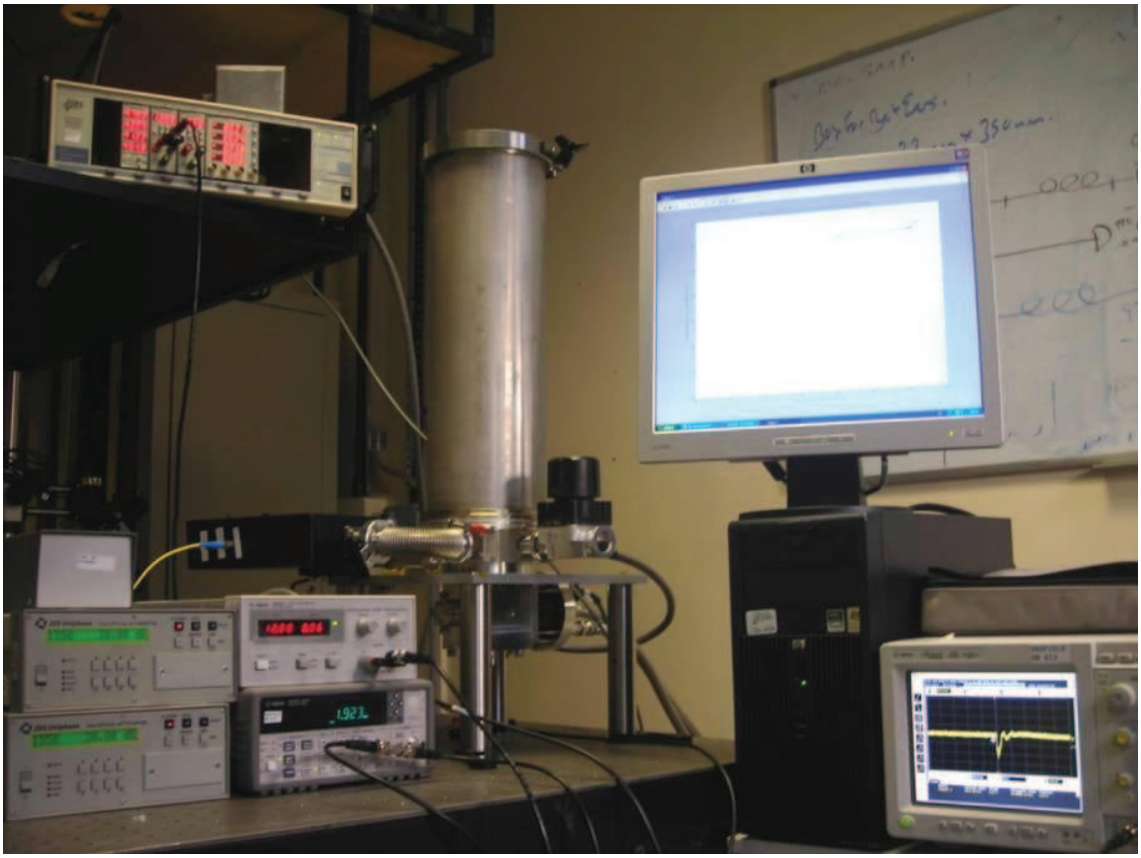

Figure 3.30: Photograph of SNSPD detector system at Heriot-Watt University.

Chapter 4

Comparison of Performance of NbN and NbTiN SNSPDs

As discussed in the previous chapter, the closed-cycle cryocooler system allows us to characterise packaged SNSPD devices reliably and systematically. With this capability, the aim was to select SNSPDs with good performance out of those available and use them in potential applications. Since there are no facilities at Heriot-Watt University to fabricate detectors at present, the SNSPDs presented in this thesis were provided by our international collaborators. Primarily we had access to two types of SNSPDs (i) NbN nanowire on MgO substrate from NICT, Japan (these were available from the first year of my research – June, 2008 onwards)[1] and (ii) NbTiN nanowire on oxidised silicon from TU Delft, The Netherlands (these were available from the middle of the second year of my research – May, 2009 onwards)[2]. Fabrication procedure of these devices is briefly mentioned in section 4.1. The chapter then focuses on electrical and optical measurement results of each type of detector (section 4.2). NbN and NbTiN devices have similar superconducting properties, therefore offer similar electrical characteristics. Optical alignment of 20 μm $\times$ 20 μm NbN devices is relatively more easy than aligning to 10 μm $\times$ 10 μm NbTiN devices,

[1] Special thanks to S. Miki, M. Fujiwara, M. Sasaki and Z. Wang for supplying NbN devices for this thesis.

[2] Author is also extremely grateful to S. N. Dorenbos, E. Bermúdez Ureña, V. Zwiller, T. Zijlstra and T. M. Klapwijk for providing NbTiN devices. The author took the lead in all the measurements in this chapter. M. G. Tanner and V. K. Pottapenjara also took part in the characterisation of the NbTiN SNSPDs at Heriot-Watt University.

although the latter could also be successfully fibre-coupled. The overall system detection efficiency (η_{sde}) of NbTiN SNSPDs is higher than NbN devices. The results are summarised in table 4.1. $\eta_{\text{sde}}^{\text{NbTiN}}$ measured a maximum of ~30% at 1310 nm. The SiO_2/Si interface beneath the NbTiN acts as a cavity mirror enhancing the absorption of 1310 nm photons in the nanowire. This result was published in reference [22].

Source	Material	Substrate	830 nm	1310 nm	1550 nm
NICT	NbN	MgO	15.2%	5.8%	3.4%
TU Delft	NbTiN	SiO_2 on Si	4.0%	30.0%	18.0%

Table 4.1: Summary of best overall system detection efficiencies (η_{sde}) measured at ~2.3 K with 1 kHz dark count rate for 20 μm × 20 μm NbN and 10 μm × 10 μm NbTiN devices. Coupling losses have not been subtracted in these measurements.

4.1 Discussion of Fabrication and Alignment

NICT, Japan and TU Delft, The Netherlands have well established ultra-thin film growth and electron-beam lithography (EBL) facilities at their disposal. This has allowed them to successfully fabricate superconducting nanowire single-photon detectors. NICT's state of the art fabrication facility allows them to fabricate larger area devices [68] than the conventional $\leq$ 10 μm × 10 μm devices reported from Moscow [17]. Aligning a 9 μm diameter core fibre to a 20 μm × 20 μm active area results in a very high coupling efficiency ($\eta_{coupling}$). On the other hand, TU Delft group is interested in integrating SNSPDs with silicon technology [130]. Their choice is to grow NbTiN films on Si wafer with a 225 nm SiO_2 buffer layer for lattice matching. A quick summary of the fabrication process is presented in section 4.1.1.

4.1.1 Summary of the superconducting nanowire fabrication process

NbN SNSPD: NbN thin films are grown by using reactive dc magnetron sputtering. The thin films are grown by sputtering a Nb target in an Ar/N_2 plasma on

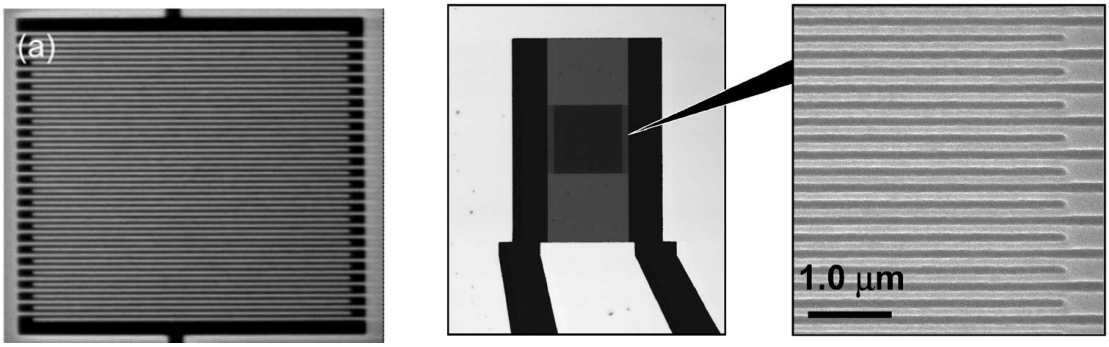

(a) NbTiN SNSPD (b) NbN SNSPD

Figure 4.1: Scanning Electron Microscope (SEM) images of (a) NbTiN SNSPD – the nanowire is shown by the darker region and (b) NbN SNSPD – the left image shows the meander embedded in the 50 Ω RF coplanar waveguide structure, the zoomed image shows the nanowire pattern (lighter region is the NbN nanowire in this image). Images reproduced from: (a) reference [130] and (b) reference [68].

lattice matched substrates such as Al_2O_3 (Sapphire) [17], MgO [131] at substrate temperatures ranging from 300 – 1200°C [60]. NbN films with best T_c and lowest resistivity are obtained when grown on MgO. These films have a critical temperature of $T_c^{NbN} = 10$ K at 4 nm thickness. Since MgO substrates are hydrophilic and expensive, large scale deposition remains a hurdle. Sapphire substrates are often preferred for large scale NbN deposition since they are chemically inert. At NICT, NbN ultra-thin films are grown epitaxially on unheated single crystal MgO (100) substrate. In the sputter system, the substrate is relatively close (∼cm) to a large magnetron. This high quality NbN film has a low defect density. The sheet resistance at 20 K is ∼350 Ω/□. These ∼4 nm films have very low resistivity compared to films grown using RF sputtering technique. The device is fabricated in a two EBL step process. In the first step, EBL is used to define the step pads and markers followed by evaporation (Ti/Au 70 nm thick) and standard lift-off using a Poly-Methyl MetAcrylate (PMMA), a positive tone electronic resist, as a stencil mask. In the next step, Hydrogen SilsesQuioxane (HSQ), a negative tone resist, is used to define the device on top of the NbN film. Fluorine based Reactive Ion Etching (RIE) is used to remove the unwanted NbN and Ti/Au material, i.e. the uncovered region of the mask. The SNSPD consists of a 100 nm wide and 2 mm long nanowire meandering across a relatively large area (20 μm × 20 μm) with a fill factor of 50%.

Typically a device has 20,000 unit □s resulting in ∼7 MΩ resistance at 20 K. The device is embedded in a 50 Ω RF coplanar waveguide structure as in figure 4.1(b).

NbTiN SNSPD: An SNSPD fabricated on a silicon wafer is an exciting prospect for fabricating nanowires on top of dielectric mirrors or silicon-on-insulator structures to improve absorption efficiency. This also allows future development of optical circuits in a single chip by integrating with planar optical waveguide technology [23]. 6 nm thick NbTiN film is deposited on a 225 nm SiO_2 buffer layer on a Si substrate by reactive ion sputtering (using $Nb_{0.7}Ti_{0.3}$ alloy as target in Ar/N_2 plasma at room temperature). These NbTiN thin films have a critical temperature of 15 K. The critical current density of NbTiN is comparable to that of NbN ($\sim 6 \times 10^6$ A/cm^2) therefore NbTiN devices are expected to display similar electrical properties to those of NbN devices. These 100 nm wide nanowires, typically folded into 10 μm×10 μm meanders (figure 4.1(a)) with 50% fill factor, are patterned by e-beam lithography and etched by RIE with a resist mask of HSQ. These nanowires are also embedded in a 50 Ω coplanar waveguide structure and have gold contact pads. A detailed discussion of NbN and NbTiN fabrication processes have been presented in references [131] and [130] by the respective groups. Anticipating possible integration of SNSPDs with photonic structures in the future, efforts have been made to fabricate SNSPDs on other semiconductor substrate such as GaAs [132].

At Heriot-Watt University, these detectors are fibre-coupled, characterised and evaluated for use in photon-counting experiments. The SNSPD is cleaned using acetone and isopropyl alcohol before mounting it on a gold plated OFHC copper sample mount (figure 3.6). The chip is held securely by a pair of Be-Cu clips or the chip is stuck to the sample mount with the help of silverpaste. Occasionally a thin layer of vacuum grease is also applied underneath the chip to hold it to the sample mount. For electrical connection, aluminium wire is wedge-bonded to gold contact pads and a small piece of RF-Printed Circuit Board (PCB). This RF-PCB is soldered to a commercially available SMP coaxial connector mounted in the sample mount. Once good contact is confirmed by measuring the room temperature resistance, the device is ready for optical alignment.

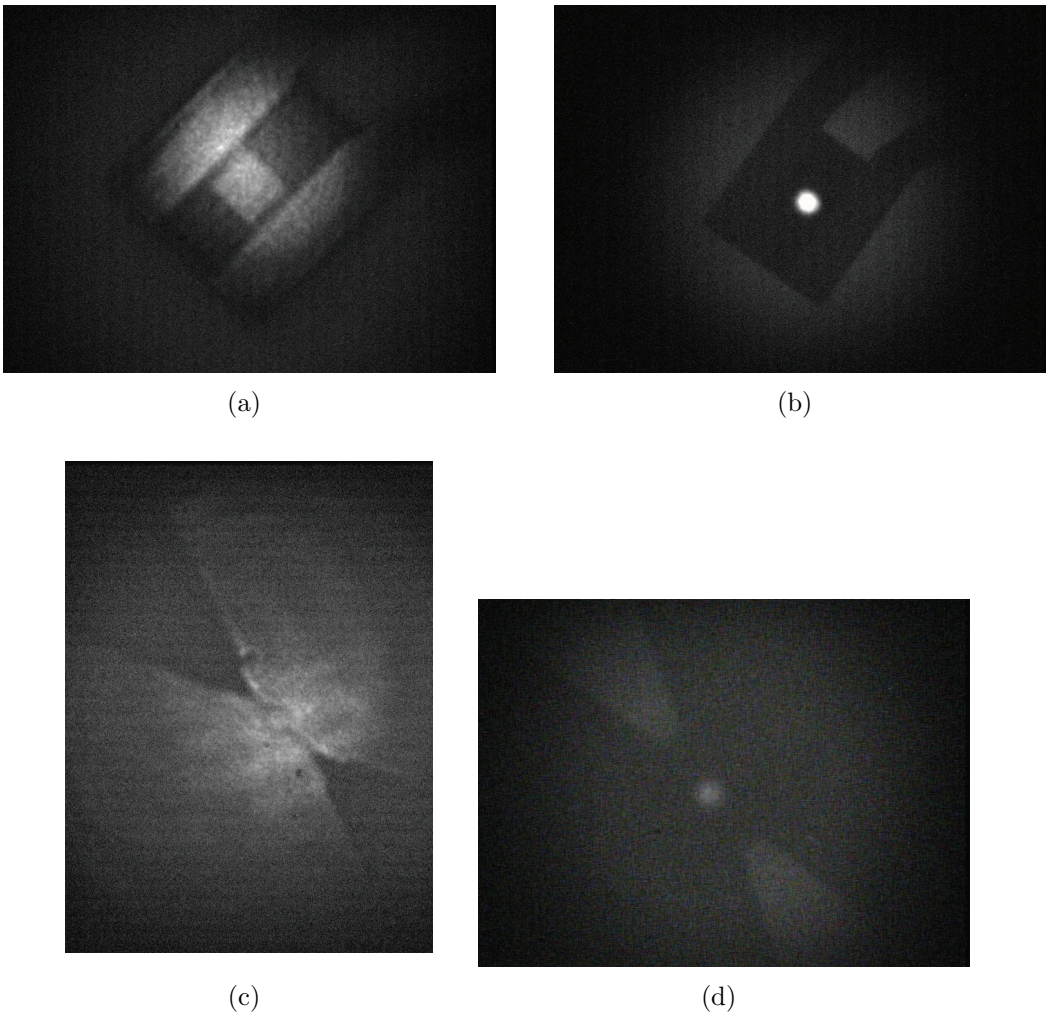

(a) (b)

(c) (d)

Figure 4.2: Images of the SNSPD nanowire device captured through the wafer using alignment microscope system. The bright spot in the middle of each image is the 1550 nm light coming out of the end of the fibre ferrule. NbN device with (a) an unfocused and (b) focused spot on the nanowire. NbTiN device with (c) an unfocused and (b) focused spot on the nanowire.

4.1.2 Optical alignment challenges

The optical alignment consists of typically 2 steps (as discussed in previous chapter in section 3.2): (i) to set the distance between end of fibre ferrule and the chip to ~ 50 μm (measured via OCT) and (ii) to align the ~ 10 μm diameter optical spot to the active area of the device. The first step is relatively straightforward once precautionary steps are taken to avert the possibility of the zirconia ferrule coming in contact with the Be-Cu clip. This can crush the detector sandwiched between the clip and sample mount from the pressure applied by the ferrule. The distance between chip and ferrule is precisely controlled by varying the number of 25 μm thick stainless steel shims used. The second step is a demanding task because the margin of error is very small. The ferrule is first positioned away from the chip to exploit the beam divergence to identify the nanowire meander area precisely as shown in figure 4.2(a) and 4.2(c). Depending on the fabrication process the Au features are not necessarily exactly aligned to the SNSPD meander. With the knowledge of the accurate position of the nanowire meander, the ferrule is brought close to the chip as defined in step (i) and bolted using brass screws with appropriate pressure, over-pressure can break the head of the screw and under-pressure fails to retain the alignment over thermal cycling. The most difficult part of the procedure is when the ferrule is brought closer and closer to the chip, the beam divergence reduces and the focused spot does not show up any contrast between the nanowire region and its surroundings as in figure 4.2(b) and 4.2(d). The level of difficulty varies depending on the type of detector. Aligning NbTiN devices is more difficult than aligning NbN devices, since the optically sensitive area is smaller than NbN devices by a factor of four. Figure 3.9 shows that $\eta_{\text{coupling}} = 0.8$ can be achieved for a 10 μm$\times$10 μm device using a 9 μm core SMF28 fibre when the ferrule is placed 25 μm away from the device without misalignment in x-y axis. With identical settings $\eta_{\text{coupling}} \approx 1$ can be achieved for a 20 μm$\times$20 μm device. Even a high η_{qe} device can end up with poor η_{sde} due to misalignment (*i.e.* low η_{coupling}). Any misjudgement in the alignment stage can cost a lot of time, since η_{coupling} can be improved only after a cool-down (~ 8 hrs), testing (~ 1 hr) and subsequent warm-up (~ 7 hrs). Readers should also note that for NbTiN on Si devices, the through-wafer alignment scheme needs flood illumination and imaging at $\lambda > 1$ μm wavelength. This is due to Si not

being transparent for wavelengths less than 1 μm.

4.2 Discussion of Electrical and Optical Performance of NbN and NbTiN SNSPDs

In total, 15 NbN devices and 17 NbTiN SNSPD devices have been characterised in this thesis work. The optical and electrical performance observed varies widely across each batch of detectors for both types. It should be noted that the approach presented to package and test the devices does not alter either physical or chemical properties of the nanowire. The variation in characteristics is attributed to defects introduced to the superconducting nanowires during the fabrication [69]. A defect in the nanowire restricts the amount of current flowing in the nanowire which in turn limits the η_{qe} of the SNSPD. Results from the two best NbN and NbTiN devices characterised in Heriot-Watt University are presented in this section.

The fibre-coupled detectors are secured to the stand-off stage of the cryostat and cooled down to ~ 2.3 K. The critical currents of NbN and NbTiN devices are measured as 22.5 μA and 30 μA respectively. Variation in output voltage pulse shapes of the devices is presented in section 4.2.1. The key device performance parameters, namely timing jitter (section 4.2.2) and system detection efficiency as a function of wavelength (section 4.2.3), are also discussed.

4.2.1 Comparison of output pulse shapes

The output pulse of the single-photon detector must be correctly prepared in order to trigger a TCSPC card (section 3.4.3). The main requirement for triggering the input channel of a TCSPC card is a pulse height of 50 – 300 mV with a clean leading edge. The pulse shape of the SNSPD plays a major role in its usefulness in many photon-counting applications. The SNSPD's output pulse is expected to have (i) a very steep leading edge to enable a clear time stamp, (ii) large amplitude pulses for good signal-to-noise ratio and (iii) small trailing edge for a shorter dead time. The pulse shapes of NbN and NbTiN devices, biased just below the critical current, are shown in figure 4.3.

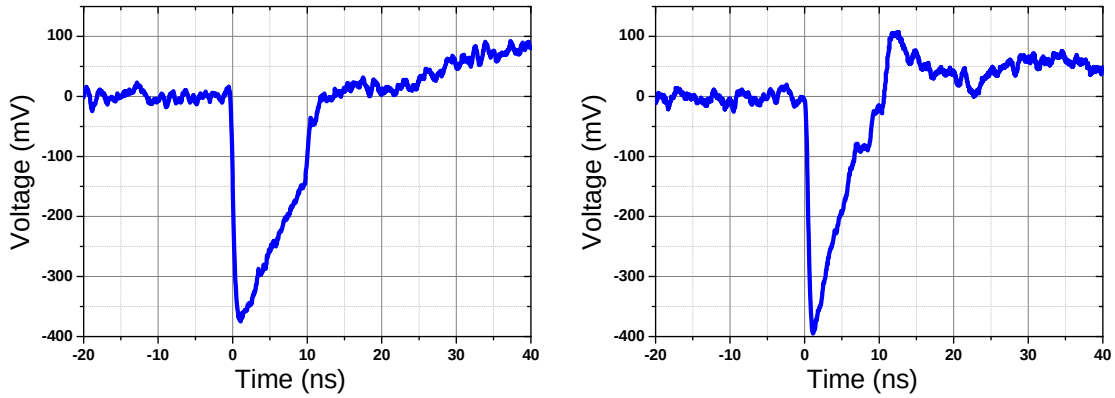

(a) (b)

Figure 4.3: Comparison of the output pulse shapes of (a) NbN and (b) NbTiN SNSPD devices. The output pulses were amplified by RFBay LNA-580 and LNA1000 inverting amplifier chain and were recorded using a 8 GHz Agilent Infiniium oscilloscope. A 50 Ω shunt resistor was used in both cases. The critical current of the NbN and NbTiN SNSPD were 22.5 μA and 30μA respectively and were biased at 90% of their I_c at ∼2.3K.

The leading edge of both detector types are dominated by the hotspot resistance. Hotspot resistance is ∼2.5 K from simulation discussed in the earlier chapter (section 3.3.2). Sample pulse shapes from NbN and NbTiN superconducting nanowires have been plotted in figure 4.3. The raw output pulse from SNSPD was amplified using LNA-580 amplifier with a 3 dB roll-off at 580 MHz and followed by LNA-1000 amplifier with 30 dB roll-off at 1 GHz. The amplified pulses were recorded using a Agilent Infiniium 8 GHz oscilloscope (DSO80804A). The ∼1 ns time constant set by $L_k/(50 + R_n)$ does not allow any distinction between the NbN and NbTiN devices for an instrument operating below 1 GHz bandwidth. However, NbTiN pulse height is taller than NbN device. This is attributed to the smaller detector area. For a given defect density, the larger the area of the meander, the greater the number of constrictions, thus limiting critical current I_c [69]. The critical current directly affects the pulse height i.e. $V_{pulse} \approx 50 \times I_{bias}$. NbTiN devices ought to be more uniform since it is 4 times shorter that NbN device, thus the larger pulse height. A longer superconducting nanowire has another disadvantage in possessing larger kinetic inductance given by $L_k = \mathcal{L}_k \int ds/A(s)$, where A(s) is the cross sectional area of the nanowire, $\mathcal{L}_k$ is the inductance per unit length and integration is along

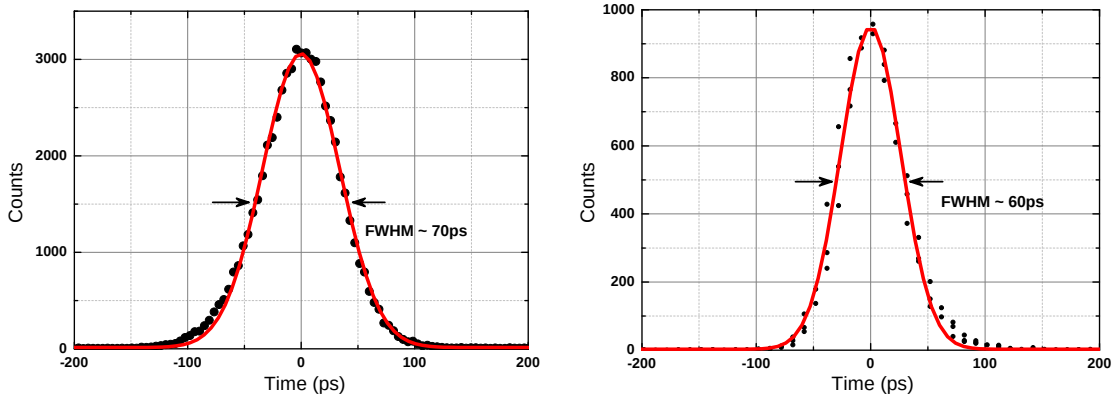

(a) NbN (b) NbTiN

Figure 4.4: Comparison of Jitter of (a) NbN and (b)NbTiN SNSPD devices. The instrument response histogram was measured using a B&H SPC600 card with bin width=4 ps. The red curve is a Gaussian fit to the measured data (black dots).

the nanowire length. The NbN devices have a longer dead-time compared to NbTiN detectors due to longer trailing edge (based on the initial curvature of the trailing edge in figure 4.3).

4.2.2 Comparison of timing resolution

The timing jitter of SNSPD plays a major role in any TCSPC applications using these detectors. The smaller the uncertainty in detector's timing resolution, the more precisely the arrival time of a photon can be known. Jitter of these devices have been measured using apparatus discussed in earlier chapter (section 3.4.3). The results shown in figure 4.4 were measured using a Becker & Hickl SPC600 card with 4 ps bin-width and 13 ps FWHM jitter [7]. Both these devices have a similar timing response around ∼60 ps (FWHM). The slight reduction in the NbTiN jitter could be attributed to the shorter nanowire, improved signal to noise and smaller thermal time constant of NbTiN.

4.2.3 Comparison of system detection efficiency

The wide spectral sensitivity is a key feature of the SNSPD device. Characterising η_{sde} over a wide range of wavelengths is challenging task due to the need for

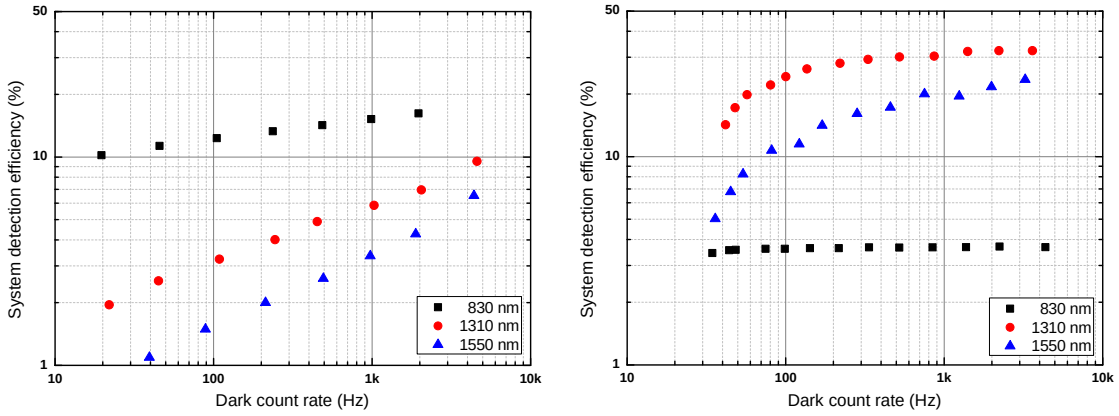

(a) NbN (b) NbTiN

Figure 4.5: Comparison of η_{sde} of NbN and NbTiN SNSPDs at wavelengths 830, 1310 and 1550 nm at 2.3 K.

calibrated attenuators, power meters and relevant optics at each wavelength. We have restricted our primary interest to characterising the detectors at the following wavelengths: 830 nm, 1310 nm and 1550 nm. In each case, we acquired an off-the-shelf fibre pigtailed diode laser. The practice throughout the thesis was to estimate η_{sde} at wavelengths 830 nm, 1310 nm and 1550 nm for all the devices using system described in section 3.4.1. For both NbN and NbTiN devices, η_{sde} is plotted against dark count rate for all three wavelengths in figure 4.5. Error bars could be added to the system detection efficiency vs dark count rate plots based on the fit, but the dominant uncertainty in this type of measurement is the systematic calibration uncertainty of the power meter. Recalling equation 2.1, η_{sde} can be broken down as $\eta_{coupling} \times \eta_{absorption} \times \eta_{wavelength} \times \eta_{registering}$. From the plots, the following can be observed:

- Increasing bias current I_{bias} increases $\eta_{registering}$: In figure 4.5, the x-axis represents the increase in bias from left to right (increasing dark count rate). Raising I_{bias} increases η_{sde} by pushing $\eta_{registering}$ towards unity because even the smallest hotspot formed can drive the nanowire resistive due to increased current density and Joule heating in the region. However as I_{bias} approaches I_c, it also increases the dark count rate.

- Decreasing wavelength increases $\eta_{wavelength}$: $\eta_{wavelength}$ increases as the energy

of the photon rises (*i.e.* wavelength decreases). As the energy of the photon goes up, the curves get flatter, this is because $\eta_{registering}$ saturates for a lower bias current. This is very clear from the NbTiN's 830 nm η_{sde} vs DCR curve (4.5(b)).

For a front-side coupled NbN nanowire meander structure, the dependence of the system detection efficiency at constant bias on wavelength is given as $\eta_{sde} \propto e^{-k\lambda}$ [32] where k is the fitting constant. The η_{sde}^{NbN} confirms this relationship in figure 4.6(a). The $\eta_{absorption}$ for a front-side coupled NbN nanowire device varies only by a factor of 1.5 between 800 nm to 1550 nm (even for the least favourable polarisation condition). This is inferred from the simulated data in figure 4.6(b) [128]. This simulation using the Finite Element Method (FEM) takes into account the variation in refractive index of NbN with wavelength and the wire grid pattern of the NbN nanowire device. Therefore the drop in η_{sde} can be attributed to the drop in $\eta_{registering}$ due to the decrease in energy of the photon as the wavelength increase. The striking feature in the figure 4.6(a) plot is that the η_{sde}^{NbTiN} does not go up with energy of photon as in literature [32]. In NbTiN devices, $\eta_{absorption}$ seem to be enhanced at 1310 nm wavelength as compared to 830 nm or 1550 nm wavelength. This suggests a cavity effect in the device. This aspect of the NbTiN device is attributed to the SiO_2/Si interface upon which the superconducting film is grown [22]. This is discussed in detail in the following section.

4.2.4 Role of SiO_2/Si interface in NbTiN SNSPD

Enhanced absorption at 1310 nm is studied by calculating absorption probability across a wide spectrum using transfer matrix simulations (Essential Macleod software package [133]). Multilayer reflection was simulated from a 225 nm SiO_2 layer on top of a Si substrate. At 1310 nm, the refractive index of SiO_2 is 1.45, Si is 3.5 and the measured refractive index (n, k) of (4.17, 5.63) was used for NbTiN in the simulation. An unpatterned 10 nm NbTiN film was used to determine (n, k) by ellipsometry at room temperature. The calculated absorption efficiency is plotted in figure 4.7(a), clearly indicating a increased absorption (∼65%) at 1310 nm than at 1550 nm or 830 nm. This peak at 1310 nm is due to the maximum electric field at the NbTiN film due to the SiO_2 layer matching the optical thickness of $\lambda_{\text{eff}}/4 = 225$ nm

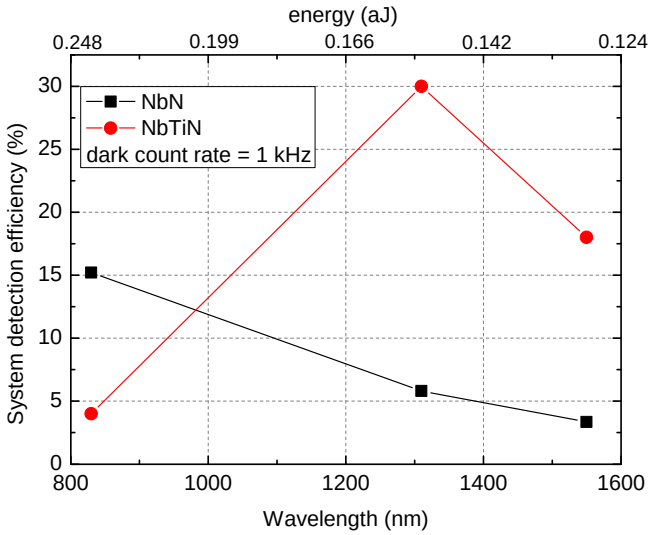

(a)

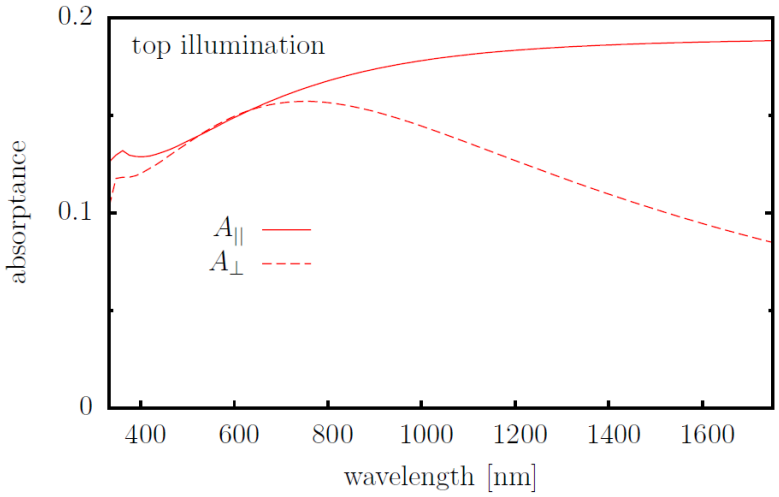

(b)

Figure 4.6: (a) System detection efficiency against wavelength for both NbN and NbTiN SNSPD detectors at 1 kHz darkcount rate and 2.3 K, The top axis gives the energy of a single-photon at the respective wavelengths (b) Finite-Element-Method simulated result of absorption ratio for a front side coupled NbN wiregrid structure. Graph reproduced from reference [128].

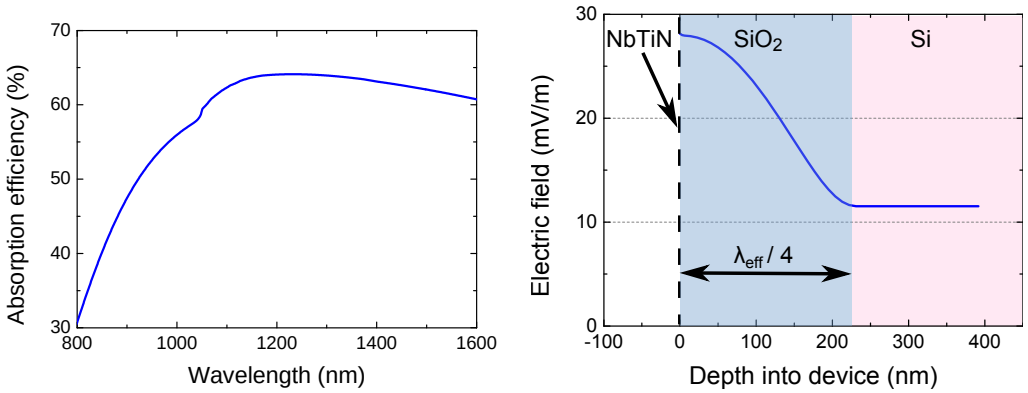

(a) (b)

Figure 4.7: Simulated data of (a) photon absorption probability in NbTiN layer and (b) electric field present in the nanowire and SiO_2/Si layers assuming 10^6 photons are incident on a 10×10 μm^2 area at $\lambda = 1310$ nm wavelength.

(figure 4.7(b)). In other words, the SiO_2/Si interface acts as a half cavity mirror due to the refractive index mismatch. The simulations[1] give a resonable picture of the absorption properties but may not match the measurements quantitatively. This is due to the lack of refractive index information for the materials with detector dimensions at cryogenic temperatures. $\eta_{absorption}$ falls down to 15% in the absence of the half cavity mirror at 1310nm; confirming the SiO_2/Si interface as the sole reason for the enhanced efficiency. More detailed study of dependence of η_{sde} on λ[2] was carried out using a white-light source and monochromator with calibrated filters and the results have been included in reference [22].

In summary, the $\eta_{registering}$ increases as the I_{bias} increases irrespective of superconducting nanowire being present in a cavity or not. The device becomes more sensitive at higher I_{bias} near the I_c. Similarly reducing the photon wavelength i.e. increasing the photon energy also enhances the registering probability. The key difference between the devices is highlighted by the increase in absorption efficiency ($\eta_{absorption}$) for selective wavelengths due to the partial mirror beneath the nanowire. This shows that wavelength specific cavities can be integrated with SNSPDs to enhance overall η_{sde} at that wavelength by improving $\eta_{absorption}$.

[1]Simulations were carried out by M. G. Tanner, HWU.
[2]This experiment was performed at NIST, USA by R. H. Hadfield, B. Baek and S. Nam

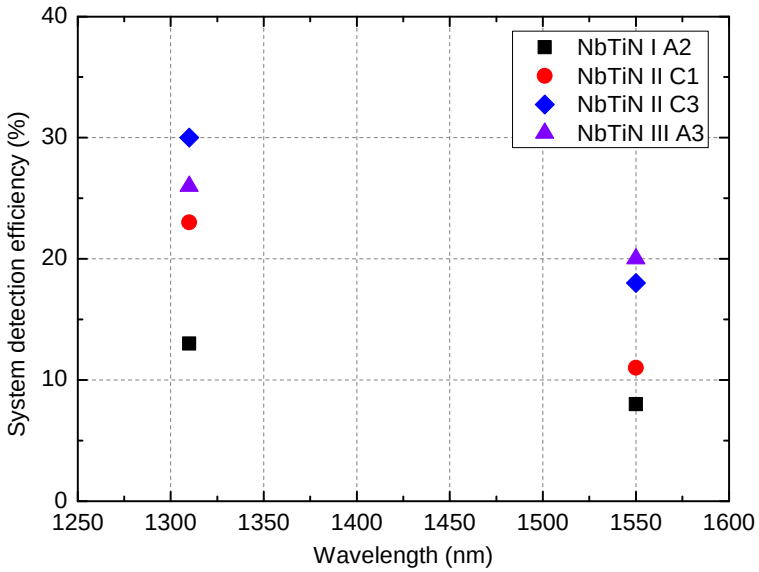

Figure 4.8: Summary of η_{sde} of current SNSPD detector system performance at wavelengths 1310 nm and 1550 nm at 2.3 K and 1 kHz darkcount rate.

4.3 Evolution of Multichannel SNSPD System

In the beginning of this thesis work (November, 2007), only η_{sde} upto 1% had been reported for frontside fibre-coupled SNSPDs [21, 134]. In August 2008, similar performance was achieved in Heriot-Watt University using NbN devices fabricated in NICT, Japan. $\eta_{\text{sde}} = 1.3\%$ was measured at 3.2 K for $\lambda = 1550$ nm. In March 2009, the multichannel system had four NbN devices with $\eta_{\text{sde}} > 1\%$ at $\lambda = 1550$ nm and $\sim$2.3 K. In June 2009, new nanowire devices based on NbTiN from TU Delft were characterised. These devices had a higher efficiency of $\eta_{\text{sde}} = 21\%$ at $\lambda = 1310$ nm and $\eta_{\text{sde}} = 8\%$ at $\lambda = 1550$ nm. In October 2010, four NbTiN devices with average $\eta_{\text{sde}} = 20\%$ at $\lambda = 1310$ nm and average $\eta_{\text{sde}} = 10\%$ at $\lambda = 1550$ nm have been installed. The performance of the current system is presented in figure 4.8. All η_{sde} quoted in this paragraph are for 1 kHz darkcount rate.

4.4 Outlook on Improving System Detection Efficiency

Quantum efficiencies (excluding coupling loss) of 57% for 1550 nm photons at 1.8 K, have been demonstrated by embedding a 3 μm $\times$ 3 μm nanowire meander inside an optical cavity and coupling the light through the substrate [18] in 2006. Our NICT collaborators have also demonstrated a similar scheme with a front-side mirror and coupling via the substrate [135]. This new scheme has challenges – the wafer either has to be ground to $\sim$ 40 μm thickness for good $\eta_{coupling}$ [18] or a lensed fibre may be used [135]. To enhance $\eta_{absorption}$, nanowires are patterned on top of wavelength specific SiO_2/Si [22, 130, 136] or GaAs/AlAs distributed Bragg mirrors [132]. The advantage is that frontside coupling is sufficient to enhance $\eta_{absorption}$ for these devices.

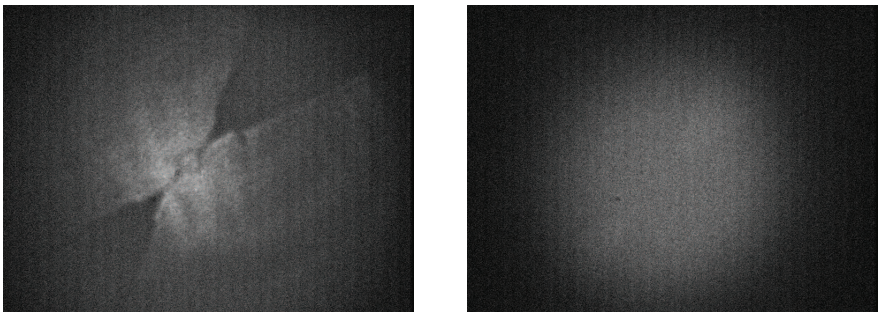

(a) (b)

Figure 4.9: Images of optical alignment of NbTiN nanowire devices on DBR mirrors. (a) an unfocused spot from the fibre end is used to locate the device (b) when the spot from the fibre end is focused on the device, the contrast is poor between the nanowire region and DBR mirror.

In our case, the enhanced absorption efficiency peaks at 1310 nm by virtue of the 225 nm layer of SiO_2 underneath the nanowire, alternatively by changing the thickness of SiO_2 to 267.5 nm (= 1550 nm/(4 $\times$ 1.45)) the $\eta_{absorption}$ can be improved at 1550 nm. $\eta_{absorption}$ can be further improved by designing a Distributed Bragg Reflector (DBR) at the wavelength of interest. In January 2010, trial devices with preliminary DBR designs were tested [1]. The DBR consist of Si(substrate) /

[1]The devices were fabricated by E. Bermúdez Ureña, TU Delft.

5 × [SiO_2(270 nm) / Si_3N_4(190 nm) / SiO_2(270 nm)] wafer. The difficult task is growing high quality superconducting thin films on DBR structures. The tested devices had very low critical current ($\sim$ 0.5 μA) – indicating defective nanowire resulting in poor η_{sde} ($\sim$0.006% at 1550 nm and 1KHz dark count rate). Additionally these devices require an alignment system operating at a different wavelength for efficient optical coupling, since the current 1550 nm alignment scheme does not allow us to focus on the device. Poor contrast between the light reflected back from the device and DBR structure was observed (see figure 4.9).

4.5 Conclusion

In this chapter, I have described the alignment and low temperature optical and electrical characterisation of two types of SNSPD supplied by NICT, Japan and TU Delft, the Netherlands. The 20 μm×20 μm area NbN on MgO devices could be fibre-coupled robustly and efficiently. High performance NbN SNSPDs were successfully installed in our detector system in August, 2008. This enabled experiments described in next chapter to be carried out. In June 2009, the NbTiN SNSPDs were fibre-coupled and characterised at telecom wavelengths for the first time. These devices gave enhanced performance (peaking at 30% at 1310 nm). Currently, four high performance NbTiN SNSPDs are installed in our detector system.

Chapter 5

Applications: Characterising Quantum Waveguide Circuits with SNSPDs[1]

Quantum Information Science and Technology (QIST) has been a topic of increasing interest for the research community over the past few decades [95]. Quantum computers may not replace conventional computers in all applications but promise to offer high processing power in specific tasks such as searching a database [137], factoring prime numbers [138] and in quantum simulations [139]. The key requirement is that the quantum object must interact only with other intended quantum objects and be isolated from the environment. When the relevant wavefunction starts to interact with its surroundings – decoherence occurs i.e. information is lost or errors are introduced. Evolution of physical quantum computer implementations will favour quantum objects and systems which are scalable and correctable with the least additional resource requirements. The scalability and correctability depends on the basic unit for information processing. The quantum analogue of classical bit is a *qubit*, a quantum system with binary state. Leading technologies and their respective binary states employed in quantum computing are (1) Nuclear Magnetic Resonance [140] – nuclear spin orientations give the two states of information, (2) trapped atoms [141] – the energy levels of the atoms form qubits, (3)

[1]This work was done in collaboration with A. Peruzzo and J. L. O'Brien from University of Bristol.

superconductors [142, 143] – charge qubits, phase qubits and flux qubits in Josephson junction circuits, (4) quantum dots [144] – exchange coupled electron or hole spins, (5) trapped ions [145] – electronic states of trapped ions and (6) photons [24] – qubit states are defined via polarisation, phase, time-bin and spatial modes.

The optical photon is an excellent candidate for the storage and processing of quantum information [23]; it is isolated from the environment even at room temperature, travels at the speed of light and can be controlled with available optical technology. Following the theoretical proposal of Knill, Laflamme and Milburn (KLM) [97] to use linear optics to construct entangling gates, considerable strides have been made in manipulating photonic qubits in the laboratory. An ultimate technological goal is a compact device capable of scalable quantum information processing. Silicon optical waveguide technology (coplanar lightwave circuit technology) has been adapted to build on-chip optical quantum information circuits [146].

In this work, we bring together two highly promising enabling technologies for photonic quantum information science and technology: quantum waveguide circuits [11, 147] and NbN Superconducting Nanowire Single-Photon Detectors (SNSPDs). The aim for this study was to verify the compatibility between these technologies and explore the advantages and disadvantages of using SNSPD over Si-SPAD.

5.1 Discussion of Technologies Involved

Unlike classical computing, quantum computing does not have a unique set of universal gates [24, 95]. Almost any two-qubit gate (entangling operation) along with single-qubit gates (to prepare a state) can be the building blocks of complex quantum information processing systems. For a spatially encoded optical qubit, a beamsplitter can be used to prepare the photon in any arbitrary quantum state. Beam combination and splitting is achieved in lightwave waveguide technology by utilising the evanescent coupling between spatial modes. The coupling ratio is analogous to the transmission coefficient of a beam splitter. As a first step, operating waveguide directional couplers with SNSPDs is an important step to demonstrate compatibility between SNSPDs and quantum waveguide circuits. The other key requirement

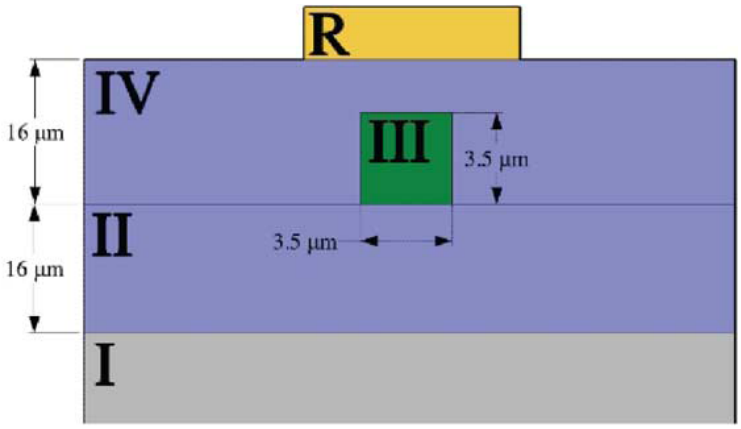

Figure 5.1: Schematic of the structure of silica-on-silicon waveguide chip. Material I is the Si wafer, material II is undoped-silica acting as the lower cladding, material III is the germanium or boron oxide doped silica acting as the core, material IV is phosphorus and boron-doped silica acting as the upper cladding and material R is a metallic layer acting as a resistive heater. Schematic reproduced from reference [146].

for testing the compatibility is generation of indistinguishable photon pairs[1]. This section discusses these two technologies.

5.1.1 Silica-on-Silicon quantum waveguide circuits[2]

Scalability of quantum photonics demands the use of planar lightwave circuits in linear optical quantum computing [23]. This system has two major advantages (i) low waveguide loss (< 0.1 dB/cm) and (ii) compatibility with commercial optical fibres. The basic waveguide consists of a central core and outer lower refractive index cladding structure. The silicon fabrication techniques result in a square core supporting a single transverse mode for a given wavelength and efficient coupling between optical fibre and waveguides. A single silica-on-silicon waveguide chip can replace numerous bulk or fibre optical components. The waveguides[3] used

[1]The photons are considered distinguishable if they have different frequencies, arrival times or coherence times. In practice, indistinguishability strongly depends on the details of the experiment.

[2]The quantum waveguides were designed and characterised by A. Politi and J. C. F. Matthews from University of Bristol.

[3]All devices were fabricated at the Centre for Integrated Photonics, UK.

in these experiments were designed to operate at wavelength λ ~800 nm. This choice was due to availability of high detection efficiency single-photon detectors at λ ~800 nm (namely commercial Si Single-Photon Avalanche Detectors (Si-SPADs)). The waveguide structure is given in figure 5.1. It consists of a 16 μm layer of thermally grown undoped silica on a silicon wafer as the lower cladding, a 3.5 μm$\times$ 3.5 μm lithographically patterned structure of germanium and boron oxide doped silica as the core and a 16 μm phosphorous and boron doped silica layer grown to form the upper cladding. Metal patterns on top of the waveguides are used as resistive heaters to locally change the temperature of the waveguides. A suitable refractive index contrast (=0.5%) is chosen, between core and cladding, for moderate mode confinement. A single transverse optical mode is supported at the design wavelength, allowing evanescent coupling between adjacent waveguides and precise control of single-photon states and multiphoton entanglement within a waveguide chip. Directional couplers are fabricated for beam splitting operations. Evanescent coupling between two adjacent waveguides can be altered by varying the separation between the waveguides. The coupling coefficient is tuned to achieve 50:50 coupling between the two waveguides at design wavelength, identical to a 50:50 optical beam splitter. Several experiments have recently been carried out demonstrating the versatility and power of this technology in QIST [11, 147, 148].

5.1.2 Indistinguishable photon pair source

In our experiment, photon pairs are generated using Spontaneous Parametric Down-Conversion (SPDC) [149]. A pump photon ω_p interacts with a non-linear crystal in the right orientation to give birth to two daughter photons with frequencies ω_1 and ω_2 such that energies are conserved as in equation 5.1. Phase matching conditions preserve the conservation of momentum inside the crystal. The non-linear crystal is chosen depending on the second order susceptibility $\chi^{(2)}$ of the non linear material.

$$\omega_1 + \omega_2 = \omega_p \tag{5.1}$$

SPDC can be summarised as:

$$|\Psi_{SPDC}\rangle = |00\rangle + \epsilon\,|11\rangle + \epsilon^2\,|22\rangle + \cdots, \tag{5.2}$$

where $|xx\rangle$ is the creation of x number of photons in each of two different modes and ϵ is parameter depending on $\chi^{(2)}$, phase matching conditions, length of the crystal and intensity of the laser pump. Generally ϵ is very small. In our experiment, pairs of photons at $\lambda = 804$ nm were generated by SPDC of continuous wave (CW) 402 nm laser diode "pump" beam in a type I phase matched bismuth borate (BiB_3O_6) (BiBO) non-linear crystal. The photon pair collection rate was measured as $\sim$5000 s^{-1} when collected into Polarisation Maintaining Fibres (PMFs) and coupled directly to twin Si-SPADs. Wavelength degenerate pairs of 804 nm photons were selected using a 2 nm bandpass filter in each path and coupled into PMFs.

5.1.3 Description of experimental setup

We tested compatibility between SNSPDs and quantum waveguide circuits via a two-photon interference experiment in a 50:50 directional coupler waveguide circuit as in figure 5.2. PMFs were butt-coupled to the 50:50 coupler waveguide chip, with index matching fluid inserted at the fibre-waveguide interface. Index matching fluid was used to minimise Fresnel reflections at the fibre-waveguide interface. The output photons from the directional couplers were similarly coupled into Single Mode Fibres (SMFs) and were detected using two SNSPD detector channels. Overall waveguide coupling efficiencies of 70% were achieved (input + output insertion loss = 30%). Simultaneous detection of a photon at each output of the coupler was recorded using a time-correlated single-photon counting module (PicoHarp 300) with 4 ps bin.

5.2 Discussion of Experimental Results

To study the advantages and disadvantages of using SNSPDs over Si-SPADs with integrated quantum photonic circuits it is necessary to perform a two-photon quantum interference using a silica-on-silicon 50:50 directional couplers with either type of these detectors. Since this experiment is a coincidence basis measurement, the better timing jitter of the SNSPDs is bound to improve on the results obtained using Si-SPADs. Subsequently, we used SNSPDs to operate two important quantum waveguide circuits at $\lambda = 804$ nm: a Controlled-NOT (CNOT) quantum logic gate comprising 0.5 and 0.33 directional couplers and a Mach-Zehnder interferometer

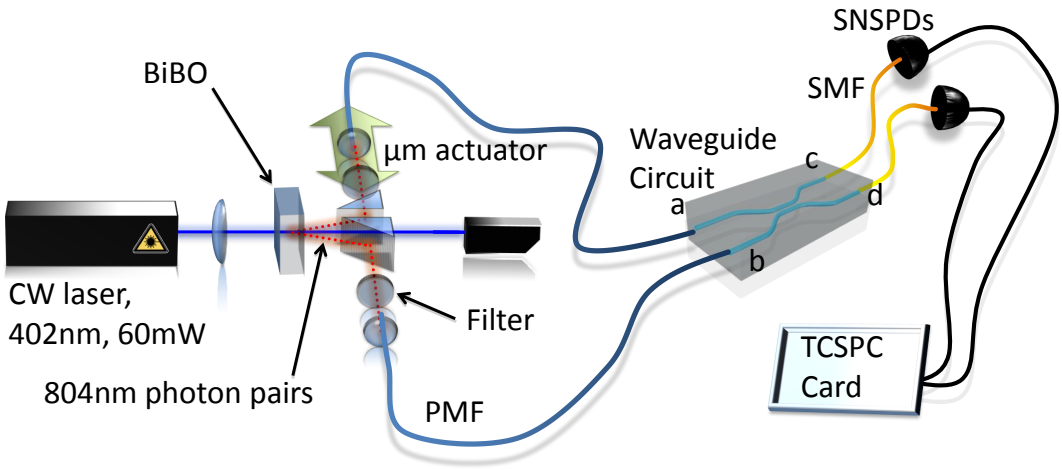

Figure 5.2: Experimental setup for the two-photon interference experiment. Photon pairs at $\lambda = 804$ nm are generated by spontaneous parametric down-conversion of 402 nm CW light in a Type-I non-linear BiB_3O_6(BiBO) crystal. Photon pairs were collected and coupled to the 50:50 coupler waveguide through a polarisation maintaining fibre (PMF). The outputs of the waveguide circuit are routed to a pair of single-photon detectors (SNSPDs or Si-SPADs) via single mode optical fibre (SMF). Coincidences between the detector channels are recorded using a time-correlated single-photon counting (TCSPC) card (PicoHarp 300) (figure courtesy of Prof. J. L. O'Brien).

with a voltage-controlled phase shift.

5.2.1 The Hong-Ou-Mandel interferometer

Ideally, when two degenerate photons are simultaneously sent into the two input waveguides a and b of a 50:50 directional coupler (figure 5.2), quantum interference results in a path entangled state of the two photons in the two output waveguides (c and d):

$$|1\rangle_a |1\rangle_b \rightarrow \frac{|2\rangle_c |0\rangle_d + |0\rangle_c |2\rangle_d}{\sqrt{2}}; \tag{5.3}$$

No simultaneous photon detection events take place due to the absence of a $|1\rangle_c |1\rangle_d$ term in this superposition as discussed in section 2.4.2. By introducing relative delays between arrival of each of the photons at the beamsplitter the two-photon interference effect can be reduced. This variation in interference is known as the

Hong-Ou-Mandel (HOM) effect [96]. The relative arrival time of the photons at the directional coupler was varied by controlling the free space path difference using a micrometer actuator (figure 5.2). As this path delay is varied a dip in the coincidence from the output modes of the beamsplitter is observed at zero delay (HOM dip). The quality of the two photon interference is characterised by the depth of HOM dip. It is quantified by visibility

$$V = (N_{max} - N_{min})/N_{max} \tag{5.4}$$

In theory, visibility is a function only of the reflection coefficient ($\mathscr{R}$) given in equation 5.5, but in practice the quality of the dip can suffer from distinguishable photons within the photon pair.

$$V_{Theory} = \frac{2\mathscr{R}(1-\mathscr{R})}{1-2\mathscr{R}+2\mathscr{R}^2} \tag{5.5}$$

The two-photon interference experiment at $\lambda = 804$ nm was performed using both NbN-SNSPDs and conventional Si-SPAD detectors. In our experimental setup, the source brightness and optical alignment remained stable over a period ∼1 hour, limiting the experimental duration. The results are shown in figure 5.3. The acquisition time per data point was 60 s using SNSPDs and 40 s using Si SPADs. Both cases show a high visibility HOM dip. Typically V is calculated after subtracting the rate of "accidental coincidences". Accidental coincidences occur either due to detectors being triggered from photons in different pairs arriving within the coincidence time window, or by dark counts in one or other detector providing a spurious trigger. The SNSPD allows both contributions to be minimized due to low D and Δt. The measured accidental rates were ∼0.01 Hz for SNSPDs and ∼5 Hz for Si-SPADs. Therefore background subtraction was unnecessary in the SNSPD case. The raw V of the HOM dip obtained using SNSPDs was $92 \pm 1\%$, whereas that of the Si-SPADs was $89.9 \pm 0.3\%$. The uncertainties were calculated using the methods elaborated in Appendix A. The larger uncertainty in the SNSPD data is due to the slower coincidence accumulation rate during the overall measurement time. The details of the fit are presented in Appendix B. Following normal practice, the Si-SPAD result can be corrected via accidental subtraction. The corrected visibility for the Si-SPAD is

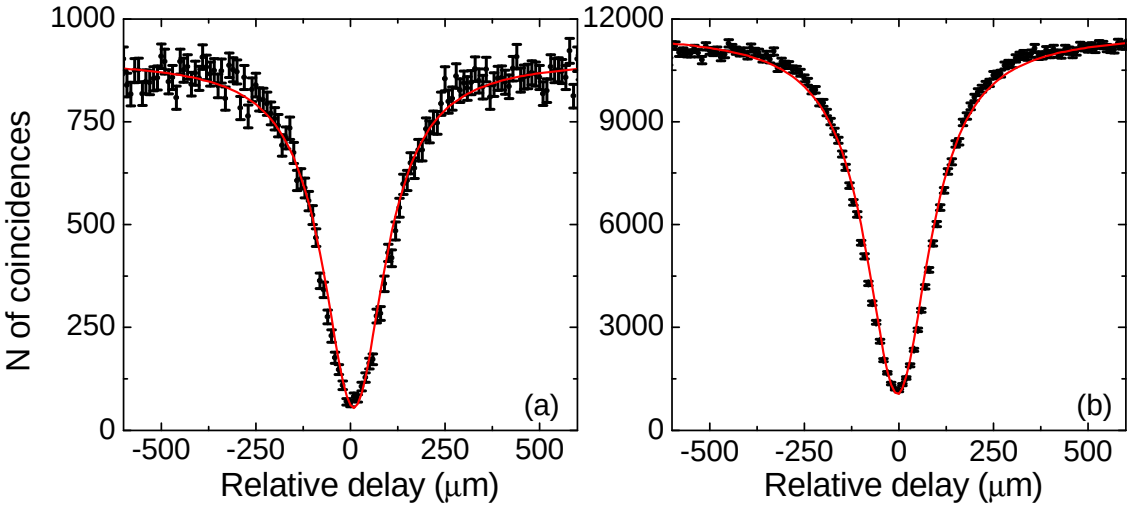

Figure 5.3: Two-photon interference in a quantum waveguide circuit at $\lambda = 804$ nm. HOM dip obtained using (a) NbN SNSPDs and (b) Si-SPADs. The acquisition time per data point was 60 s for the SNSPDs and 40 s for the Si-SPADs. Poissionian error bars of $\sqrt{N}$ are shown, where N is the number of coincidences.

$92.6 \pm 0.4\%$, matching the "raw" SNSPD result. Non-unity visibility is attributed to the spectral distinguishability of the photons.

5.2.2 Controlled-NOT gate

A CNOT gate can be seen as a non-linear phase shifter in between two Hadamard gates as in figure 5.4(a). A Hadamard gate (H)[1] can be realised using a 50:50 beamsplitter. In linear quantum optical computing [97], the non-linear phase shift can be achieved with help of $\frac{1}{2}$ and $\frac{1}{3}$ beamsplitters (BS) as in figure 5.4(b). An interferometer is formed with the target modes using two 50:50 beam splitters. The control qubits interact with the target qubits by the central $\frac{1}{3}$ BS in figure 5.4(b). When the control photon is in $|0\rangle_{logic}$, the photon entering in either of the target mode leaves the interferometer in the same spatial mode. This is preserved by $\frac{1}{3}$ BSs in each arm of the interferometer. When control qubit$= |1\rangle_{logic}$, quantum interference in the middle $\frac{1}{3}$ BS introduces a π phase-shift in the upper arm of the interferometer. This results in a flip in target qubit and no change in control qubit as in table 5.1. The

[1] $H \equiv \frac{1}{\sqrt{2}} \begin{bmatrix} 1 & 1 \\ 1 & -1 \end{bmatrix}$

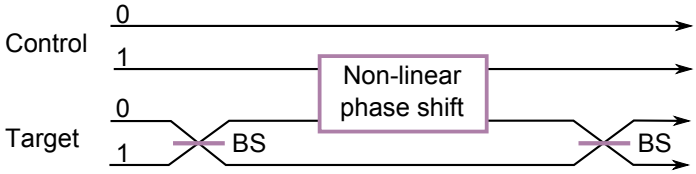

(a) CNOT schematic

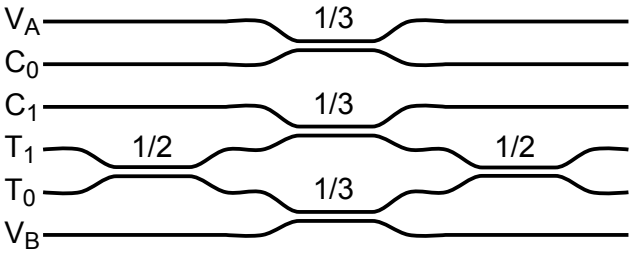

(b) Probabilistic CNOT gate

Figure 5.4: (a) Schematic of a CNOT gate constructed using a non-linear phase shifter and beamsplitters (b) schematic of probabilistic CNOT gate constructed using only beamsplitters and relying on two-photon interference [23]. The modes C_x, T_x and V_x represent the control, target and unoccupied ancillary modes respectively.

Control	Target	CNOT
$\|0\rangle$	$\|0\rangle$	$\|0,0\rangle$
$\|0\rangle$	$\|1\rangle$	$\|0,1\rangle$
$\|1\rangle$	$\|0\rangle$	$\|1,1\rangle$
$\|1\rangle$	$\|1\rangle$	$\|1,0\rangle$

Table 5.1: Truth table of an ideal Controlled-NOT gate

probability of detecting single-photon in both control and target modes is equal to 1/9. However, when we do measure two single-photons CNOT operation has been performed. Thus a CNOT gate is a probabilistic, coincidence basis circuit built using only beam splitters.

SNSPDs are ideally suited to the characterisation of CNOT gates, as the CNOT gate measurement relies on a coincidence basis operation. The CNOT gates used in the experiment were characterised and presented in reference [11] using Si-SPADs. The CNOT waveguide chip consists of silica waveguides written lithographically on a silicon substrate represented by the schematic structure in figure 5.4(b). The CNOT gate was characterised by inputting the four computational basis states ($|00\rangle, |01\rangle, |10\rangle, |11\rangle$) and measuring the corresponding output probabilities. The

Input $\|CT\rangle$	$P_{\|00\rangle}$	$P_{\|01\rangle}$	$P_{\|10\rangle}$	$P_{\|11\rangle}$
$\|00\rangle$	0.98 ± 0.08	0.02 ± 0.08	0	0
$\|01\rangle$	0.01 ± 0.07	0.99 ± 0.07	0	0
$\|10\rangle$	0	0	0.20 ± 0.06	0.80 ± 0.06
$\|11\rangle$	0	0	0.84 ± 0.07	0.16 ± 0.07

Table 5.2: Measured probabilities for the logical basis CNOT gate operation. The quantum waveguide CNOT gate was characterised using SNSPD detectors at wavelength $\lambda = 804$ nm

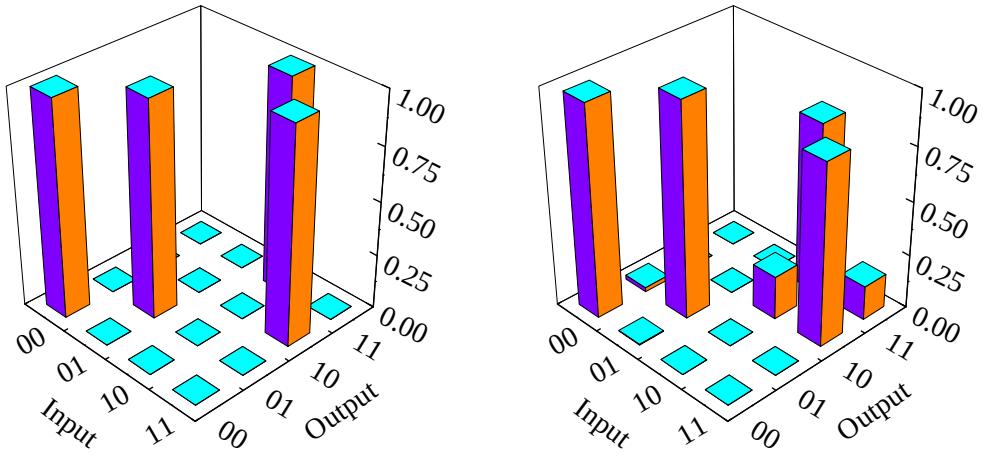

(a) Ideal

(b) Measured

Figure 5.5: (a) Ideal CNOT gate probabilities (b) Measured probabilities for the logical basis CNOT gate operation using SNSPDs. The silica-on-silicon quantum waveguide circuit was operated at wavelength $\lambda = 804$ nm.

data is tabulated in table 5.2 and compared against ideal truth table in figure 5.5. In the classical regime, i.e. for $|C\rangle = 0$ state the gate work well with probability values $98 \pm 8\%$ and $99 \pm 7\%$. For state $|C\rangle = 1$ the device underperforms due to quantum interference; with $80 \pm 6\%$ and $84 \pm 7\%$ probability values. Imperfections in the reflection coefficients of the beamsplitters can degrade the visibility of the two-photon interference. The average of the logical basis is defined as the fidelity of the CNOT gate. A logical basis fidelity, F, of 90% was observed. Even though the operation of CNOT gate has been demonstrated the entanglement of the photons has not been tested explicitly.

5.2.3 Mach-Zehnder interferometer

In quantum information science, any compatibility testing should probe the generation of entangled states. Figure 5.4(a) shows that the CNOT gate is a interferometer with a π phase shifter in one of the arms, controlled by the $|C\rangle$ qubit. Replacing the constant phase shifter with a variable phase shifter enables detailed study of entangled states generated in the interferometer. The variable phase shift is achieved by varying the refractive index of the waveguide locally. The metal pattern on the top of the waveguide acts as a resistive heater, which in turn varies the refractive index of the waveguide (see figure 5.1). The quantum mechanical unitary operator of a Mach-Zehnder interferometer at a single-photon level is given as

$$U_{MZ} = U_{DC} e^{i\phi\sigma_Z} U_{DC} \tag{5.6}$$

U_{DC} is the unitary operation of a 50:50 beamsplitter. Two indistinguishable single-photons entering mode 'a' and 'b' transforms into a maximally path entangled state of two photons across modes 'c' and 'd'. A relative phase shift 2ϕ is introduced into the entangled state and the two modes recombine at the subsequent beam splitter.

$$|1\rangle_a |1\rangle_b \rightarrow \frac{1}{\sqrt{2}}(|2\rangle_c |0\rangle_d + |0\rangle_c |2\rangle_d) \tag{5.7}$$

$$\frac{1}{\sqrt{2}}(|2\rangle_c |0\rangle_d + i\,|0\rangle_c |2\rangle_d) \rightarrow \frac{1}{\sqrt{2}}(|2\rangle_c |0\rangle_d + ie^{i2\phi}\,|0\rangle_c |2\rangle_d) \tag{5.8}$$

The quantum operation of the Mach-Zehnder circuit was characterised by inputting a single-photon in both inputs to generate the state of eqn. 5.7 inside the interferometer. The two-photon interference fringe is shown figure 5.6(b), using two-photon state and varying the phase $\phi(V)$. A contrast of $81 \pm 2\%$ was observed.

The resulting Mach-Zahnder (MZ) circuit (figure 5.6(a)) can be potentially used as a direction coupler with a reconfigurable reflectivity. The unitary operation U_{MZ} in terms of phase shift ϕ is:

$$U_{MZ} = \begin{pmatrix} sin(\phi/2) & cos(\phi/2) \\ cos(\phi/2) & -sin(\phi/2) \end{pmatrix} \tag{5.9}$$

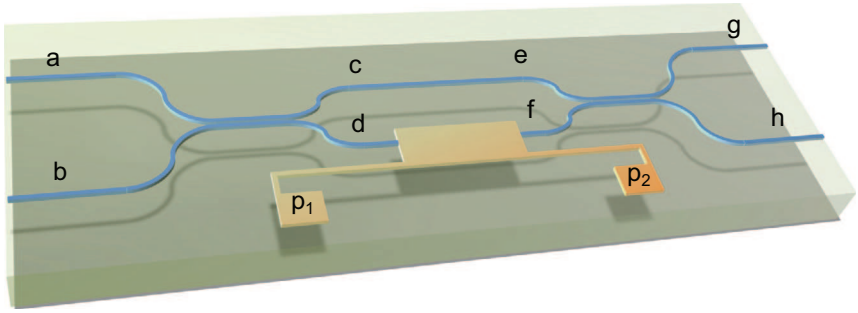

(a) MZ circuit

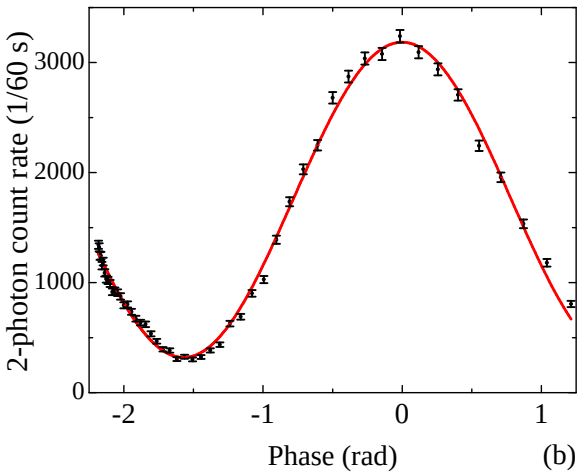

(b) 2NOON fringe

Figure 5.6: (a) Schematic of an integrated Mach-Zehnder interferometer. The phase-shifter is realised using the resistive heater. Schematic reproduced from reference [147]. (b) Two-photon coincidental count rate measured using SNSPD and PicoHarp 300 between the outputs g and h with $|1\rangle_a |1\rangle_b$ as the input and phase varied by heating the metallic resistor on the waveguide.

	Wavelength λ	Efficiency η_{sde}	Dark count rate D (Hz)	FWHM JitterΔt (ps)	η_{sde}^2	$\eta_{sde}/D\Delta t$
Si-SPAD	804 nm	0.45	200	350	0.203	6.43×10^6
NbN SNSPD	830 nm	0.1	20	60	0.01	8.3×10^7
NbN SNSPD	1550 nm	0.01	40	60	0.0001	4.2×10^6
NbTiN SNSPD	1550 nm	0.1	70	60	0.01	2.3×10^7

Table 5.3: Comparison of the properties of Si-SPAD (manufacturer specifications [8]), NbN SNSPD and NbTiN SNSPD (data from figure 4.5).

Variation in ϕ results in reconfigurable reflection coefficient $\mathscr{R}$

$$\mathscr{R} = sin^2\frac{\phi}{2} \tag{5.10}$$

5.3 Outlook on quantum waveguide circuit experiments with SNSPDs

In summary, the experiments have demonstrated the compatibility between quantum waveguide circuits and SNSPDs at $\lambda = 804$ nm. SNSPDs give an improved visibility over Si-SPADs in a HOM experiment via a 50:50 waveguide coupler. The difference arises owing to the detector properties. The characteristics of the two detector types are given in first rows of the table 5.3, in terms of system detection efficiency η_{sde}, ungated dark count rate D and FWHM timing jitter Δt. A figure of merit which combines these properties [1] and reflects the signal-to-noise ratio is given by $\eta_{sde}/D\Delta t$. Considering the signal-to-noise of the two detector types is important because in a time-correlated single-photon counting experiment, the effect of the dark count rate can be mitigated by gating or time binning. The minimum effective

binning interval is set by the detector jitter Δt. Here, owing to the low dark counts and excellent timing jitter, the NbN-SNSPD outperforms the Si-SPAD by a factor >10. We are able to exploit this advantage fully in our experimental setup, as the resolution of our electronics (4 ps) is well below Δt for either detector type. The higher V obtained using the SNSPDs is due to the better signal-to-noise. The accumulation rate of coincidences (off the HOM dip) was 14 s^{-1} for the SNSPD and 275 s^{-1} for the Si-SPAD (a ratio of 20:1). This corresponds well to η_{sde}^2 in each case (table 5.3). The longer accumulation time is a disadvantage of using low efficient detector, but higher quality results can be obtained with a stable experimental setup.

The 2NOON fringe contrast and CNOT gate's fidelity achieved show that SNSPDs can be successfully used to characterise advanced quantum waveguide circuits. The contrast and fidelity is somewhat lower than that reported in reference [11, 147] using Si-SPADs; this is because the SNSPD results are limited by the acquisition time (determined by the stability of our optical setup used in the experiment).

The main reason for operating these waveguides at $\lambda = 804$ nm, until this point, was simply due to lack of commercial single-photon detectors with free running operation and low dark counts at telecommunication wavelengths. SNSPDs present a solution to this problem. The performance of SNSPDs with currently improved telecommunication wavelength efficiency is presented in table 5.3. At 1550 nm, NbTiN SNSPDs offer improved SNR over NbN SNSPDs by a factor of ∼5. NbTiN devices also improve the 2-photon coincidence probability by a factor of 100, when compared to NbN devices. This confirms the feasibility of operating quantum waveguide circuits at λ =1550 nm for the first time in QIST experiments. It should be noted that the commercially available InGaAs SPADs have not been included in the discussion since they are typically run in gated mode to mitigate high dark-count rates. Gated-mode operation with long dead time is an inefficient choice for coincidence measurements. A Hong-Ou-Mandel dip with a visibility of 96.3% was recently measured using a commercially available 50:50 polarising beamsplitter and NbTiN detectors at telecom wavelengths. The HOM dip is plotted in figure 5.7. 1550 nm photon pair source was generated using a BiBO SPDC source. The coincidence measurement was performed with a PicoHarp TCSPC module. The next step is to implement quantum waveguide circuits at 1550 nm and characterise them using SNSPDs. A switch to $\lambda = 1550$ nm will allow the full range of telecommu-

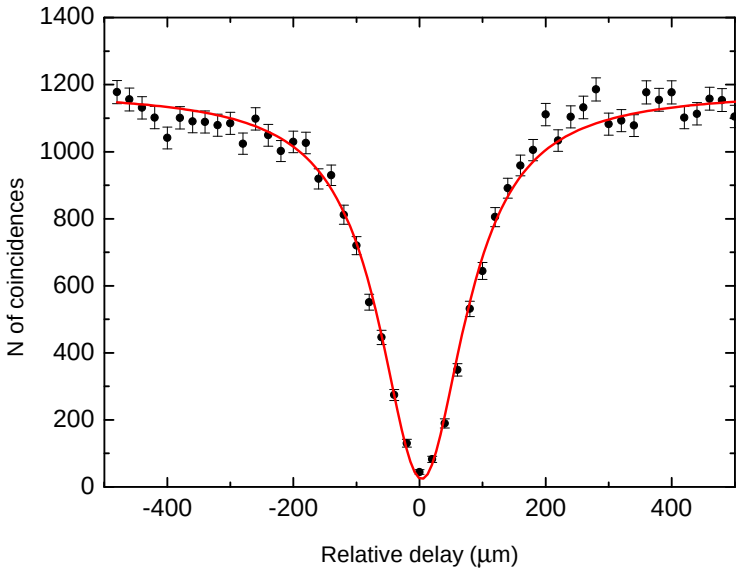

Figure 5.7: Two-photon interference observed in a 50:50 polarising beamsplitter at $\lambda = 1550$ nm. Hong-Ou-Mandel dip was measured using NbTiN SNSPDs.

nication waveguide technologies to be exploited. Currently experiments are being conducted in University of Bristol investigating variety of commercially available lithium niobate waveguide products at telecommunication wavelengths with the improved detector system built during this thesis work.

Chapter 6

Conclusions

6.1 Summary of the Thesis Work

This thesis work has demonstrated a robust method for operating Superconducting Nanowire Single-Photon Detector (SNSPD/SSPD) with excellent practical performance, using a closed-cycle cryocooler system. A cryostat was built around a commercially available Gifford-McMahon cryocooler [150] (see figure 3.30). The target temperature of ∼2.5 K was reached even with a heat load of 8 SNSPD packages. This cryostat overcomes the disadvantages of traditional liquid He cryostats. Transportable nature of the SNSPD system was demonstrated by employing the detectors in challenging optical quantum information science experiments at the University of Bristol [25].

The first stage of this thesis work was to establish facilities to package and characterise SNSPDs at Heriot-Watt University. Standard SMF28 telecommunications optical fibre was chosen as the optical interface to improve the portability and compatibility with other optics experiments. Fibre-coupling techniques were optimised to efficiently couple the photons to the detector at 1550 nm, with control of the fibre-device spacing down to ∼25 μm [150]. The SNSPD and fibre ferrule are packaged such that the coupling varies only minimally over multiple thermal cycles. Laboratory facilities were also established to enable full characterisation of SNSPDs at a selection of key wavelengths (830 nm, 1310 nm and 1550 nm). Robust measurements of practical detection efficiency, dark count rate, and timing jitter were performed to

the standards of measurements previously carried out at the US National Institute of Standards and Technology [21].

Initially, SNSPD devices based on NbN nanowires patterned on MgO substrates (supplied by NICT, Japan [68]) were characterised. The best system detection efficiency (SDE) measured is ∼3% for 1550 nm photons with a dark count rate of 1 kHz and ∼70 ps (FWHM) jitter. This result is comparable to similar devices reported in the literature [68]. This was an improvement by a factor of 3 for fibre-coupled detectors reported at the start of this work [21]. The fine-tuned packaging and characterisation techniques allowed us to investigate a new SNSPD based on NbTiN nanowires (supplied by TU Delft, The Netherlands [130]) at telecom wavelengths. Record SDE for front-side (not via substrate) fibre-coupled detectors was measured at ∼20% for 1550 nm photons (∼30% for 1310 nm photons) with ∼60 ps FWHM jitter and 1 kHz dark count rate. This improved efficiency is due to the partial reflector (SiO_2/Si interface) formed beneath the nanowire [22]. In our study, we have achieved very high practical efficiency without resorting to the use of laborious thinning of the substrate [18] or expensive *in-situ* nano positioning [151]. Currently, our main detector system consists of 4 fibre-coupled NbTiN SNSPD channels with individual system efficiencies >20% at 1310 nm. Moreover, my work has led to the construction of duplicate SNSPD detector systems at Heriot-Watt university for the UK National Physical Laboratory (delivered December 2009) [152] and the University of Toronto, Canada (delivered September 2010).

Optical quantum information science applications place stringent demands on single-photon detectors [1]. The advantages of SNSPDs have been demonstrated elsewhere by employing them in long-distance, high speed quantum key distribution experiments [20]. The excellent signal-to-noise ratio and timing precision of the SNSPD allowed new world records to be set in terms of secure transmission distance and bit rate. The realisation of a quantum computer is a long term research goal for this field [3]. Quantum waveguide circuit technology offers a promising and potentially scalable platform for an optical quantum computer [11, 147]. We have employed our high performance SNSPDs in challenging quantum waveguide experiments involving quantum interference. Operations of Hong-Ou-Mandel interferometer, Mach-Zehnder interferometer and CNOT gate were demonstrated using a photon pair source at 804 nm, silica-on-silicon waveguide circuits and NbN SNSPDs.

These results demonstrated the advantages of SNSPD over conventional Si single-photon avalanche diode in this application (figure 5.3). The negligible dark counts and narrower jitter of SNSPD allow higher fidelity results to be obtained [25]. Recently we have used efficient NbTiN SNSPD devices to observe a Hong-Ou-Mandel dip using a 1550 nm photon-pair source.

6.2 Future Work Based on this Thesis

SNSPDs were first introduced a decade ago [17] and a major worldwide effort has built up only over the last five years. Developments in this field are accelerating rapidly: there is immense potential to improve the practical performance of the devices and to explore opportunities to use SNSPD in new areas of research. My view of the outlook for this field is discussed below.

6.2.1 Scope for improvement in detection efficiency

Even though this thesis work has demonstrated system detection efficiencies up to 30%, this performance is inadequate for the most challenging photon-counting applications such as linear optical quantum computing [101]. A further improvement in the practical efficiency of the detector is needed. The NbTiN SNSPD on oxidised silicon substrate confirms that by patterning the nanowire on top of a partial mirror the efficiency improves significantly. Next step to further improve absorption is to pattern the nanowire on top of a high reflectivity Distributed Bragg Reflector (DBR). The reflectivity of the DBR can be tuned to specific wavelengths. For example, a fine-tuned DBR designed for 1550 nm photons can improve the absorption efficiency to $\sim$100% at λ=1550 nm but the penalty is that these devices will lose broadband efficiency. The practical advantage is that we can use the same packaging scheme explained in this thesis to achieve high detection efficiencies. Several groups have recently demonstrated progress in this area, but practical performance falls short of the best predictions [132, 136].

The efficiency of the devices can also be enhanced by improving the coupling efficiency. The two coupling techniques which can be attempted are (i) etching aided alignment and (ii) waveguide coupling. *Etching aided alignment*: in this scheme,

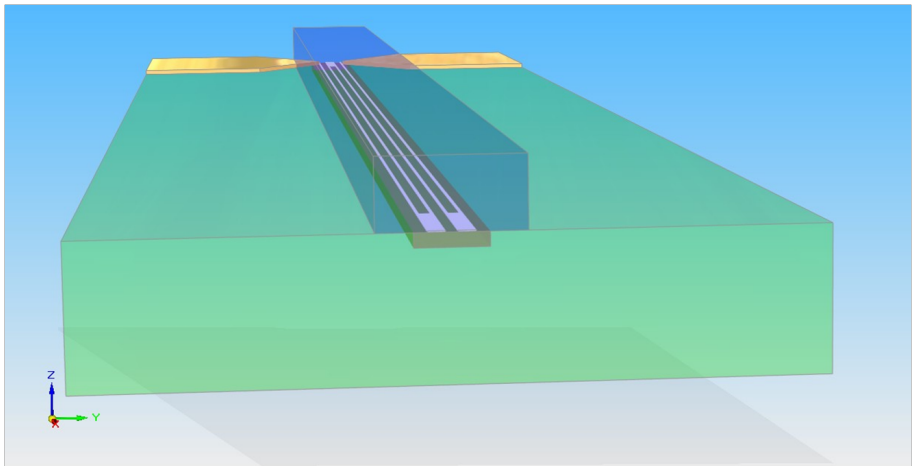

(a)

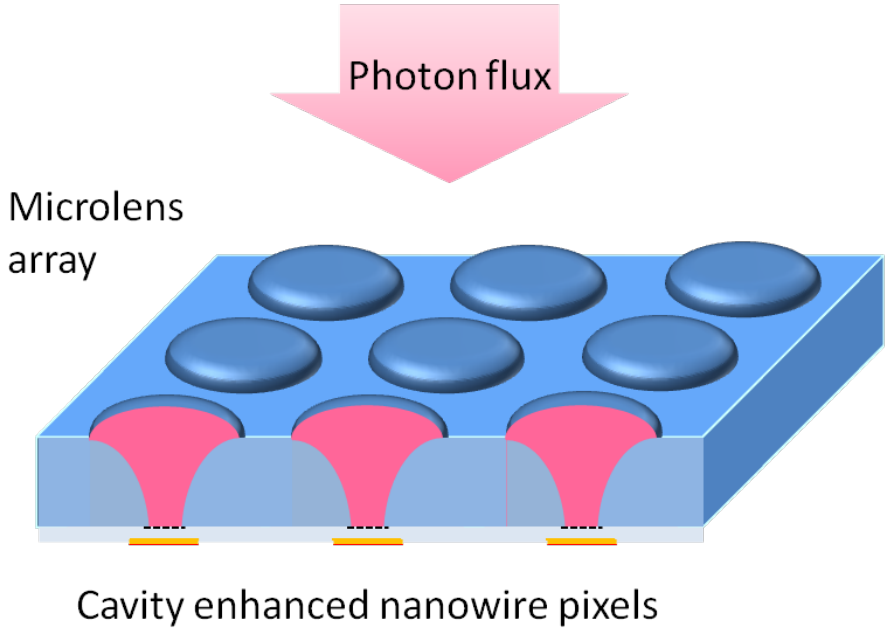

(b)

Figure 6.1: SNSPD device developments (a) SNSPD embedded in a waveguide (figure courtesy of Dr. M. G. Tanner), (b) nanowire pixels (figure courtesy of Dr. R. H. Hadfield).

the substrate of the SNSPD is etched out to accommodate the optical fibre. This allows precise alignment of SNSPD to the optical fibre without manual positioning. This technique can save packaging time and also result in highly efficient optical coupling. *Waveguide coupling*: Integrating a nanowire detector within a waveguide as shown in figure 6.1(a) has the potential to improve the coupling/absorption efficiency significantly [153]. The NbTiN device discussed in this thesis is an ideal choice to attempt both these techniques making use of the silicon substrate. The long-term goal for the optical quantum information science community is to demonstrate a proof-of-principle quantum processor on a single-chip. This would include waveguide single-photon source (e.g. periodically poled lithium niobate photon-pair source) to the waveguide and single-photon detectors.

Poor coupling efficiencies have currently limited the use of SNSPD in free space applications. Focussing the photons, to the small detector size (20 μm $\times$ 20 μm), in a real time free-space experiment is a challenging task. Fabricating an array of SNSPDs covering a larger area with individual focussing lenses (see figure 6.1(b)) or simple large area nanowire meanders would allow SNSPDs to be more widely utilised in free-space quantum key distribution, astronomy, eye-safe time-of-flight ranging, optical deep space communication and life sciences applications requiring fluorescence detection at the single-photon level.

6.2.2 Potential applications of the SNSPD detector system

Multiphoton experiments: Up to the present, SNSPDs have been used mainly for two-photon coincidence experiments due to their poor system detection efficiency. Demonstration of high efficiency detectors in this thesis work opens the pathway to attempting 4-photon coincidence experiments for the first time at telecom wavelengths in applications such as quantum metrology [154] and quantum simulations [95]. In figure 6.2, the probability of n-photon coincidence event is plotted against the detector efficiencies. For $\sim$1% SDE detectors, the two-photon detection experiments reported are already challenging due to their poor 2-photon coincidence detection probability (0.0001, point 'a'). The current detector system characterised in this thesis work has improved the probability by more than two orders of magnitude (0.04, point 'b'). With four $\sim$20% SDE detectors the probability of four-photon

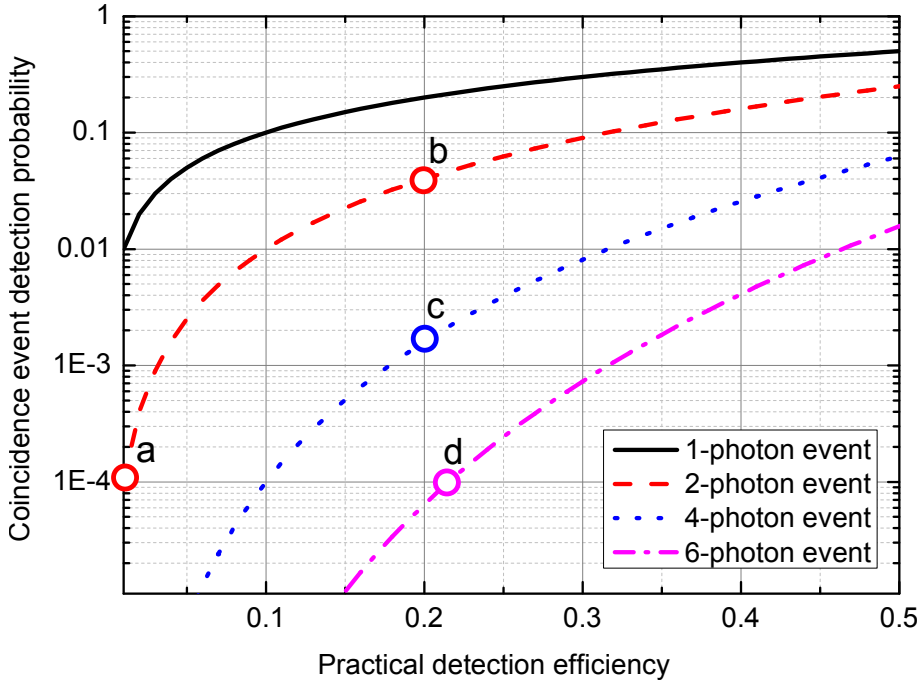

Figure 6.2: Coincidence event probability plotted against detector efficiency for different numbers of photon event. Point 'a' indicates the 2-photon coincidence event with 1% detection efficiency. Similarly, points 'b', 'c' and 'd' represent 2-photon, 4-photon and 6-photon coincidence events at ∼20% detection efficiency.

coincidence measurement is better by more than one order of magnitude (point 'c'). Even a six-photon coincidence measurement is well within reach with these type of detectors (point 'd'). At telecom wavelengths, SNSPDs can play a key role in developing 4 or 6 photon sources. This is a very important milestone to reach in the field of optical quantum information science.

A 50:50 fibre-beamsplitter at 1550 nm has been used to show a proof-of-principle two-photon quantum interference experiment at 1550 nm in this thesis work. Much advanced off-the-shelf available electro-optic components such as high speed polarisation controllers and 40 GBps phase or intensity modulators can be used to build complex high performance quantum information circuits at 1550 nm. These circuits can be characterised at very high frequencies using SNSPDs.

Looking beyond the realm of quantum information science, for atmospheric remote gas-sensing applications, sensitivity at mid infrared wavelengths is important (e.g. methane absorption peak at $\sim 3.2\ \mu$m). The sensitivity of SNSPDs beyond

telecom wavelengths has not been studied in detail yet [155]. There is scope to study the efficiency of these devices by substituting the current telecom fibre with low mid infrared absorption photonic bandgap fibre or chalcogenide fibre to couple the photons to the detectors. SNSPD design can be modified to suit mid-infrared wavelengths by using a narrower nanowire meander or parallel nanowire pattern [155].

6.2.3 Relaxing the cooling power requirements

New developments in Cryocoolers: The cooling power of the GM cryocooler used in this thesis work is more than needed for running two SNSPD channels (currently more applications need only 2 detectors). The portability of the current multichannel SNSPD system can be improved by mounting the devices into a smaller and lighter closed cycle cryocooler. In May 2009, Hybrid Stirling/J-T (Joule-Thomson) cooler reaching a base temperature of 4 K was demonstrated by Rutherford Appleton Laboratory, UK (for space science applications – Planck mission). This cryocooler has many advantages such as low power consumption (∼100 W), low vibration and less weight (20 kg). These cryocoolers can be employed for SNSPD operation in space and also can improve portability in the lab environments.

New superconducting materials: SNSPDs operating at higher temperatures can also relax the demanding needs of liquid He temperatures. The SNSPD devices reported to date are based on NbN or NbTiN although a wide variety of superconducting materials exist, including materials with considerably higher operating temperatures (cuprate high temperature superconductors and magnesium diboride, MgB_2 [T_c = 39 K]). Fabricating a superconducting nanowire meander using a novel material or even high-T_c superconductor is arguably just a question of technological development. Recently the first MgB_2 SNSPDs have been demonstrated, but performance (even at visible wavelengths) is poor [156]. The platform built in this thesis work can be readily employed to characterise any novel devices quickly and reliably, provided the substrate used is not opaque at 1550 nm. Further collaborations with thin film growth groups can accelerate development of SNSPD operating at higher temperatures using new materials.

6.3 Conclusion

During the course of this thesis work considerable advances have been made. A state-of-the-art laboratory for packaging and characterising SNSPDs has been set up at Heriot-Watt University (first of its kind in UK). We are now able to routinely characterise SNSPDs from a variety of sources, efficiently and with high reliability. A high performance multichannel SNSPD detector system has been constructed and successfully used in challenging quantum information science experiments (most notably with the University of Bristol, UK). As a result of this work, a duplicate detector system has been delivered to the UK National Physics Laboratory. There is considerable scope for further improvement in SNSPD devices, detector systems and their implementation in new photon-counting applications.

Appendix A: Calculation of Uncertainty for Visibility of Hong-Ou-Mandel Dip

General formula for error propagation for $q = q(x, ...z)$ is [157]:

$$\delta_q = \sqrt{\left(\frac{\partial q}{\partial x}\delta x\right)^2 + \cdots + \left(\frac{\partial q}{\partial z}\delta z\right)^2} \tag{1}$$

For the Hong-Ou-Mandel (HOM) dip, visibility parameter (V) in terms of maximum counts (V_{max}) and minimum counts (V_{min}) is

$$V = \frac{N_{max} - N_{min}}{N_{max}}$$

The Poissonian uncertainties (errors) of N_{max} and N_{min} (i.e. $\delta_{N_{max}}$ and $\delta_{N_{min}}$) are $\sqrt{N_{max}}$ and $\sqrt{N_{min}}$ respectively. From equation 1, the uncertainty in the visibility function can be derived as below

$$\begin{aligned}
\delta_V &= \sqrt{\left(\frac{\partial V}{\partial N_{max}}\right)^2 \delta^2_{N_{max}} + \left(\frac{\partial V}{\partial N_{min}}\right)^2 \delta^2_{N_{min}}} \\
&= \sqrt{\left(\frac{-N_{min}}{N^2_{max}}\right)^2 N_{max} + \left(\frac{-1}{N_{max}}\right)^2 N_{min}}
\end{aligned}$$

In practice, the Hong-Ou-Mandel dip measurement suffers from accidental coincidences as discussed in section 5.2.1. The accidental coincidence or background

counts (B) are subtracted from V_{max} and V_{min} to estimate the the corrected visibility parameter (V') of the Hong-Ou-Mandel dip as

$$\begin{aligned} V' &= \frac{(N_{max} - B) - (N_{min} - B)}{N_{max} - B} \\ &= \frac{N_{max}}{N_{max} - B} - \frac{N_{min}}{N_{max} - B} \end{aligned}$$

from equation 1, the uncertainty of the corrected visibility function can be derived as below

$$\begin{aligned} \delta'_V &= \sqrt{\left(\frac{\partial V}{\partial N_{max}}\right)^2 \delta^2_{N_{max}} + \left(\frac{\partial V}{\partial N_{min}}\right)^2 \delta^2_{N_{min}} + \left(\frac{\partial V}{\partial B}\right)^2 \delta^2_B} \\ &= \sqrt{\left(\frac{N_{min} - B}{(N_{max} - B)^2}\right)^2 N_{max} + \left(\frac{-1}{N_{max} - B}\right)^2 N_{min} + \left(\frac{N_{max} - N_{min}}{(N_{max} - B)^2}\right)^2 B} \end{aligned}$$

HOM dip was recorded using quantum waveguide directional couplers as discussed in section 5.2.1 using SNSPDs and Si-SPADs. The visibilities and uncertainties of the data recorded are tabulated below:

#	Detector type	N_{max}	N_{min}	B	V	δ_V
1	SNSPD_{raw}	859	66	–	92%	±1%
2	Si-SPAD_{raw}	10929	1103	–	89.9%	±0.3%
3	$\text{Si-SPAD}_{corrected}$	10929	1103	320	92.6%	±0.4%

As the calculation shows even in the case of low background counts for the Si-SPADs the uncertainty increases with background subtraction. The SNSPD allows the visibility to be measured faithfully without resorting to background subtraction. The error in the SNSPD measurement could be reduced by either (i) increasing the measurement time or (ii) increasing the detection efficiency via use of next generation SNSPDs. For example while maintaining the same V_{max}/V_{min} ratio, V_{min} can be estimated to have 769 counts for $V_{max} = 10000$ counts. For this case the predicted visibility is calculated as $92.3 \pm 0.3\%$.

Appendix B: Curve Fitting of Measured Hong-Ou-Mandel Dip Data

The curve fitting of the HOM data in section 5.2.1 merits further discussion. The shape of the Hong-Ou-Mandel (HOM) dip is based on the indistinguishability of the photons. The measured HOM data were fit to the following Lorentzian curve [96, 158]:

$$N_c = C(\mathscr{T}^2 + \mathscr{R}^2)\left[1 - X\frac{2\mathscr{R}\mathscr{T}}{\mathscr{R}^2 + \mathscr{T}^2}\frac{\Delta\omega^2}{\Delta\omega^2 + \delta\tau^2}\right]$$

Where N_c is the expected number of coincidences, C is an arbitrary constant, $\mathscr{R}$ and $\mathscr{T}$ are the reflectivity and transmissivity of the beam splitter, $\Delta\omega$ is the bandwidth, $c\delta\tau$ is the displacement and X is the correction factor for the imperfect destructive interference caused by the lack of overlap of the signal and idler fields admitted by the filters. $\mathscr{R}$ is estimated as 0.58 from the fit. Since $\mathscr{R}/\mathscr{T} \neq 1$, N_c does not drop down to 0 when $\delta\tau = 0$ ($X = 1$ [blue] curve in figures a and b). A correction factor of $X = 0.98$ has been used to fit the measured data (red curve). The waveguide directional coupler does not exhibit a reflection coefficient close to 0.5, as reported in references [11] and [159], in our experiments because of differences in the experimental environment. The reflection coefficient of the waveguide depends on parameters such as ambient temperature and wavelength of the incident photons. In our experiments, narrow spectral filters were used to enhance the indistinguishability of the photons. For example, the orientation of the filter relative to the incident optical beam can shift the exact central frequency of the filter affecting $\mathscr{R}$ and $\mathscr{T}$.

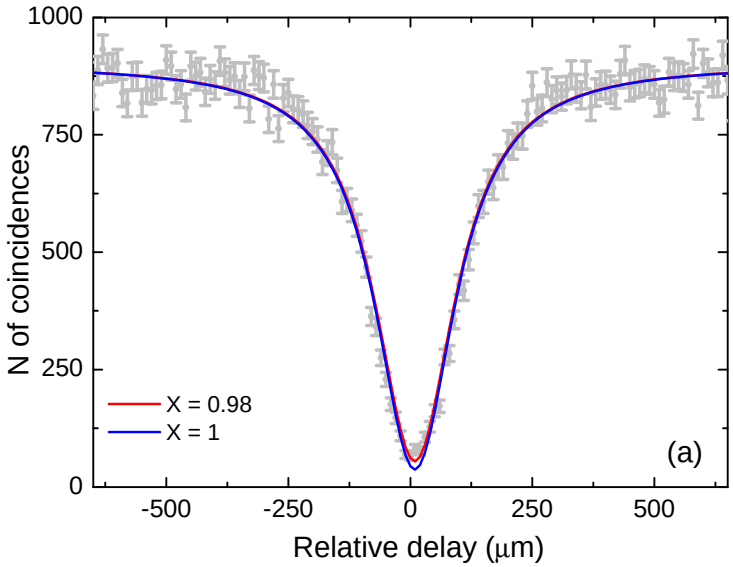

(a) HOM dip measured using SNSPDs. The data are fitted with a Lorentzian curve. The blue ($X = 1$) and red ($X = 0.98$) curves are the ideal and corrected HOM dips respectively. The extracted reflection coefficient of the directional coupler ($\mathscr{R}$) from the fit is 0.58.

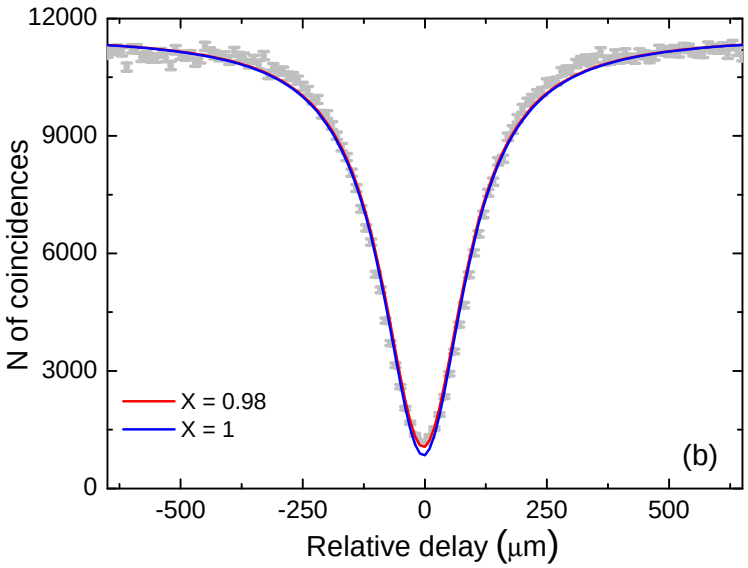

(b) HOM dip measured using SPADs. The data are fitted with a Lorentzian curve. The blue ($X = 1$) and red ($X = 0.98$) curves are the ideal and corrected HOM dips respectively. The extracted reflection coefficient of the directional coupler ($\mathscr{R}$) from the fit is 0.58.

References

[1] R. H. Hadfield, "Single-photon detectors for optical quantum information applications," *Nature Photon.* **3**, 696–705 (2009). 1, 9, 39, 66, 103, 107

[2] J. Mendenhall, L. Candell, P. Hopman, G. Zogbi, D. Boroson, D. Caplan, C. Digenis, D. Hearn, and R. Shoup, "Design of an optical photon counting array receiver system for deep-space communications," *Proc. IEEE* **95**, 2059 –2069 (2007). 1

[3] T. D. Ladd, F. Jelezko, R. Laflamme, Y. Nakamura, C. Monroe, and J. L. O'Brien, "Quantum computers," *Nature* **464**, 45–53 (2010). 1, 107

[4] N. Gisin, G. Ribordy, W. Tittel, and H. Zbinden, "Quantum cryptography," *Rev. Mod. Phys.* **74**, 145–195 (2002). 1, 4, 27, 28

[5] D. Elson, J. Requejo-Isidro, I. Munro, F. Reavell, J. Siegel, K. Suhling, P. Tadrous, R. Benninger, P. Lanigan, J. McGinty, C. Talbot, B. Treanor, S. Webb, A. Sandison, A. Wallace, D. Davis, J. Lever, M. Neil, D. Phillips, G. Stamp, and P. French, "Time-domain fluorescence lifetime imaging applied to biological tissue," *Photochem. Photobiol. Sci.* **3**, 795–801 (2004). 1, 3

[6] R. E. Warburton, A. McCarthy, A. M. Wallace, S. Hernandez-Marin, R. H. Hadfield, S. W. Nam, and G. S. Buller, "Subcentimeter depth resolution using a single-photon counting time-of-flight laser ranging system at 1550 nm wavelength," *Opt. Lett.* **32**, 2266–2268 (2007). 1, 7, 33, 34

[7] W. Becker, *The bh TCSPC Handbook*, 3rd ed. (Becker & Hickl GmbH, 2008). 2, 33, 72, 83

[8] *SPCM-AQRH Data sheet*, `http://www.perkinelmer.co.uk/PDFS/downloads/cat_sensorsandemittersphotondetection.pdf`, PerkinElmer Inc. (accessed date: January 19, 2011). 3, 37, 103

[9] T. Schmitt-Manderbach, H. Weier, M. Fürst, R. Ursin, F. Tiefenbacher, T. Scheidl, J. Perdigues, Z. Sodnik, C. Kurtsiefer, J. G. Rarity, A. Zeilinger, and H. Weinfurter, "Experimental demonstration of free-space decoy-state quantum key distribution over 144 km," *Phys. Rev. Lett.* **98**, 010504 (2007). 3

[10] K. Gordon, V. Fernandez, G. Buller, I. Rech, S. Cova, and P. Townsend, "Quantum key distribution system clocked at 2 GHz," *Opt. Express* **13**, 3015–3020 (2005). 3, 28

[11] A. Politi, M. J. Cryan, J. G. Rarity, S. Yu, and J. L. O'Brien, "Silica-on-silicon waveguide quantum circuits," *Science* **320**, 646–649 (2008). 3, 4, 6, 92, 94, 99, 104, 107, 116

[12] A. J. Shields, "Semiconductor quantum light sources," *Nature Photon.* **1**, 215–223 (2007). 3, 8, 31

[13] P. A. Hiskett, C. S. Parry, A. McCarthy, and G. S. Buller, "A photon-counting time-of-flight ranging technique developed for the avoidance of range ambiguity at gigahertz clock rates," *Opt. Express* **16**, 13685–13698 (2008). 3, 34

[14] *SMF28e+ Product information*, `http://www.corning.com/docs/opticalfiber/pi1463.pdf`, Corning Inc. (accessed date: January 25, 2011). 3, 51

[15] H. C. H. Mulvad, M. Galili, L. K. Oxenløwe, H. Hu, A. T. Clausen, J. B. Jensen, C. Peucheret, and P. Jeppesen, "Demonstration of 5.1 Tbit/s data capacity on a single-wavelength channel," *Opt. Express* **18**, 1438–1443 (2010). 3

[16] J. Zhang, R. Thew, C. Barreiro, and H. Zbinden, "Practical fast gate rate InGaAs/InP single-photon avalanche photodiodes," *Appl. Phys. Lett.* **95**, 091103 (2009). 4, 16

[17] G. N. Gol'tsman, O. Okunev, G. Chulkova, A. Lipatov, A. Semenov, K. Smirnov, B. Voronov, A. Dzardanov, C. Williams, and R. Sobolewski, "Picosecond superconducting single-photon optical detector," *Appl. Phys. Lett.* **79**, 705–707 (2001). 4, 7, 21, 22, 24, 26, 59, 73, 76, 77, 108

[18] K. M. Rosfjord, J. K. W. Yang, E. A. Dauler, A. J. Kerman, V. Anant, B. M. Voronov, G. N. Gol'tsman, and K. K. Berggren, "Nanowire single-photon detector with an integrated optical cavity and anti-reflection coating," *Opt. Express* **14**, 527–534 (2006). 4, 5, 8, 24, 37, 89, 107

[19] J. Zhang, W. Słysz, A. Verevkin, O. Okunev, G. Chulkova, A. Korneev, A. Lipatov, G. Gol'tsman, and R. Sobolewski, "Response time characterization of NbN superconducting single-photon detectors," *IEEE Trans. App. Supercond.* **13**, 180 – 183 (2003). 4

[20] H. Takesue, S. W. Nam, Q. Zhang, R. H. Hadfield, T. Honjo, K. Tamaki, and Y. Yamamoto, "Quantum key distribution over a 40-dB channel loss using superconducting single-photon detectors," *Nature Photon.* **1**, 343–348 (2007). 4, 7, 29, 107

[21] R. H. Hadfield, M. J. Stevens, S. S. Gruber, A. J. Miller, R. E. Schwall, R. P. Mirin, and S. W. Nam, "Single photon source characterization with a superconducting single photon detector," *Opt. Express* **13**, 10846–10853 (2005). 5, 32, 39, 66, 88, 107

[22] M. G. Tanner, C. M. Natarajan, V. K. Pottapenjara, J. A. O'Connor, R. J. Warburton, R. H. Hadfield, B. Baek, S. Nam, S. N. Dorenbos, E. B. U. na, T. Zijlstra, T. M. Klapwijk, and V. Zwiller, "Enhanced telecom wavelength single-photon detection with NbTiN superconducting nanowires on oxidized silicon," *Appl. Phys. Lett.* **96**, 221109 (2010). 5, 76, 85, 87, 89, 107

[23] J. L. O'Brien, A. Furusawa, and J. Vučković, "Photonic quantum technologies," *Nature Photon.* **3**, 687–695 (2009). 6, 78, 92, 93, 99

[24] P. Kok, W. J. Munro, K. Nemoto, T. C. Ralph, J. P. Dowling, and G. J. Milburn, "Linear optical quantum computing with photonic qubits," *Rev. Mod. Phys.* **79**, 135–174 (2007). 6, 29, 30, 31, 92

[25] C. M. Natarajan, A. Peruzzo, S. Miki, M. Sasaki, Z. Wang, B. Baek, S. Nam, R. H. Hadfield, and J. L. O'Brien, "Operating quantum waveguide circuits with superconducting single-photon detectors," *Appl. Phys. Lett.* **96**, 211101 (2010). 6, 106, 108

[26] A. Migdall and J. Dowling, "Eds. Special Issue: Single-Photon: Detectors, applications, and measurement methods," *J. Mod. Opt.* **51** (2004). 7

[27] C. Silberhorn, "Detecting quantum light," *Contemp. Phys.* **48**, 143 – 156 (2007). 8, 11

[28] S. Cova, M. Ghioni, A. Lotito, I. Rech, and F. Zappa, "Evolution and prospects for single-photon avalanche diodes and quenching circuits," *J. Mod. Opt.* **51**, 1267 – 1288 (2004). 8, 9, 10, 13, 14, 15

[29] D. Rosenberg, A. E. Lita, A. J. Miller, and S. W. Nam, "Noise-free high-efficiency photon-number-resolving detectors," *Phys. Rev. A* **71**, 061803 (2005). 8, 9, 20

[30] V. Anant, A. J. Kerman, E. A. Dauler, J. K. W. Yang, K. M. Rosfjord, and K. K. Berggren, "Optical properties of superconducting nanowire single-photon detectors," *Opt. Express* **16**, 10750–10761 (2008). 8, 68

[31] "Photomultiplier tubes: Basics and applications," 3rd ed., Hamamatsu City, Japan (2007). 9, 11, 12, 13

[32] A. Verevkin, J. Zhang, R. Sobolewski, A. Lipatov, O. Okunev, G. Chulkova, A. Korneev, K. Smirnov, G. N. Gol'tsman, and A. Semenov, "Detection efficiency of large-active-area NbN single-photon superconducting detectors in the ultraviolet to near-infrared range," *Appl. Phys. Lett.* **80**, 4687–4689 (2002). 9, 24, 25, 85

[33] S. Haykin, *Communication systems*, 4th ed. (J. Wiley and Sons, 2001). 10

[34] E. Dauler, B. Robinson, A. Kerman, J. Yang, E. Rosfjord, V. Anant, B. Voronov, G. Gol'tsman, and K. Berggren, "Multi-element superconducting nanowire single-photon detector," *IEEE Trans. App. Supercond.* **17**, 279 –284 (2007). 10, 25, 26

[35] A. Divochiy, F. Marsili, D. Bitauld, A. Gaggero, R. Leoni, F. Mattioli, A. Korneev, V. Seleznev, N. Kaurova, O. Minaeva, G. Gol'tsman, K. G. Lagoudakis, M. Benkhaoul, F. Lévy, and A. Fiore, "Superconducting nanowire photon-number-resolving detector at telecommunication wavelengths," *Nature Photon.* **2**, 302–306 (2008). 11, 26

[36] D. Achilles, C. Silberhorn, C. Śliwa, K. Banaszek, and I. A. Walmsley, "Fiber-assisted detection with photon number resolution," *Opt. Lett.* **28**, 2387–2389 (2003). 11

[37] A. Peacock, P. Verhoeve, N. Rando, A. van Dordrecht, B. G. Taylor, C. Erd, M. A. C. Perryman, R. Venn, J. Howlett, D. J. Goldie, J. Lumley, and M. Wallis, "Single optical photon detection with a superconducting tunnel junction," *Nature* **381**, 135–137 (1996). 11, 18

[38] B. Cabrera, R. M. Clarke, P. Colling, A. J. Miller, S. Nam, and R. W. Romani, "Detection of single infrared, optical, and ultraviolet photons using superconducting transition edge sensors," *Appl. Phys. Lett.* **73**, 735 –737 (1998). 11, 19

[39] *Understanding Photomultiplier*, `http://www.electrontubes.com/Photomultipliers/Understanding.pdf`, ET Enterprises Ltd (accessed date: January 10, 2011). 12

[40] A. Jiménez-Banzo, X. Ragàs, P. Kapusta, and S. Nonell, "Time-resolved methods in biophysics. 7. Photon counting vs. analog time-resolved singlet oxygen phosphorescence detection," *Photochem. Photobiol. Sci.* **7**, 1003–1010 (2008). 13, 34

[41] G. Ribordy, J.-D. Gautier, H. Zbinden, and N. Gisin, "Performance of InGaAs/InP avalanche photodiodes as gated-mode photon counters," *Appl. Opt.* **37**, 2272–2277 (1998). 14

[42] J. G. Rarity, T. E. Wall, K. D. Ridley, P. C. M. Owens, and P. R. Tapster, "Single-photon counting for the 1300–1600-nm range by use of Peltier-cooled and passively quenched InGaAs avalanche photodiodes," *Appl. Opt.* **39**, 6746–6753 (2000). 14

[43] R. Sidhu, H. Chen, N. Duan, G. Karve, J. Campbell, and A. Holmes, "GaAsSb resonant-cavity enhanced avalanche photodiode operating at 1.06 μm," *Electron. Lett.* **40**, 1296–1297 (2004). 14

[44] Z. L. Yuan, A. W. Sharpe, J. F. Dynes, A. R. Dixon, and A. J. Shields, "Multi-gigahertz operation of photon counting InGaAs avalanche photodiodes," *Appl. Phys. Lett.* **96**, 071101 (2010). 16, 37

[45] N. Namekata, S. Adachi, and S. Inoue, "1.5 GHz single-photon detection at telecommunication wavelengths using sinusoidally gated InGaAs/InP avalanche photodiode," *Opt. Express* **17**, 6275–6282 (2009). 16

[46] Z. L. Yuan, J. F. Dynes, A. W. Sharpe, and A. J. Shields, "Evolution of locally excited avalanches in semiconductors," *Appl. Phys. Lett.* **96**, 191107 –191107–3 (2010). 16

[47] B. E. Kardynał, Z. L. Yuan, and A. J. Shields, "An avalanche-photodiode-based photon-number-resolving detector," *Nature Photon.* **2**, 425–428 (2008). 16

[48] L. A. Jiang, E. A. Dauler, and J. T. Chang, "Photon-number-resolving detector with 10bits of resolution," *Phys. Rev. A* **75**, 062325 (2007). 16

[49] O. Thomas, Z. L. Yuan, J. F. Dynes, A. W. Sharpe, and A. J. Shields, "Efficient photon number detection with silicon avalanche photodiodes," *Appl. Phys. Lett.* **97**, 031102 (2010). 16

[50] M. A. Albota and F. C. Wong, "Efficient single-photon counting at 1.55 μm by means of frequency upconversion," *Opt. Lett.* **29**, 1449–1451 (2004). 16

[51] C. Langrock, E. Diamanti, R. V. Roussev, Y. Yamamoto, M. M. Fejer, and H. Takesue, "Highly efficient single-photon detection at communication wavelengths by use of upconversion in reverse-proton-exchanged periodically poled LiNbO3 waveguides," *Opt. Lett.* **30**, 1725–1727 (2005). 16

[52] R. T. Thew, S. Tanzilli, L. Krainer, S. C. Zeller, A. Rochas, I. Rech, S. Cova, H. Zbinden, and N. Gisin, "Low jitter up-conversion detectors for telecom wavelength GHz QKD," *New J. Phys.* **8**, 32 (2006). 16

[53] M. Tinkham, *Introduction to Superconductivity*, 2nd ed. (McGraw-Hill College, 1996). 17

[54] K. Fossheim and A. Subdø, *Superconductivity: Physics and Applications* (Wiley, 2004). 17

[55] J. R. Waldram, *Superconductivity of Metals and Cuprates* (IOP Publishing Ltd, 1996). 18

[56] S. Friedrich, "Superconducting tunnel junction photon detectors: Theory and applications," *J. Low Temp. Phys.* **151**, 277–286 (2008). 18, 19

[57] G. W. Fraser, J. S. Heslop-Harrison, T. Schwarzacher, P. Verhoeve, A. Peacock, and S. J. Smith, "Optical fluorescence of biological samples using STJs," *Nucl. Instrum. Meth. Phys. Res. A* **559**, 782–784 (2006). 18

[58] A. E. Lita, A. J. Miller, and S. W. Nam, "Counting near-infrared single-photons with 95% efficiency," *Opt. Express* **16**, 3032–3040 (2008). 19, 20

[59] A. J. Miller, S. W. Nam, J. M. Martinis, and A. V. Sergienko, "Demonstration of a low-noise near-infrared photon counter with multiphoton discrimination," *Appl. Phys. Lett.* **83**, 791 –793 (2003). 19, 20

[60] Z. Wang, A. Kawakami, Y. Uzawa, and B. Komiyama, "Superconducting properties and crystal structures of single-crystal niobium nitride thin films deposited at ambient substrate temperature," *J. Appl. Phys.* **79**, 7837–7842 (1996). 21, 45, 77

[61] J. Yang, A. Kerman, E. Dauler, V. Anant, K. Rosfjord, and K. Berggren, "Modeling the electrical and thermal response of superconducting nanowire single-photon detectors," *IEEE Trans. App. Supercond.* **17**, 581 –585 (2007). 21, 22, 24

[62] A. Annunziata, "Single-photon detection, kinetic inductance, and non-equilibrium dynamics in niobium and niobium nitride superconducting nanowires," Ph.D. thesis, Department of Applied Physics, Yale University, USA (2010). 21, 23

[63] R. H. Hadfield, A. J. Miller, S. W. Nam, R. L. Kautz, and R. E. Schwall, "Low-frequency phase locking in high-inductance superconducting nanowires," *Appl. Phys. Lett.* **87**, 203505 –203505–3 (2005). 23, 24, 59, 73

[64] A. J. Kerman, E. A. Dauler, W. E. Keicher, J. K. W. Yang, K. K. Berggren, G. Gol'tsman, and B. Voronov, "Kinetic-inductance-limited reset time of superconducting nanowire photon counters," *Appl. Phys. Lett.* **88**, 111116 (2006). 24, 59, 60, 73

[65] M. Ejrnaes, R. Cristiano, O. Quaranta, S. Pagano, A. Gaggero, F. Mattioli, R. Leoni, B. Voronov, and G. Gol'tsman, "A cascade switching superconducting single photon detector," *Appl. Phys. Lett.* **91**, 262509 (2007). 25

[66] M. Ejrnaes, A. Casaburi, R. Cristiano, O. Quaranta, S. Marchetti, and S. Pagano, "Maximum count rate of large area superconducting single photon detectors," *J. Mod. Opt.* **56**, 390 – 394 (2009). 25

[67] S. N. Dorenbos, E. M. Reiger, N. Akopian, U. Perinetti, V. Zwiller, T. Zijlstra, and T. M. Klapwijk, "Superconducting single photon detectors with minimized polarization dependence," *Appl. Phys. Lett.* **93**, 161102 (2008). 25, 68

[68] S. Miki, M. Fujiwara, M. Sasaki, B. Baek, A. J. Miller, R. H. Hadfield, S. W. Nam, and Z. Wang, "Large sensitive-area NbN nanowire superconducting single-photon detectors fabricated on single-crystal MgO substrates," *Appl. Phys. Lett.* **92**, 061116 (2008). 24, 37, 76, 77, 107

[69] A. J. Kerman, E. A. Dauler, J. K. W. Yang, K. M. Rosfjord, V. Anant, K. K. Berggren, G. N. Gol'tsman, and B. M. Voronov, "Constriction-limited detection efficiency of superconducting nanowire single-photon detectors," *Appl. Phys. Lett.* **90**, 101110 (2007). 25, 81, 82

[70] A. J. Kerman, J. K. W. Yang, R. J. Molnar, E. A. Dauler, and K. K. Berggren, "Electrothermal feedback in superconducting nanowire single-photon detectors," *Phys. Rev. B* **79**, 100509 (2009). 25, 64

[71] M. Ejrnaes, A. Casaburi, O. Quaranta, S. Marchetti, A. Gaggero, F. Mattioli, R. Leoni, S. Pagano, and R. Cristiano, "Characterization of parallel super-

conducting nanowire single photon detectors," *Supercond. Sci. Technol.* **22**, 055006 (2009). 25

[72] E. A. Dauler, A. J. Kerman, B. S. Robinson, J. K. W. Yang, B. Voronov, G. Goltsman, S. A. Hamilton, and K. K. Berggren, "Photon-number-resolution with sub-30-ps timing using multi-element superconducting nanowire single photon detectors," *J. Mod. Opt.* **56**, 364 – 373 (2009). 26

[73] F. Marsili, D. Bitauld, A. Fiore, A. Gaggero, R. Leoni, F. Mattioli, A. Divochiy, A. Korneev, V. Seleznev, N. Kaurova, O. Minaeva, and G. Goltsman, "Superconducting parallel nanowire detector with photon number resolving functionality," *J. Mod. Opt.* **56**, 334 – 344 (2009). 26

[74] D. Bitauld, F. Marsili, A. Gaggero, F. Mattioli, R. Leoni, S. J. Nejad, F. Levy, and A. Fiore, "Nanoscale optical detector with single-photon and multiphoton sensitivity," *Nano Lett.* **10**, 2977–2981 (2010). 26

[75] N. Gisin and R. Thew, "Quantum communication," *Nature Photon.* **1**, 165–171 (2007). 27

[76] C. H. Bennett and G. Brassard, "Quantum cryptography: Public key distribution and coin tossing," in "Systems and Signal Processing," , vol. 175 (Proceedings of IEEE International Conference on Computers, Bangalore, India, 1984), pp. 175–179. 27

[77] W. K. Wootters and W. H. Zurek, "A single quantum cannot be cloned," *Nature* **299**, 802–803 (1982). 27

[78] C. H. Bennett, F. Bessette, G. Brassard, L. Salvail, and J. Smolin, "Experimental quantum cryptography," *J. Cryptology* **5**, 3–28 (1992). 27

[79] P. Townsend, J. Rarity, and P. Tapster, "Single photon interference in 10 km long optical fibre interferometer," *Electron. Lett.* **29**, 634 –635 (1993). 27

[80] A. Muller, H. Zbinden, and N. Gisin, "Quantum cryptography over 23 km in installed under-lake telecom fibre," *Europhys. Lett.* **33**, 335 (1996). 27

[81] *Clavis2*, `http://www.idquantique.com/scientific-instrumentation/clavis2-qkd-platform.html`, ID Quantique SA (accessed date: November 20, 2010). 27

[82] *MagiQ QPN 8505*, `http://www.magiqtech.com/MagiQ/Products_files/8505_Data_Sheet.pdf`, MagiQ Technologies Inc. (accessed date: November 20, 2010). 27

[83] J. Bienfang, A. Gross, A. Mink, B. Hershman, A. Nakassis, X. Tang, R. Lu, D. Su, C. Clark, C. Williams, E. Hagley, and J. Wen, "Quantum key distribution with 1.25 Gbps clock synchronization," *Opt. Express* **12**, 2011–2016 (2004). 28

[84] W.-Y. Hwang, "Quantum key distribution with high loss: Toward global secure communication," *Phys. Rev. Lett.* **91**, 057901 (2003). 28

[85] X.-B. Wang, "Beating the photon-number-splitting attack in practical quantum cryptography," *Phys. Rev. Lett.* **94**, 230503 (2005). 28

[86] H.-K. Lo, X. Ma, and K. Chen, "Decoy state quantum key distribution," *Phys. Rev. Lett.* **94**, 230504 (2005). 28

[87] Y. Zhao, B. Qi, X. Ma, H.-K. Lo, and L. Qian, "Experimental quantum key distribution with decoy states," *Phys. Rev. Lett.* **96**, 070502 (2006). 28

[88] K. Inoue, E. Waks, and Y. Yamamoto, "Differential phase shift quantum key distribution," *Phys. Rev. Lett.* **89**, 037902 (2002). 28

[89] V. Scarani, A. Acín, G. Ribordy, and N. Gisin, "Quantum cryptography protocols robust against photon number splitting attacks for weak laser pulse implementations," *Phys. Rev. Lett.* **92**, 057901 (2004). 28

[90] D. Stucki, N. Brunner, N. Gisin, V. Scarani, and H. Zbinden, "Fast and simple one-way quantum key distribution," *Appl. Phys. Lett.* **87**, 194108 (2005). 28

[91] T. Schmitt-Manderbach, H. Weier, M. Fürst, R. Ursin, F. Tiefenbacher, T. Scheidl, J. Perdigues, Z. Sodnik, C. Kurtsiefer, J. G. Rarity, A. Zeilinger, and H. Weinfurter, "Experimental demonstration of free-space decoy-state

quantum key distribution over 144 km," *Phys. Rev. Lett.* **98**, 010504 (2007). 28

[92] R. Ursin, F. Tiefenbacher, T. Jennewein, and A. Zeilinger, "Applications of quantum communication protocols in real world scenarios toward space," *Elektrotechnik und Informationstechnik* **124**, 149–153 (2007). 28

[93] C. H. Bennett, G. Brassard, and N. D. Mermin, "Quantum cryptography without bell's theorem," *Phys. Rev. Lett.* **68**, 557–559 (1992). 29

[94] H. Takesue, K. ichi Harada, K. Tamaki, H. Fukuda, T. Tsuchizawa, T. Watanabe, K. Yamada, and S. ichi Itabashi, "Long-distance entanglement-based quantum key distribution experiment using practical detectors," *Opt. Express* **18**, 16777–16787 (2010). 29

[95] M. A. Nielsen and I. L. Chuang, *Quantum Computation and Quantum Information* (Cambridge Univ. Press, 2000). 29, 91, 92, 110

[96] C. K. Hong, Z. Y. Ou, and L. Mandel, "Measurement of subpicosecond time intervals between two photons by interference," *Phys. Rev. Lett.* **59**, 2044–2046 (1987). 30, 97, 116

[97] E. Knill, R. Laflamme, and G. J. Milburn, "A scheme for efficient quantum computation with linear optics," *Nature* **409**, 46–52 (2001). 31, 92, 98

[98] T. C. Ralph, N. K. Langford, T. B. Bell, and A. G. White, "Linear optical Controlled-NOT gate in the coincidence basis," *Phys. Rev. A* **65**, 062324 (2002). 31

[99] J. D. Franson, B. C. Jacobs, and T. B. Pittman, "Experimental demonstration of quantum logic operations using linear optical elements," *Fortschritte der Physik* **51**, 369–378 (2003). 31

[100] J. L. O'Brien, G. J. Pryde, A. G. White, T. C. Ralph, and D. Branning, "Demonstration of an all-optical quantum controlled-not gate," *Nature* **426**, 264–267 (2003). 31

[101] M. Varnava, D. E. Browne, and T. Rudolph, "How good must single photon sources and detectors be for efficient linear optical quantum computation?" *Phys. Rev. Lett.* **100**, 060502 (2008). 31, 108

[102] A. Gruber, A. Dräbenstedt, C. Tietz, L. Fleury, J. Wrachtrup, and C. v. Borczyskowski, "Scanning confocal optical microscopy and magnetic resonance on single defect centers," *Science* **276**, 2012–2014 (1997). 31

[103] C. Liang, K. F. Lee, M. Medic, P. Kumar, R. H. Hadfield, and S. W. Nam, "Characterization of fiber-generated entangled photon pairs with superconducting single-photon detectors," *Opt. Express* **15**, 1322–1327 (2007). 32

[104] M. A. Jaspan, J. L. Habif, R. H. Hadfield, and S. W. Nam, "Heralding of telecommunication photon pairs with a superconducting single photon detector," *Appl. Phys. Lett.* **89**, 031112 (2006). 32

[105] R. Y. Tsien, "The green flurorescent protein," *Annu. Rev. Biochem.* **67**, 509–544 (1998). 33

[106] W. Becker, A. Bergmann, M. Hink, K. Knig, K. Benndorf, and C. Biskup, "Fluorescence lifetime imaging by time-correlated single-photon counting," *Microsc. Res. Tech.* **63**, 58–66 (2004). 33

[107] J. S. Massa, A. M. Wallace, G. S. Buller, S. J. Fancey, and A. C. Walker, "Laser depth measurement based on time-correlated single-photon counting," *Opt. Lett.* **22**, 543–545 (1997). 34

[108] M. A. Albota, R. M. Heinrichs, D. G. Kocher, D. G. Fouche, B. E. Player, M. E. O'Brien, B. F. Aull, J. J. Zayhowski, J. Mooney, B. C. Willard, and R. R. Carlson, "Three-dimensional imaging laser radar with a photon-counting avalanche photodiode array and microchip laser," *Appl. Opt.* **41**, 7671–7678 (2002). 34

[109] V. Galievsky, A. Stasheuski, V. Kiselyov, A. Shabusov, M. Belkov, and B. Dzhagarov, "Laser NIR lifetime spectrometer with nanosecond time resolution," *Instrum. Exp. Tech.* **53**, 568–574 (2010). 34

[110] B. Li, H. Lin, D. Chen, M. Wang, and S. Xie, "Detection system for singlet oxygen luminescence in photodynamic therapy," *Chin. Opt. Lett.* **8**, 86–88 (2010). 34

[111] J. Schlothauer, S. Hackbarth, and B. Röder, "A new benchmark for time-resolved detection of singlet oxygen luminescence revealing the evolution of lifetime in living cells with low dose illumination," *Laser Phys. Lett.* **6**, 216–221 (2009). 34

[112] G. Ehret, C. Kiemle, M. Wirth, A. Amediek, A. Fix, and S. Houweling, "Space-borne remote sensing of CO_2, CH_4, and N_2O by integrated path differential absorption lidar: a sensitivity analysis," *Appl. Phys. B: Laser Optic.* **90**, 593–608 (2008). 35

[113] J. Caron and Y. Durand, "Operating wavelengths optimization for a space-borne lidar measuring atmospheric CO_2," *Appl. Opt.* **48**, 5413–5422 (2009). 35

[114] J. Abshire, H. Riris, X. Sun, M. Krainak, R. Kawa, J.-P. Mao, P.-S. Jian, and J. Burris, "Lidar approach for measuring the CO_2 concentrations in the troposphere from space," in "Lasers and Electro-Optics, 2007. CLEO 2007. Conference on," (2007), pp. 1 –2. 35

[115] J. Zhang, N. Boiadjieva, G. Chulkova, H. Deslandes, G. Gol'tsman, A. Korneev, P. Kouminov, M. Leibowitz, W. Lo, R. Malinsky, O. Okunev, A. Pearlman, W. Słysz, K. Smirnov, C. Tsao, A. Verevkin, B. Voronov, K. Wilsher, and R. Sobolewski, "Noninvasive CMOS circuit testing with NbN superconducting single-photon detectors," *Electron. Lett.* **39**, 1086 – 1088 (2003). 35

[116] *id210 Data sheet*, `http://www.idquantique.com/images/stories/PDF/id210-single-photon-counter/id210-specs.pdf`, ID Quantique SA (accessed date: May 04, 2011). 37

[117] T. M. Flynn, *Cryogenic engineering*, 2nd ed. (CRC Press, New York, 2005). 40, 41, 42

[118] R. Radenbaugh, "Refrigeration for superconductors," *Proc. IEEE* **92**, 1719 – 1734 (2004). 40

[119] *4K Cryocoolers*, `http://www.shicryogenics.com/index.php?option=com_content&task=blogcategory&id=22&Itemid=169`, SHI Cryogenics Group (accessed date: November 25, 2010). 40, 41, 42, 43

[120] J. W. Ekin, *Experimental techniques for low-temperature measurements* (Oxford University Press, New York, 2006). 44, 45

[121] Martin M. Härtig, "Optical fibre alignment for superconducting nanowire single-photon detectors," M. Phys. (Year 5) Research project report, Department of Physics, Heriot-Watt University, UK (2007-2008). 52

[122] J. Schmitt, "Optical coherence tomography (OCT): a review," *IEEE J. Quantum Electron.* **5**, 1205 –1215 (1999). 53

[123] D. Huang, E. A. Swanson, C. P. Lin, J. S. Schuman, W. G. Stinson, W. Chang, M. R. Hee, T. Flotte, K. Gregory, C. A. Puliafito, and J. G. Fujimoto, "Optical coherence tomography," *Science* **254**, 1178–1181 (1991). 53

[124] K. Serrels, M. Renner, and D. Reid, "Optical coherence tomography for non-destructive investigation of silicon integrated-circuits," *Microelectron. Engg.* **87**, 1785 – 1791 (2010). 53

[125] K. S. Il'in, M. Lindgren, M. Currie, A. D. Semenov, G. N. Gol'tsman, R. Sobolewski, S. I. Cherednichenko, and E. M. Gershenzon, "Picosecond hot-electron energy relaxation in NbN superconducting photodetectors," *Appl. Phys. Lett.* **76**, 2752 –2754 (2000). 59

[126] *S144A Power Meter Optical Head Specification Sheet*, `http://www.thorlabs.de/Thorcat/14100/14120-S01.pdf`, Thorlabs Inc. (accessed date: February 22, 2011). 65

[127] *S120B Power Meter Optical Head Specification Sheet*, `http://www.thorlabs.de/Thorcat/13300/13336-S01.pdf`, Thorlabs Inc. (accessed date: February 22, 2011). 65

[128] V. Anant, "Engineering the optical properties of subwavelength devices and materials," Ph.D. thesis, Department of Electrical Engineering and Computer Science, Massachusetts Institute of Technology, USA (2007). 68, 85, 86

[129] *PicoHarp 300*, `http://www.picoquant.com/_lightsources.htm`, PicoQuant GmbH (accessed date: March 04, 2011). 72

[130] S. N. Dorenbos, E. M. Reiger, U. Perinetti, V. Zwiller, T. Zijlstra, and T. M. Klapwijk, "Low noise superconducting single photon detectors on silicon," *Appl. Phys. Lett.* **93**, 131101 (2008). 76, 77, 78, 89, 107

[131] S. Miki, M. Fujiwara, M. Sasaki, and Z. Wang, "NbN superconducting single-photon detectors prepared on single-crystal MgO substrates," *IEEE Trans. App. Supercond.* **17**, 285–288 (2007). 77, 78

[132] A. Gaggero, S. J. Nejad, F. Marsili, F. Mattioli, R. Leoni, D. Bitauld, D. Sahin, G. J. Hamhuis, R. Nötzel, R. Sanjines, and A. Fiore, "Nanowire superconducting single-photon detectors on GaAs for integrated quantum photonic applications," *Appl. Phys. Lett.* **97**, 151108 (2010). 78, 89, 108

[133] *The Essential Macleod*, `http://www.thinfilmcenter.com/essential.html`, Thin Film Center Inc. (2011). 85

[134] W. Słysz, M. Wegrzecki, J. Bar, P. Grabiec, M. Gorska, V. Zwiller, C. Latta, P. Bohi, I. Milostnaya, O. Minaeva, A. Antipov, O. Okunev, A. Korneev, K. Smirnov, B. Voronov, N. Kaurova, G. Gol'tsman, A. Pearlman, A. Cross, I. Komissarov, A. Verevkin, and R. Sobolewski, "Fiber-coupled single-photon detectors based on NbN superconducting nanostructures for practical quantum cryptography and photon-correlation studies," *Appl. Phys. Lett.* **88**, 261113 (2006). 88

[135] S. Miki, T. Yamashita, M. Fujiwara, M. Sasaki, and Z. Wang, "Multichannel SNSPD system with high detection efficiency at telecommunication wavelength," *Opt. Lett.* **35**, 2133–2135 (2010). 89

[136] B. Baek, J. A. Stern, and S. W. Nam, "Superconducting nanowire single-photon detector in an optical cavity for front-side illumination," *Appl. Phys. Lett.* **95**, 191110 (2009). 89, 108

[137] P. G. Kwiat, J. R. Mitchell, P. D. D. Schwindt, and A. G. White, "Grover's search algorithm: an optical approach," *J. Mod. Opt.* **47**, 257–266 (2000). 91

[138] L. M. K. Vandersypen, M. Steffen, G. Breyta, C. S. Yannoni, M. H. Sherwood, and I. L. Chuang, "Experimental realization of Shor's quantum factoring algorithm using nuclear magnetic resonance," *Nature* **414**, 883–887 (2001). 91

[139] M. Mohseni, P. Rebentrost, S. Lloyd, and A. Aspuru-Guzik, "Environment-assisted quantum walks in photosynthetic energy transfer," *J. Chem. Phys.* **129**, 174106 (2008). 91

[140] N. A. Gershenfeld and I. L. Chuang, "Bulk spin-resonance quantum computation," *Science* **275**, 350–356 (1997). 91

[141] R. Blatt and D. Wineland, "Entangled states of trapped atomic ions," *Nature* **453**, 1008–1015 (2008). 91

[142] I. Chiorescu, Y. Nakamura, C. J. P. M. Harmans, and J. E. Mooij, "Coherent quantum dynamics of a superconducting flux qubit," *Science* **299**, 1869–1871 (2003). 92

[143] J. A. Schreier, A. A. Houck, J. Koch, D. I. Schuster, B. R. Johnson, J. M. Chow, J. M. Gambetta, J. Majer, L. Frunzio, M. H. Devoret, S. M. Girvin, and R. J. Schoelkopf, "Suppressing charge noise decoherence in superconducting charge qubits," *Phys. Rev. B* **77**, 180502 (2008). 92

[144] B. Trauzettel, D. V. Bulaev, D. Loss, and G. Burkard, "Spin qubits in graphene quantum dots," *Nature Phys.* **3**, 192–196 (2007). 92

[145] D. Kielpinski, C. Monroe, and D. J. Wineland, "Architecture for a large-scale ion-trap quantum computer," *Nature* **417**, 709–711 (2002). 92

[146] A. Politi, J. Matthews, M. Thompson, and J. O'Brien, "Integrated quantum photonics," *IEEE J. Quantum Electron.* **15**, 1673 –1684 (2009). 92, 93

[147] J. C. F. Matthews, A. Politi, StefanovAndre, and J. L. O'Brien, "Manipulation of multiphoton entanglement in waveguide quantum circuits," *Nature Photon.* **3**, 346–350 (2009). 92, 94, 102, 104, 107

[148] A. Peruzzo, M. Lobino, J. C. F. Matthews, N. Matsuda, A. Politi, K. Poulios, X.-Q. Zhou, Y. Lahini, N. Ismail, K. Wörhoff, Y. Bromberg, Y. Silberberg, M. G. Thompson, and J. L. O'Brien, "Quantum walks of correlated photons," *Science* **329**, 1500–1503 (2010). 94

[149] R. W. Boyd, *Nonlinear Optics*, 3rd ed. (Academic Press, Elsevier, Inc., Oxford, UK, 2008). 94

[150] C. M. Natarajan, M. M. Härtig, R. E. Warburton, G. S. Buller, R. H. Hadfield, B. Baek, S. W. Nam, S. Miki, M. Fujiwara, M. Sasaki, and Z. Wang, "Superconducting nanowire single-photon detectors for quantum communication applications," in "Quantum Communication and Quantum Networking," , vol. 36 of *Lecture Notes of the Institute for Computer Sciences, Social Informatics and Telecommunications Engineering* (Springer Berlin Heidelberg, 2010), pp. 225–232. 106

[151] X. Hu, T. Zhong, J. E. White, E. A. Dauler, F. Najafi, C. H. Herder, F. N. C. Wong, and K. K. Berggren, "Fiber-coupled nanowire photon counter at 1550 nm with 24% system detection efficiency," *Opt. Lett.* **34**, 3607–3609 (2009). 107

[152] C. R. Fitzpatrick, C. M. Natarajan, R. E. Warburton, G. S. Buller, B. Baek, S. Nam, S. Miki, Z. Wang, M. Sasaki, A. G. Sinclair, and R. H. Hadfield, "A superconducting nanowire single-photon detector system for single-photon source characterization," (SPIE, 2010), p. 76810H. 107

[153] X. Hu, C. Holzwarth, D. Masciarelli, E. Dauler, and K. Berggren, "Efficiently coupling light to superconducting nanowire single-photon detectors," *IEEE Trans. App. Supercond.* **19**, 336 –340 (2009). 110

[154] V. Giovannetti, S. Lloyd, and L. Maccone, "Quantum-enhanced measurements: Beating the standard quantum limit," *Science* **306**, 1330–1336 (2004). 110

[155] Y. Korneeva, I. Florya, A. Semenov, A. Korneev, and G. Goltsman, "New generation of nanowire nbn superconducting single-photon detector for mid-infrared," *IEEE/CSC & ESAS European Superconductivity News Forum* **15** (2011). 112

[156] H. Shibata, M. Asahi, T. Maruyama, T. Akazaki, H. Takesue, T. Honjo, and Y. Tokura, "Optical response and fabrication of MgB_2 nanowire detectors," *IEEE Trans. App. Supercond.* **19**, 358 –360 (2009). 112

[157] J. R. Taylor, *An introduction to error analysis : The study of uncertainties in physical measurements*, 2nd ed. (University Science Books, 1997). 114

[158] F. W. Sun and C. W. Wong, "Indistinguishability of independent single photons," *Phys. Rev. A* **79**, 013824 (2009). 116

[159] A. Laing, A. Peruzzo, A. Politi, M. R. Verde, M. Halder, T. C. Ralph, M. G. Thompson, and J. L. O'Brien, "High-fidelity operation of quantum photonic circuits," *Appl. Phys. Lett.* **97**, 211109 (2010). 116